Alma Mater Studiorum · University of Bologna

School of Science
Department of Physics and Astronomy
Master Degree in Physics

Study of a detection system for the search of the X17 boson at the n_TOF facility

Supervisor:
Prof. Cristian Massimi

Submitted by:
Nicholas Pieretti

Academic Year 2023/2024

Abstract

In recent years, a statistically significant anomaly has been observed in the emission of electron-positron pairs with an invariant mass of approximately $17\,\mathrm{MeV/c^2}$ at the HUN-REN ATOMKI laboratories. This so-called X17 anomaly consisted of an excess of events in the angular distribution of lepton pairs produced in the nuclear reactions $^{7}\mathrm{Li}(\mathrm{p},\mathrm{e^+e^-})^{8}\mathrm{Be}$, $^{3}\mathrm{H}(\mathrm{p},\mathrm{e^+e^-})^{4}\mathrm{He}$ and $^{11}\mathrm{B}(\mathrm{p},\mathrm{e^+e^-})^{12}\mathrm{C}$. Among several hypotheses, this anomaly may indicate the existence of a light neutral boson beyond the Standard Model. However, further independent experimental validation is needed to either confirm or refute these observations.

For this purpose, the conjugate neutron-induced reaction $^{3}\mathrm{He}(\mathrm{n},\mathrm{e^+e^-})^{4}\mathrm{He}$ has been proposed to be studied at the n_TOF facility. The measurement of angular distribution of the electron-positron pair produced in this reaction could confirm the existence of the X17 boson and, if detected, determine its quantum numbers. The detection system for this experiment is designed to provide large acceptance, particle identification and tracking. It consists of a layer of μ-RWELL gaseous detectors and a surrounding array of scintillator bars.

This thesis presents the characterization of the scintillator array, performed through data analysis of a test conducted at n_TOF. The role of the array in the experiment is to trigger the acquisition and to measure the incident neutron energy. Noise and saturation effects, which are crucial aspects in a neutron-dominated background, were evaluated for both the scintillator and the readout system. A hit-map reconstruction algorithm was implemented to improve the overall tracking resolution. While the scintillator array and SiPM readout were found suitable for the upcoming experiment, the data acquisition (DAQ) system showed several limitations, prompting the selection of an alternative system for the final setup.

Contents

Introduction

In the past few decades, many experiments have proved that the Standard Model (SM) of particle physics is a highly successful theory in describing fundamental particles and their interactions. However, some shortcomings led the SM to be regarded as a low-energy limit of a more comprehensive theory. In fact, some important questions are left unanswered, such as the nature of dark matter, the origin of the matter-antimatter asymmetry in the Universe, and the strong CP problem. These limitations have motivated extensive theoretical and experimental efforts to search for new physics phenomena.
A very active and developed research field in this context is the search for new particles, whose observation would constitute a clear, unambiguous signal of physics beyond the Standard Model. Surprisingly, a signal of this type could come from the realm of low-energy nuclear physics reactions.
During the transition of a nucleus from an excited state to its ground state, there are different competitive emission processes, among which the γ decay is usually dominant. Another process, known as internal pair creation (IPC), involves the emission of an electron-positron pair. The angular distribution of the correlation between the emitted leptons in IPC has been studied since the 1950s. Experimentally, it has been used to study the multipolarity of nuclear transitions by exploiting the different kinematics of magnetic and electric transitions at large angles.
However, in recent years, a statistically significant excess of emitted lepton pairs has been detected at large correlation angles at the HUN-REN ATOMKI laboratories at Debrecen, Hungary. This anomaly was observed after the de-excitation of the final nuclear states following the $^{7}\mathrm{Li}(\mathrm{p},\mathrm{e}^{+}\mathrm{e}^{-})^{8}\mathrm{Be}$, $^{3}\mathrm{H}(\mathrm{p},\mathrm{e}^{+}\mathrm{e}^{-})^{4}\mathrm{He}$ and $^{11}\mathrm{B}(\mathrm{p},\mathrm{e}^{+}\mathrm{e}^{-})^{12}\mathrm{C}$ reactions.
So far, no nuclear physics model has successfully explained this anomaly. A fascinating interpretation beyond the SM of these results points to the existence of a light boson decaying into the observed lepton pairs. This particle is referred to as X17, due to the value of the observed excess in the $e^{\pm}$ invariant mass of approximately $17\,\mathrm{MeV/c^2}$.
Despite the consistency of the observations at ATOMKI and the intriguing beyond SM prospect, additional experimental data are required to fully understand the nature of this anomaly. For this reason, many experiments worldwide are either investigating or planning to investigate the X17 anomaly through different channels. While some of these experiments have already constrained the coupling of this hypothetical particle

with ordinary matter, others are still in the R&D phase, but are expected to contribute significantly to the understanding of this phenomenon in the near future.
An interesting approach is the study of the neutron-induced reaction ^{3}He$(n, e^+e^-)^4$He reaction, considered complementary to the ^{3}H$(p, e^+e^-)^4$He one. This reaction has been proposed to be studied at the n_TOF facility at CERN, which provides a pulsed neutron beam characterized by high instantaneous neutron flux, wide energy range and high energy resolution.
The detection system has been designed to overcome the experimental limitations of the ATOMKI measurements and, at the same time, to minimize the effect of the challenging neutron-dominated background conditions. The setup that was proposed consists of four μ-RWELL gaseous detectors and a configuration of crossed scintillator bars surrounding the ^{3}He target.
In this thesis work, the performance of the crossed scintillator bars array has been evaluated. In particular, the analysis on data from a test conducted at n_TOF in 2023 has been performed, to assess the suitability of the detection system to the detection of $e^{\pm}$ pairs in the energy range of interest. The analysis included the estimation of background, saturation effects such as the dead time of the system, hit spatial reconstruction and response to different neutron energies.
Chapter 1 illustrates the theoretical framework behind the expected observations in the aforementioned nuclear reactions and some hypotheses on the observed X17 anomaly, together with a description of the ATOMKI experimental apparatus for its detection.
Chapter 2 provides an overview of the n_TOF facility, its purposes and the unique features of its neutron beam for the study of the reaction of interest.
In Chapter 3 the theoretical motivations and experimental solutions for the search of the X17 anomaly at n_TOF are reported. The apparatus used for the test studied in this thesis is also described.
Finally, Chapter 4 contains a review of the main results obtained from the data analysis carried out on the scintillator bar array.

Chapter 1

The X17 anomaly

In recent years, a research group at the HUN-REN Institute for Nuclear Research (ATOMKI) has observed a resonant structure at approximately 17 MeV/c^2 in the invariant mass distribution of positron-electron pairs, produced after excitation of target nuclei by means of a proton beam. The anomaly was observed with a significant deviation (greater than 6.6σ) from the theoretical expectations in the following nuclear reactions [1–3]:

$$^{7}\mathrm{Li}(\mathrm{p}, \mathrm{e}^{+}\mathrm{e}^{-})^{8}\mathrm{Be} \tag{1.1}$$

$$^{3}\mathrm{H}(\mathrm{p}, \mathrm{e}^{+}\mathrm{e}^{-})^{4}\mathrm{He} \tag{1.2}$$

$$^{11}\mathrm{B}(\mathrm{p}, \mathrm{e}^{+}\mathrm{e}^{-})^{12}\mathrm{C} \tag{1.3}$$

So far, this anomaly remains unexplained, and could indicate the existence of a light boson referred to as X17, with mass of approximately 17 MeV/c^2. The observations made by the ATOMKI group have yet to be confirmed or refuted by independent experiments.

1.1 Electromagnetic transitions in nuclei

For all three reactions 1.1, 1.2, 1.3, the excited intermediate state (Be*, He* or C*) can decay to the fundamental state either by high-energy gamma radiation emission (about 17 MeV) or by a positron-electron pair by Internal Pair Conversion (IPC).
The following section introduces the common framework of electromagnetic transitions, which constitute the main contribution of expected signals in the nuclear reactions studied at ATOMKI.

1.1.1 γ decay

When a nucleus is in an excited state, due to previous α or β decays or nuclear reactions, γ decay is the dominant process during the transition to the ground state. It consists of

an emission of one or several photons in the energy range 0.1 MeV to 10 MeV, typical of the energy separation between nuclear states. Consider a nucleus of mass M at rest, transitioning from an initial excited state E_i to a final state E_f. To conserve linear momentum, the final nucleus will recoil with momentum p_R and corresponding nonrelativistic recoil kinetic energy T_R, given by $T_R = \frac{p_R^2}{2M}$. Conservation of total energy and momentum gives:

$$\Delta E = E_i - E_f = E_\gamma + T_R$$

$$\mathbf{p_R} = -\mathbf{p}_\gamma$$

where E_γ and $\mathbf{p}_\gamma$ are the energy and the momentum of the emitted γ-ray photon, respectively.
Using the relativistic relation $E_\gamma = cp_\gamma$, it follows that:

$$\Delta E = E_\gamma + \frac{E_\gamma^2}{2Mc^2}$$

For $\Delta E \ll Mc^2$ (which holds true since ΔE is of the order of MeV), the γ-ray energy E_γ can be approximated as:

$$E_\gamma \cong \Delta E - \frac{(\Delta E)^2}{2Mc^2}$$

The recoil correction is typically on the order of 10^{-5} and is generally negligible compared to experimental uncertainties. Consequently, the approximation $\Delta E \approx E_\gamma$ is valid, implying that the measured photon energy serves as a first-order estimate of the energy difference between the nuclear states under investigation [4].
Even though the quantum description of electromagnetic radiation from nuclear transitions is more appropriate, some analogies from the classical treatment can aid in understanding quantum calculations. Static charge and current distributions generate static electric and magnetic fields, which can be described using the multipole moments of the charge distribution, such as the dipole and quadrupole moments. These moments produce characteristic fields that can be studied individually. The electromagnetic field produced by time-dependent charges and currents can also be obtained, at distances much greater than the source, through a multipole series expansion, characterized by the angular distribution of the emitted radiation.
For example, given a system with equal and opposite charges $+q$ and $-q$ separated by a fixed distance z, the electric dipole moment is defined as $d = qz$. A static magnetic dipole can be instead represented as a circular current loop of current i enclosing an area A, with the magnetic dipole moment given by $\mu = iA$.
When these dipole moments vary over time, they produce electromagnetic radiation fields. For instance, oscillating charges along the z axis generate an electric dipole radiation field described by $d(t) = qz\cos(\omega t)$, while varying currents produce a magnetic dipole

radiation field $\mu(t) = iA\cos(\omega t)$. In quantum mechanics, the different terms in the multipole expansion are associated with distinct values of angular momentum carried by the photon, characterized by the quantum number L. The index L in the context of multipole radiation indicates the multipole order, where $L = 1$ corresponds to dipole radiation, $L = 2$ to quadrupole, and so on. Using E for electric and M for magnetic, three properties of multipole radiation are worth mentioning:

1. The angular distribution of 2^L-pole radiation, relative to a chosen direction, is governed by the Legendre polynomial $P_{2L}(\cos\theta)$. For example, in the dipole case $P_2 = \frac{1}{2}(3\cos^2\theta - 1)$ is used.

2. The parity of the radiation field is:

$$\pi(ML) = (-1)^{L+1}$$

$$\pi(EL) = (-1)^{L}$$

   Electric and magnetic multipoles of the same order always have opposite parity.

3. The radiated power is:

$$P(uL) = \frac{2(L+1)c}{\epsilon_0 L\,[(2L+1)!!]^2}\left(\frac{\omega}{c}\right)^{2L+2}[m(uL)]^2 \tag{1.4}$$

   where $u = E$ or M represents electric or magnetic radiation, $m(uL)$ is the amplitude of the time-varying u multipole moment, and $(2L+1)!!$ denotes the double factorial $(2L+1)\cdot(2L-1)\cdot\ldots\cdot 3\cdot 1$.

The transition to the quantum mechanics description implies that the multipole moments $m(uL)$ become multipole operators, which change the nuclear state from ψ_i to ψ_f while simultaneously creating a photon of the proper energy, parity, and multipole order. The γ decay probability is therefore given by the matrix element of the multipole operator

$$m_{fi}(uL) = \int_V \psi_f^* m(uL)\psi_i\,dv \tag{1.5}$$

By dividing Eq. 1.4 by the emitted photon energy $\hbar\omega$, the probability per unit time for photon emission, commonly referred to as the decay constant $\lambda(uL)$, is obtained.
The decay constant for various electric multipole orders can be estimated by computing the matrix elements from Eq. 1.5, using the nuclear shell model to describe the transition.

These computations, together with other assumptions and approximations detailed in [4], are known as Weisskopf estimates. They provide relative comparisons for nuclear transition rates, rather than precise theoretical predictions.
The resulting estimates for the lower electric multipole orders, specifically for ^{8}Be ($A = 8$), are as follows:

$$\begin{aligned} \lambda(E1) &\simeq 4.0 \times 10^{14} E^3, \\ \lambda(E2) &\simeq 1.2 \times 10^{9} E^5, \\ \lambda(E3) &\simeq 2.2 \times 10^{3} E^7, \\ \lambda(E4) &\simeq 2.8 \times 10^{-3} E^9. \end{aligned} \tag{1.6}$$

where λ is in s^{-1} and E, the transition energy, is in MeV. The transition rates for lower magnetic multipole orders are:

$$\begin{aligned} \lambda(M1) &\simeq 5.6 \times 10^{13} E^3, \\ \lambda(M2) &\simeq 1.4 \times 10^{8} E^5, \\ \lambda(M3) &\simeq 2.6 \times 10^{2} E^7, \\ \lambda(M4) &\simeq 2.9 \times 10^{-4} E^9. \end{aligned} \tag{1.7}$$

Although these estimates are specifically calculated for ^{8}Be, the results are found to be very similar for the final states of $^3\mathrm{H}(\mathrm{p}, \mathrm{e}^+\mathrm{e}^-)^4\mathrm{He}$ and $^{11}\mathrm{B}(\mathrm{p}, \mathrm{e}^+\mathrm{e}^-)^{12}\mathrm{C}$.
Two key conclusions from the Weisskopf estimates are as follows:

1. Lower multipolarities dominate, with each increase in multipole order reducing the transition probability by approximately 10^5.

2. For light nuclei, electric radiation is generally more probable than magnetic radiation of the same multipole order by about one order of magnitude.

Another important consideration is that γ decays are governed by selection rules, which depend on the angular momentum and parity of the transition. For instance, nuclear $E0$ transitions do not result in the emission of a single photon because a photon must carry at least one unit of angular momentum. As a result, $E0$ transitions are instead observed through other mechanisms: either as emission of multiple photons, as ejection of a bound electron from its atomic shell, or by the creation of a positron-electron pair. The latter two processes, Internal Conversion and Internal Pair Creation, are explained in detail in the following subsections.

1.1.2 Internal Conversion

Internal conversion is an electromagnetic process that competes with γ emission. In this process, the electromagnetic fields of the nucleus do not result in photon emission; instead, these fields interact with atomic electrons, causing one of the electrons to be ejected from the atom. Unlike β decay, the electron involved in internal conversion is not newly created during the decay but is a pre-existing electron in an atomic orbit.
It is important to notice that internal conversion is not a two-step process where a photon is first emitted and then knocks an electron out of orbit, similar to the photoelectric effect, since such a scenario would have an extremely low probability of occurring.
The transition energy E involved in this process is converted into the kinetic energy T_e of the emitted electron, minus the binding energy B that is required to release the electron from its atomic shell:

$$T_e = E - B$$

The electron binding energy B in a specific shell sets the threshold for internal conversion to occur). Thus, conversion electrons are identified by the electronic shell they originate from, such as K, L, M, etc., corresponding to principal atomic quantum numbers $n = 1, 2, 3$, and so on.
The intensity of the conversion electron process varies depending on the multipolarity of the radiation field. In some cases, internal conversion is much more probable than γ emission, while in others, it may be negligible. It is generally necessary to account for internal conversion when calculating the probability of γ emission.
To account for this contribution, the internal conversion coefficient (ICC) α is defined as:

$$\alpha = \frac{\lambda_e}{\lambda_\gamma}$$

where λ_e and λ_γ are the internal conversion and γ emission decay probability constants, respectively. Partial conversion coefficients can be defined for individual atomic shells, such as K, L, M, etc., and further subdivided into subshells if needed.
Since the process is electromagnetic in nature, the matrix element that governs it is similar to that of Eq. 1.5, but with initial state including a bound electron, denoted as $\psi_i = \psi_{i,N}\psi_{i,e}$, where N represents the nuclear wave function and e represents the electron wave function. In the final state, $\psi_f = \psi_{f,N}\psi_{f,e}$, where $\psi_{f,e}$ is the free-particle wave function.
An important aspect is that, with a degree of approximation, all nuclear-specific information is contained within $\psi_{i,N}$ and $\psi_{f,N}$, and both γ emission and internal conversion are governed by the same electromagnetic multipole operator $m(uL)$. Consequently, the nuclear part of the matrix element in Eq. 1.5 remains identical for both processes. Given that both $\lambda_\gamma(uL)$ and $\lambda_e(uL)$ are proportional to $|m_{fi}(uL)|^2$, their ratio α is independent of the specific details of nuclear structure. This result relies on an approximation that

assumes the electron wavefunction does not significantly "penetrate" the nucleus. While the electron wavefunction does interact with the specific nuclear wavefunction to some extent, this interaction typically has a very slight and usually negligible effect on the conversion coefficient. An approximated, non-relativistic calculation gives the following results:

$$\begin{aligned} \alpha(EL) &\propto \frac{Z^3}{n^3}\frac{L}{L+1}\left(\frac{1}{E}\right)^{L+\frac{5}{2}} \\ \alpha(ML) &\propto \frac{Z^3}{n^3}\left(\frac{1}{E}\right)^{L+\frac{3}{2}} \end{aligned} \tag{1.8}$$

where n is the principal quantum number of the bound electron wave function. It can be noted that internal conversion is an important effect for nuclei of high atomic number Z in low-energy transitions of high multipole order L.

1.1.3 Internal Pair Creation

Where the transition energy from an excited state to a lower-energy one is high enough ($> 1.022\,\mathrm{MeV}$), it is possible for an emitted photon to convert into a positron–electron pair in the Coulomb field of the emitting nucleus. This process is known as Internal Pair Creation, Internal Pair Conversion (IPC) or Internal Pair Formation.
In this scenario the transition energy can be transmitted to electrons in the "negative-energy states" near the nucleus. From Dirac's theory it is well known that the states of negative kinetic energy are occupied by electrons. The lifting of one of these negative-energy electrons into a positive-energy state appears as the creation of an electron-positron pair.
The electron wave functions which are used to compute IPC probability (in a very similar manner to the one described in Section 1.1.2) are the continuum solutions of the Dirac equation for a nuclear potential V_N:

$$(\boldsymbol{\alpha}\cdot\mathbf{p} + V_N + \beta m_e)\psi = i\frac{\partial\psi}{\partial t}\ ,$$

where $\boldsymbol{\alpha}$ and β are the Dirac matrices, m_e the mass of the electron and $\mathbf{p}$ its momentum. A complete orthogonal set of continuum solutions which can be used are either ordinary plane waves or Coulomb-distorted plane waves, which are the exact scattering wave functions for electrons and positrons and are derived by solving the Dirac equation in parabolic coordinates [5].
First calculations of the angular correlation in internal pair conversion were performed by Rose [6] for the multipolarity $L > 0$ of the nuclear transition. His calculations utilize second-order perturbation theory with ordinary plane waves as lepton wave functions, i.e. Born approximation is employed.

The representation of electrons and positrons by ordinary plane waves implies the neglect of any Coulomb distortion. For the decay of states close to threshold in heavy nuclei, however, one clearly should take into account that electrons and positrons are created in the Coulomb potential of the nucleus [7]. As a consequence, the lepton wave functions will be strongly deformed by this potential, which is characterized by the coupling constant $Z\alpha$ ($= 0$ if plane waves are used instead), where α is the fine structure constant. For high transition energy and low atomic number Z, the full calculations agree with the results obtained from the Born approximation. Thus, for the reactions of interest mentioned above, the Born approximation is sufficient.
For nuclear transitions of angular momentum $L > 0$, any penetration effect is neglected, as already done in Section 1.1.2, which would otherwise require assumptions about a specific nuclear model. These assumptions would drastically complicate the calculations and, furthermore, would contain uncertainties on the same scale as this "no penetration" approximation.
Similarly to the IC case, the Internal Pair Conversion Coefficient (IPCC) β is defined, for $L > 0$, as the ratio of the pair conversion probability to the γ emission probability:

$$\beta = \frac{\lambda_{e^+e^-}}{\lambda_\gamma}$$

As mentioned in Section 1.1.1, $E0$ transitions do not result in photon emission, since it is forbidden by conservation of angular momentum and parity. In this case, the IPCC is defined as:

$$\eta = \frac{\lambda_{e^+e^-}}{\lambda_e}$$

Calculations of the IPCC have been extensively investigated, and the results are tabulated in various references [8–10]. The IPCC exhibits the following general trends:

1. It increases with the transition multipole order L.
2. It increases with the transition energy.
3. It slightly decreases with the atomic number Z.

As a result, the IPC rate becomes most significant in scenarios where the IC rate is lowest, namely in the region of low atomic number Z and high transition energies.
The angular correlation of the emitted positron-electron pairs provides a method of distinguishing between the different types and multipole order of the transition under study [11].
As previously noted, the estimates by Rose [6], based on the Born approximation, are sufficiently accurate for the reactions of interest in this thesis, given the low atomic number Z and the high transition energy E of the involved excited states.

Additionally, while more precise calculations are available, they still fail to explain the observed anomaly at $\simeq 17\,\mathrm{MeV/c^2}$.
Considering $e^{\pm}$ pairs traveling in the solid angles $d\Omega_-$ and $d\Omega_+$, respectively, and the positron energy included in the range $[W_+, W_+ + dW_+]$, the ratio of the number of produced pairs per second to the number of emitted photons per second, is given by

$$d\gamma_L(W_+;\theta_+,\varphi_+;\theta_-,\varphi_-) = \frac{\alpha E}{32\pi^3} p_+ p_- W_+ W_- \sum_{s_- s_+} \left|\langle\psi_-|\phi + \boldsymbol{\alpha}\cdot\mathbf{A}|\psi_+\rangle\right|^2 d\Omega_+ d\Omega_- dW_+ \ ,$$

where $\hbar = m_e = c = 1$, $W_\pm$, $\mathbf{p}_\pm$, $\theta_\pm$, $\varphi_\pm$ and $\psi_\pm$ are the $e^\pm$ total energies, momenta, emission polar coordinates and Dirac spinor wave functions, respectively, and ϕ and $\mathbf{A}$ the scalar and vector potentials, representing the radiation field.
The distribution of the correlation angle Θ is obtained after the integration over the two solid angles, $W_\pm$ being fixed. Naming $\mathbf{q} = \mathbf{p}_+ + \mathbf{p}_-$, the result for the electric multipoles is:

$$\begin{aligned}\gamma_L^E(\Theta) = \frac{2\alpha}{\pi(L+1)}\frac{p_+p_-}{q}\frac{\left(\frac{q}{E}\right)^{2L-1}}{(E^2-q^2)^2}\Bigg\{&(2L+1)\left(W_+W_- + 1 - \frac{1}{3}p_+p_-\cos\Theta\right) + \\ &+ L\left(\frac{q^2}{E^2} - 2\right)(E_+E_- - 1 + p_+p_-\cos\Theta) + \\ &+ \frac{1}{3}(L-1)p_+p_-\left[\frac{3}{q^2}(p_- + p_+\cos\Theta)(p_+ + p_-\cos\Theta) - \cos\Theta\right]\Bigg\}\end{aligned} \tag{1.9}$$

and for the magnetic multipoles:

$$\begin{aligned}\gamma_L^B(\Theta) = \frac{2\alpha}{\pi}\frac{p_+p_-}{q}\frac{\left(\frac{q}{E}\right)^{2L+1}}{(E^2-q^2)^2}\Bigg\{&1 + W_+W_- - \\ &\frac{p_+p_-}{q^2}(p_- + p_+\cos\Theta)(p_+ + p_-\cos\Theta)\Bigg\}\end{aligned} \tag{1.10}$$

By integrating Eq. 1.9 and 1.10 over Θ and W_+, the IPCCs for electric or magnetic multipoles are obtained:

$$\beta_L^u = \int_1^{E-1}\int_0^{\pi} \gamma_L^u(\Theta, W_+)\sin\Theta d\Theta dW_+$$

Rose's calculations are applicable in situations where the γ radiation in electromagnetic transitions is emitted isotropically, such as following β decay. In these cases, the emission of $e^\pm$ pairs is also isotropic, meaning that the probability of emission does not depend on the spatial orientation of the triangle formed by the momenta $p_\pm$ of the emitted particles, though it will depend on the triangle's size and shape.

However, when excited nuclear states are produced by bombarding a target with a particle beam, the resulting radiations are generally not isotropic. The angular correlation of internally converted pairs under these conditions has been studied by Goldring [12] and Rose [13], particularly when the excited state is formed during a nuclear reaction involving a particle beam. The treatment in the case of heavy nuclei has been performed in [14]. For optimal experimental results, the detectors should be positioned in the plane perpendicular to the beam and made sensitive to the same energy range. This setup ensures little interference between magnetic and electric transitions, and the angular correlation for each specific transition can be determined by integrating the relevant expressions over the appropriate energy interval. However, the interference contribution must be still considered in a rigorous analysis of experimental results, also at right angles to the beam [15].
The IPCC, as illustrated in Figure 1.1, decreases as the correlation angle Θ increases for the lowest multipole orders of E and M transitions.

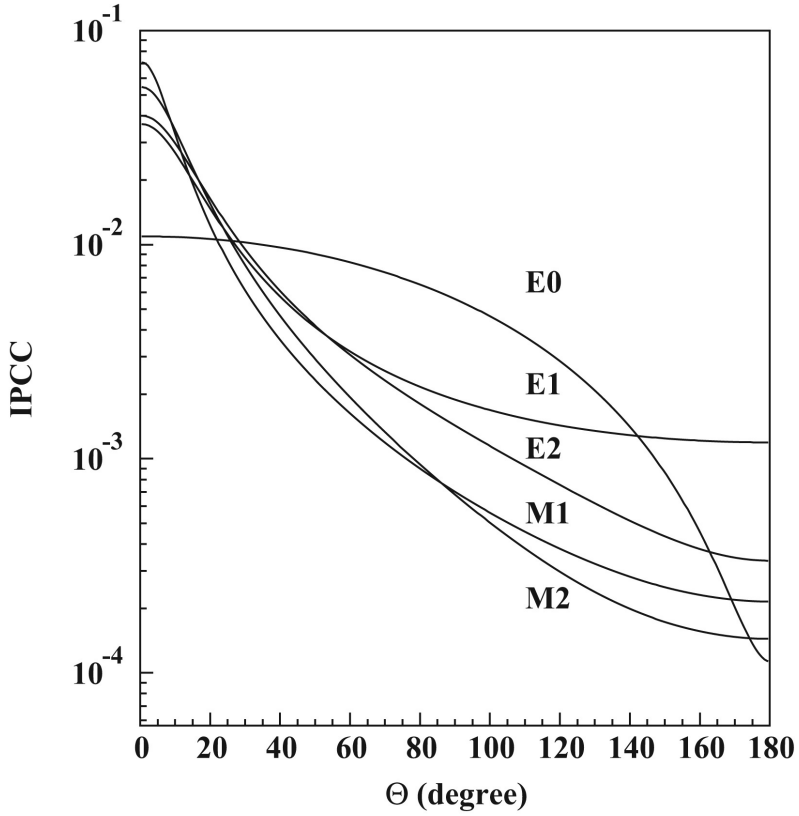

Figure 1.1: IPCC for different electromagnetic transitions as a function of the correlation angle Θ. Image produced in [16], using Rose's calculations [6] at the transition energy $E = 17\,\mathrm{MeV}$.

After the theoretical calculations of IPC were developed, experimental searches were performed and confirmed with great accuracy the expected angular correlation distribution of $e^{\pm}$ pairs from IPC, both shortly after the theoretical predictions [17–19] and in later years [20–22]. As a result, IPC angular distributions have become a well-established tool for studying the multi-polarity of nuclear transitions, exploiting the different kinematics of magnetic and electric transitions at large angles.
The recent measurements at ATOMKI, which detected the X17 anomaly, fall within this long-standing framework of IPC studies. The following sections will provide an experimental overview of these measurements and describe their possible theoretical interpretations.

1.2 The ATOMKI measurements

Because of their low mass numbers, ^{8}Be, ^{4}He, and ^{12}C exhibit relatively few excited states, with most of the first ones located more than 10 MeV above their ground states, particularly in the case of ^{8}Be and ^{4}He. Combined with the high Q-values of the reactions ^{7}Li(p, e^{+}e^{-})^{8}Be, ^{3}H(p, e^{+}e^{-})^{4}He and ^{11}B(p, e^{+}e^{-})^{12}C, this creates the ideal conditions for exploring new particles such as X17, as the accessible mass region is significantly larger compared to other nuclei typically used in IPC studies.
The ^{8}Be nuclear excitation spectrum is known with high precision [23]. The ^{8}Be nuclear states relevant for the X17 anomaly, denoted as ^{8}Be* and ^{8}Be*', and their properties are illustrated in Figure 1.2.

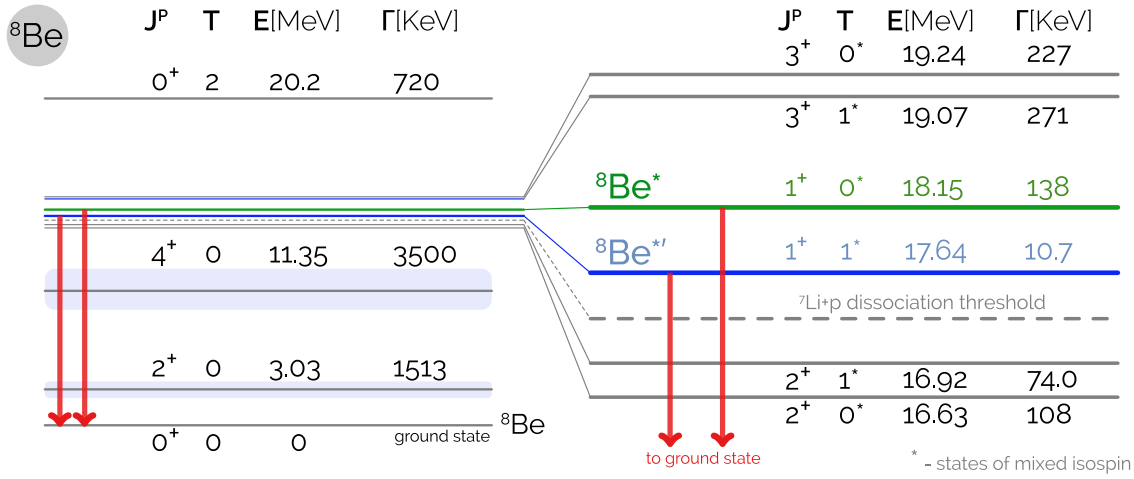

Figure 1.2: Energy level diagram of the relevant ^{8}Be states, together with their spin-parities J^{P} , isospins T , excitation energies E, and decay widths Γ. Asterisks on isospin assignments indicate states with significant isospin mixing [24].

As previously mentioned, the reaction $^7\mathrm{Li(p, e^+e^-)^8Be}$ (Eq. 1.1) was studied by Krasznahorkay et al. [1], sending protons with kinetic energy of 1.025 MeV and 0.441 MeV, to populate the ^{8}Be* and and ^{8}Be*', at 18.15 MeV and 17.64 MeV from the ^{8}Be ground state, respectively.
The resulting excited states decay promptly, dominantly back to $p + {}^7$Li, but also through γ emission and IPC. For example, the radiative decay to the ground state of ^{8}Be* has branching ratio $B(^8\mathrm{Be}^* \rightarrow {}^8\mathrm{Be}\,\gamma) \approx 1.4 \times 10^{-5}$, while the IPC has branching ratio $B(^8\mathrm{Be}^* \rightarrow {}^8\mathrm{Be}\,e^+e^-) \approx 3.9 \times 10^{-3} B(^8\mathrm{Be}^* \rightarrow {}^8\mathrm{Be}\gamma) \approx 5.5 \times 10^{-8}$ [25].
By measuring the correlation angle Θ and the invariant mass $m_{e^\pm}$ of the emitted $e^\pm$ pairs, the ATOMKI measurements showed an excess of counts at about $\Theta \approx 140°$ and $m_{e^\pm} \approx 17\,\mathrm{MeV/c^2}$.
As illustrated in Figure 1.3, the excess is maximal on the ^{8}Be* resonance and disappears as the proton beam energy is moved off resonance. No such effect is seen in ^{8}Be*' IPC decays.

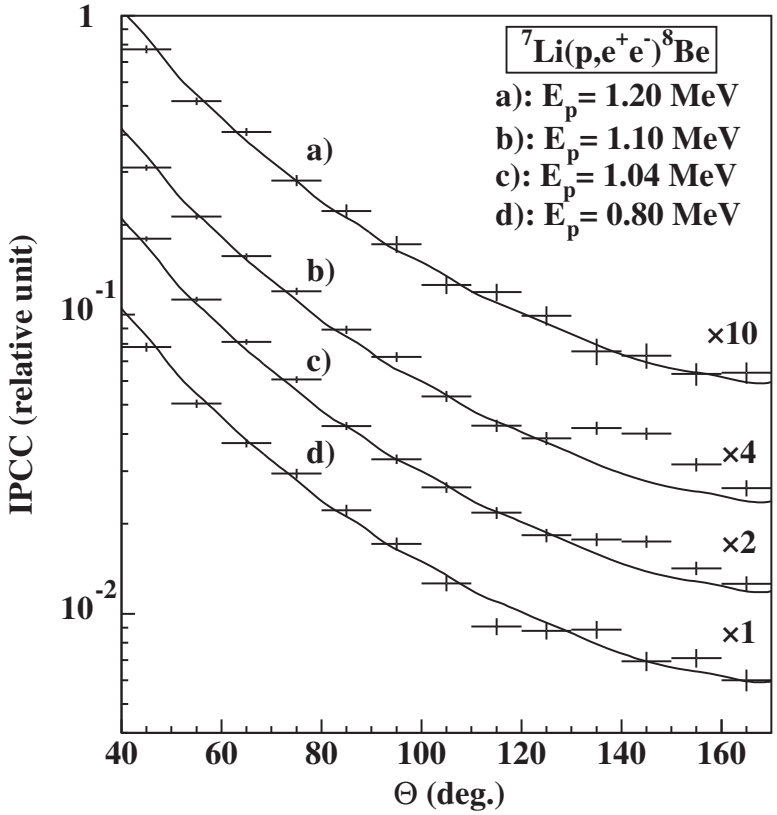

Figure 1.3: The ATOMKI excess observed at $\Theta \approx 140°$ in the reaction of Eq. 1.1. The solid lines represent the simulated IPC signals, while the data points with error bars correspond to experimental measurements for different proton beam kinetic energies E_p scanning through the resonance [1].

More in detail, in the experiment, proton beams from a 5 MV Van de Graaff accelerator, with a typical current of 1.0 µA, were impinged onto targets consisting of 15 µg cm^{-2} thick LiF_2 and 700 µg cm^{-2} thick LiO_2 layers evaporated onto 10 µm Al backings.
Given the very low energy of the emerging $e^{\pm}$ pairs (only a few MeV), accurate measurement of their angular distribution is challenging. In the original setup, depicted in Figure 1.4 (a), the $e^{\pm}$ pairs were detected using five $\Delta E - E$ detector telescopes, combined with position-sensitive detectors. The ΔE detectors were very thin plastic scintillators, measuring 38 mm × 45 mm × 1 mm, selected for their excellent γ-ray suppression capabilities, while the much thicker E detectors, measuring 78 mm × 60 mm × 70 mm, were used to separately determine the $e^{\pm}$ energies.
The $\Delta E - E$ detector telescopes were positioned perpendicularly to the beam direction at azimuthal angles of 0°, 60°, 120°, 180°, and 270°. These angles ensured homogeneous acceptance of the $e^{\pm}$ pairs as a function of the correlation angle Θ.
The hit positions were determined by multiwire proportional counters (MWPC) [26] placed in front of the ΔE and E detectors.
The target strip foil was oriented perpendicular to the beam direction, and the telescope detectors were arranged around the vacuum chamber, which was constructed from a 1 mm-thick carbon-fiber tube. The use of a thin support for the target and carbon-fiber beam-pipe limits multiple scattering of e^+e^- pairs, thus avoiding the deterioration of aperture angle resolution.
A more detailed description of the experimental setup is available in [16].
Subsequently, using an improved accelerator, detection system and data analysis, the ATOMKI group confirmed the original anomaly in the ^{8}Be* [27] and observed other similar anomalies in the reactions ^{3}H(p, e^+e^-)^{4}He (Eq. 1.2) and ^{11}B(p, e^+e^-)^{12}C (Eq. 1.3), with high statistical significance at the same invariant mass [2, 3]. The ^{8}Be* anomaly has been later confirmed also by using a similar experimental setup in a different facility [28].
A comparison between the original detection system and the updated one used at ATOMKI is illustrated in Figure 1.4, while in Figure 1.5 a more detailed scheme of the updated setup is shown.
The detection of $e^{\pm}$ pairs in the updated detection system is carried out by 6 telescopes mounted in a plane orthogonal to the beamline. Each telescope consists of a double-sided silicon detector (DSSD) with orthogonal strips 3 mm wide and 0.5 mm thick, coupled with a plastic scintillator with dimensions 82 mm × 86 mm × 80 mm. The silicon strips provide the impact point of crossing particles, while the scintillators are used to measure the $e^{\pm}$ energies. The detection system, however, does not provide 3D reconstruction of the $e^{\pm}$ tracks nor their identification. It is also noted that the angular acceptance of the apparatus is limited to particles emitted at $\approx 90°$ with respect to the beamline [29].

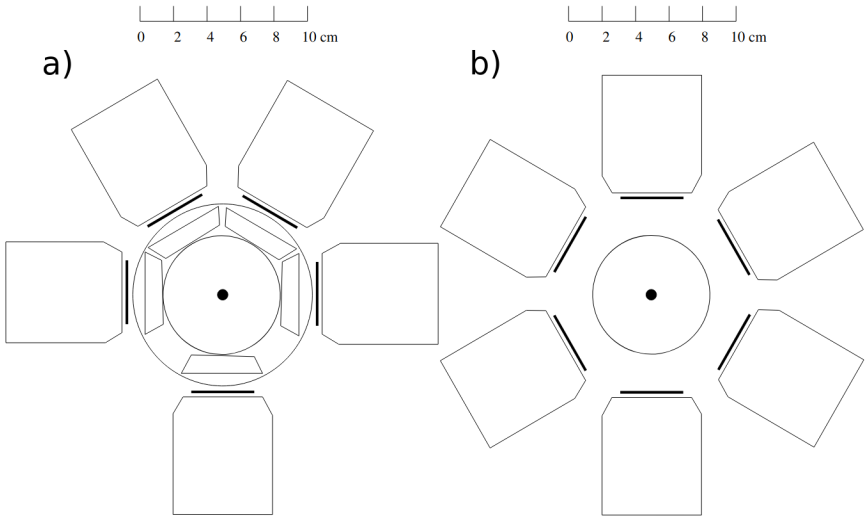

Figure 1.4: Comparison between the original and subsequent experimental setups for the study of the $^{7}\mathrm{Li}(\mathrm{p}, \mathrm{e}^{+}\mathrm{e}^{-})^{8}\mathrm{Be}$ reaction. The setup when the anomaly was first detected (a) employed five $\Delta E - E$ telescopes, each equipped with a multiwire proportional chamber (MWPC) to determine particle positions. In the more recent setup that confirmed the anomaly (b), six telescopes were used, and the MWPCs were replaced by double-sided silicon strip detectors (DSSDs) [27].

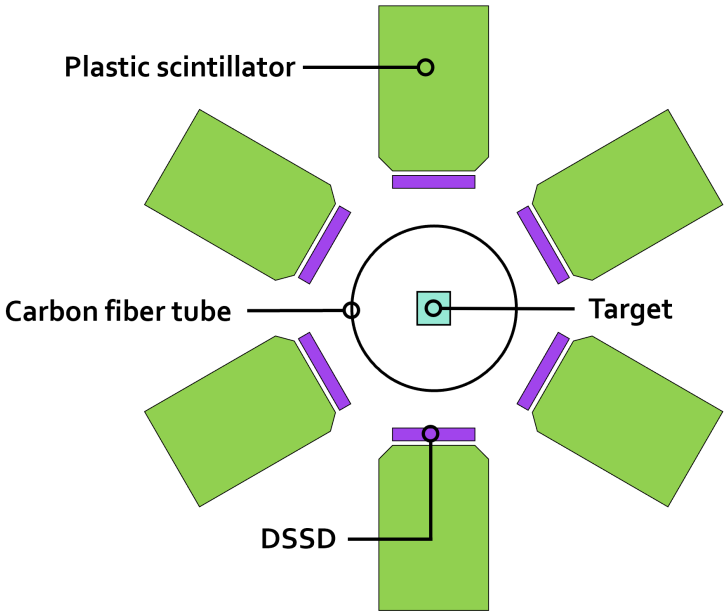

Figure 1.5: Scheme of the updated detection setup used for the search of the X17 anomaly at ATOMKI [29].

Several experimental observations strongly support the hypothesis that the ATOMKI anomaly is a genuine effect:

- The statistical significance of the observations consistently exceeds 6 standard deviations.
- The anomaly has been detected in ^{8}Be* using two different experimental setups: a 5-arm and a 6-arm spectrometer.
- It has been observed with different position-sensitive detectors, including MWPCs and DSSDs.
- The anomaly has been identified in two distinct target nuclei, ^{8}Be and ^{4}He, appearing at different angles in each case ($\Theta \approx 140^{\circ}$ and $\Theta \approx 115^{\circ}$, respectively).
- It has been detected across varying proton beam energies.
- The anomaly was not observed in calibration atoms, such as ^{16}O, during the same data collection period.
- It was not observed in events involving asymmetric momentum $e^{\pm}$ pairs.

Despite the consistency of these observations, additional experimental data is necessary to fully understand the nature of this anomaly. Consequently, many experiments worldwide are either actively searching for this particle in different channels or planning to do so. Some experiments have already placed constraints on the coupling of this hypothetical particle with ordinary matter, while others, still in the R&D phase, are expected to offer additional understanding in the future.
Among them, the study of the neutron-induced reaction $^{3}\mathrm{He}(\mathrm{n}, \mathrm{e}^{+}\mathrm{e}^{-})^{4}\mathrm{He}$ is thought to be complementary to the one of Eq. 1.2 and will be performed at the n_TOF facility at CERN. A detailed description of the proposed experimental setup is found in Chapter 3.

1.3 Theoretical interpretations

Assuming that the observed anomalies are not due to underestimated experimental uncertainties (which still need to be ruled out through different and independent measurements), many theoretical efforts have been made to interpret the observed signals. While no single explanation has been definitively established, the anomalies could potentially be attributed to unaccounted effects within the Standard Model [30–33] and/or nuclear physics [34–36], or they might indicate physics Beyond the Standard Model.
In the latter case, several scenarios have been proposed, interpreting the anomalies within the framework of a light and weakly coupled dark sector, possibly connected to Dark Matter physics. With the current experimental data, only a few theoretical interpretations can be entirely ruled out, highlighting the need for further investigations.

As already anticipated, one possible explanation is the existence of a light boson with a mass of $17\,\mathrm{MeV/c^2}$, referred to as the X17 boson. The observed excesses in the three reactions described in Eq. 1.1, Eq. 1.2, Eq. 1.3, are resonant bumps at the same $e^{\pm}$ invariant mass, within experimental errors.
Additionally, the $e^{\pm}$ opening angles in the anomalous peaks vary consistently with the kinematics of a $17\,\mathrm{MeV/c^2}$ boson decaying into a lepton pair [37].
For these reasons, one of the earliest explanations for the observed anomalies has been proposed as the effect of the creation of a on-shell $J^{\pi} = 1^{+}$ Gauge boson and its subsequent decay into $e^{\pm}$ pairs [1, 24, 25]. Based on results from the NA48/2 experiment, which did not observe dark photon A' production through the $\pi^0 \to A' + \gamma$ decay followed by the prompt $A' \to e^+e^-$ decay [38], it is required that the X17 boson couples more strongly with neutrons than with protons, exhibiting a so-called "protophobic" behaviour. It was also noted that the existence of a vector X17 boson could resolve the discrepancy between experimental data and the Standard Model predictions regarding the magnetic moment of the electron and muon [39].
Another interpretation of the experimental results suggests the existence of a pseudoscalar ($J^{\pi} = 0^{-}$) particle. In the ^{8}Be case, this predicts that the branching ratio for the 17.6 MeV transition would be ten times smaller than for the 18.15 MeV one, in good agreement with the observations [40].
Subsequent studies have explored different extensions of the Standard Model, including a two-Higgs-doublet model [41–43].
However, as previously mentioned, due to the limited experimental information, it is not possible to definitively establish the cause of the observed anomalies. At present, considering all measurements, it is not possible to establish the quantum numbers of the X17 boson, the intensity of the coupling constant ϵ_e and its peculiarities.
Figure 1.6 shows the ATOMKI result for ^{8}Be (blue line) in the (m_X, ϵ_e) parameter space, which denote the hypothetical X17 mass and its coupling constant to the electron, respectively. The result is consistent with the regions of the parameter space excluded by other experiments (in gray). The coloured contours depict the sensitivity of different experiments to detecting dark photons, without any assumption of "protophobicity", which can set more stringent constraints.

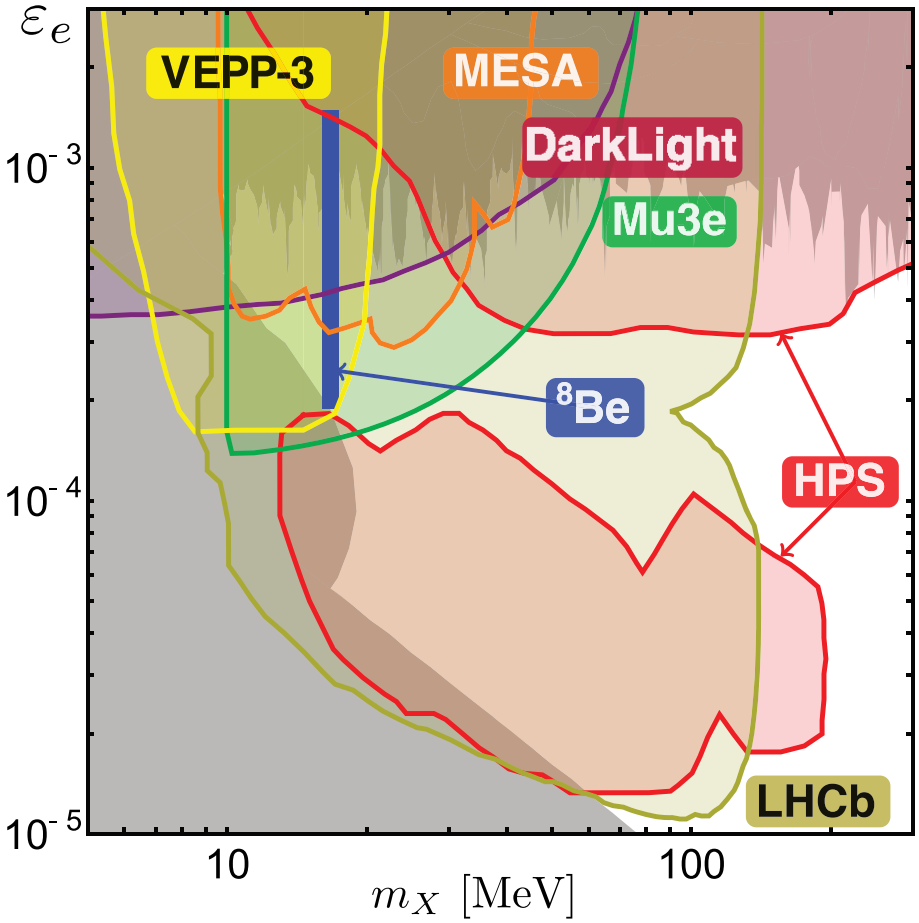

Figure 1.6: The ^{8}Be signal region (blue line) in the (m_X, ϵ_e) parameter space. The excluded parameter space assuming a protophobic coupling is also shown (gray area). The coloured areas show the sensitivity for the dark photon search of several experiments [25].

Chapter 2

The n_TOF facility

The neutron Time Of Flight facility, n_TOF, became operational at CERN in 2001, based on an idea by C. Rubbia [44]. Since then, it has become one of the most important facilities for measuring cross-sections of neutron-induced reactions.
Nuclear data, particularly neutron-induced reaction cross sections, are relevant across a broad spectrum of research fields. They are essential for the safety and criticality assessment of nuclear technologies, not only for current power reactors but also radiation dosimetry, medical applications, nuclear waste transmutation, accelerator-driven systems (ADS), fuel cycle studies, and the development of future reactor systems, such as those in Generation IV or fusion reactors.
Moreover, nuclear data are necessary for research areas like nuclear level density studies and stellar nucleosynthesis. The simulations and calculations used in nuclear technology applications heavily depend on evaluated nuclear data libraries. These libraries are derived from both experimental data and theoretical models. Experimental nuclear reaction data are globally compiled by the Nuclear Reaction Data Centres (NRDC) network in the EXFOR database, which serves as a critical link between nuclear data measurements and the evaluated data libraries. Throughout the years of its scientific program, n_TOF has contributed significantly to produce unique data used and integrated in modern nuclear data libraries [45–47].

2.1 The Time Of Flight concept

The neutron energies of interest range from thermal (25 meV) to hundreds of MeV, depending on their application. In this energy range, neutron cross-sections exhibit resonant structures that vary significantly from isotope to isotope and cannot be predicted, thus requiring high energy resolution to distinguish these structures.

A useful method for this purpose is the time-of-flight (TOF) technique, where a pulsed beam of neutrons, distributed over a wide energy range, travels a specific distance L before reaching the sample under study. In this way, the kinetic energy of the neutrons is determined by their arrival time t at the measurement station. Given the velocity $v = L/t$, the kinetic energy can be expressed as:

$$E_n = E - mc^2 = \sqrt{p^2c^2 + m^2c^4} - mc^2 = mc^2(\gamma - 1) \tag{2.1}$$

where $\gamma = (1 - v^2/c^2)^{-1/2}$ is the Lorentz factor. The first term of the series expansion provides the classical expression for kinetic energy, valid in the non-relativistic regime:

$$E_n = \frac{1}{2}mv^2 \tag{2.2}$$

Regarding the energy resolution, it can be evaluated as:

$$\frac{\Delta E_n}{E_n} = \gamma(\gamma + 1)\frac{\Delta v}{v} = \gamma(\gamma + 1)\sqrt{\left(\frac{\Delta t}{t}\right)^2 + \left(\frac{\Delta L}{L}\right)^2} \tag{2.3}$$

The ability to resolve resonant structures in cross-sections is thus favored by the use of long flight paths (large L and t) and by producing neutrons in the shortest possible time (Δt) and space (ΔL) intervals.
Several facilities worldwide currently use this technique to measure neutron-induced reaction cross-sections, with different neutron production methods and flight paths ranging from one to 400 meters. Among these, the n_TOF facility stands out, particularly for its high instantaneous neutron flux, wide energy range and excellent energy resolution. The facility began its first operational phase between 2001 and 2004. After a four-year shutdown for an upgrade of the neutron production target, operations resumed in 2008. A shutdown between 2012 and 2014 allowed for the construction of a second 20-meter flight path (EAR2), complementing the original 185-meter path (EAR1). In 2021, an additional experimental station was added (NEAR), along with further upgrades to the neutron production target.
Figure 2.1 depicts the relation between the neutron kinetic energy and its time-of-flight for the beamlines EAR1 and EAR2, using Eq. 2.1.

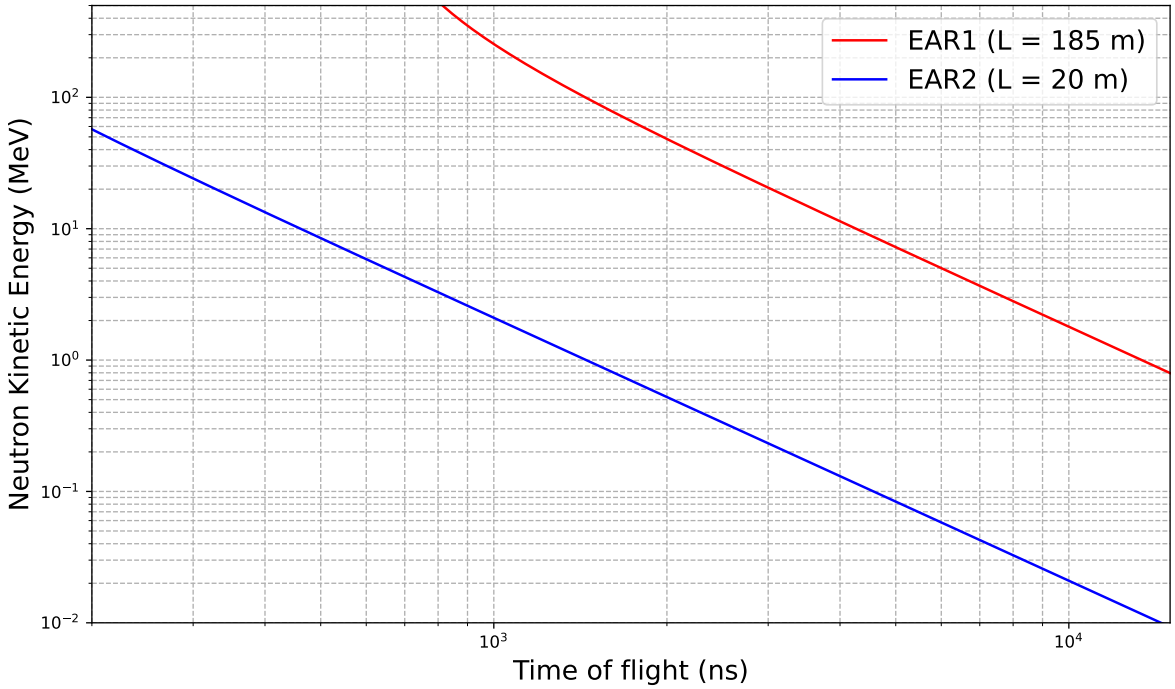

Figure 2.1: Relation between incident neutron kinetic energy and its corresponding time-of-flight for the beamlines EAR1 and EAR2 at the n_TOF facility.

2.2 Neutron beam

The n_TOF facility is part of the fixed-target experimental program of the CERN accelerator complex, as shown in Figure 2.2. The LINAC supplies the PS-Booster, which provides the PS (Proton Synchrotron) with protons of 1.4 GeV/c, finally accelerated up to 20 GeV/c. This beam is extracted and sent to the neutron production site of n_TOF in bunches of 7×10^{12} protons.
Neutron facilities such as n_TOF require a stable and sufficiently intense neutron source to conduct the desired experiments. In the context of nuclear physics experiments, several methods and physical phenomena have been employed to generate neutron beams. However, the practical requirements for increasingly intense neutron fluxes, particularly for scattering experiments, limit the available options for neutron sources and require increasingly advanced technological efforts. The n_TOF facility generates its neutron beam through the spallation process, where protons from the PS are impinged onto a lead target. The following subsections detail the physical process and provide technical information on the spallation target used at n_TOF. Its careful design, coupled with the TOF technique, is what establishes n_TOF as a top-tier neutron facility, thanks to the aforementioned neutron beam characteristics.

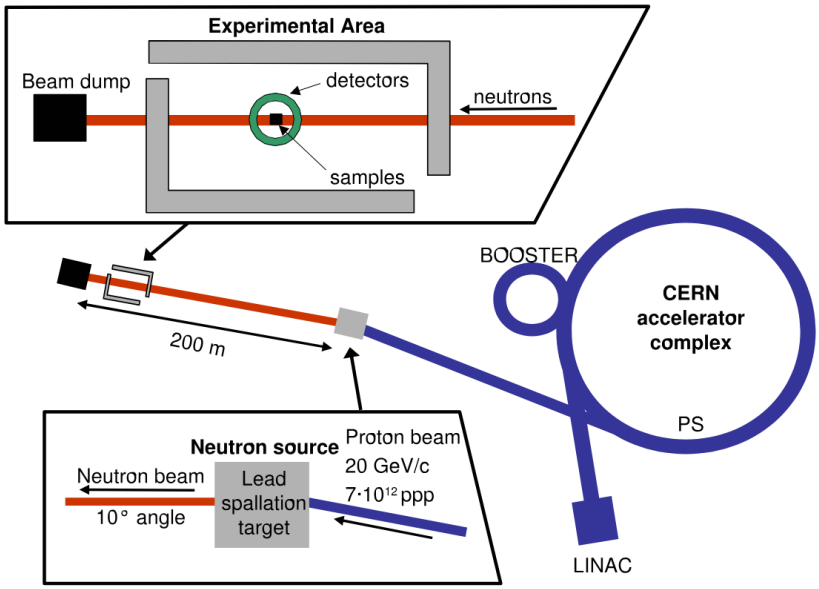

Figure 2.2: Diagram of the n_TOF EAR1 facility along with the neutron production site and the CERN accelerator complex [45].

2.2.1 The spallation process

If nuclei are created with excitation energy greater than the neutron binding energy, they can decay by emitting a neutron; however, these highly excited states are not produced as a result of any convenient radioactive decay process (i.e. with sufficiently long half-lives). For this reason, isotopic neutron sources do not exist, unlike, for example, the production of γ rays, which can be obtained using various nuclei that undergo β decay. The choice of radioisotopes as neutron sources is therefore very limited and is based either on spontaneous fission or on nuclear reactions in which the incident particle is the product of a conventional decay process [48]. Since α particles are the only low-Z charged particles available from processes involving radioisotopes, reactions that instead need incident protons, deuterons, etc. to produce neutrons must rely on artificially accelerated particles.
The reaction exploited at the n_TOF facility, spallation, also uses accelerated charged particles. It is a nuclear reaction that occurs when high-energy particles bombard the nuclei of heavy atoms. The process occurs only above a certain threshold energy of the incident particle, typically on the order of hundreds of MeV [49]. The reaction, involving the temporary incorporation of the incident particle by the target nucleus, is a sequential process. Initially, there is an intranuclear cascade within the excited target nucleus, followed by an internuclear cascade when high-energy particles, including neutrons, are expelled and absorbed by other nuclei; finally, the various target nuclei de-excite following

the emission (known as "evaporation") of several lower-energy neutrons and various types of nucleons, photons, and neutrinos. A schematic of the process is shown in Figure 2.3.

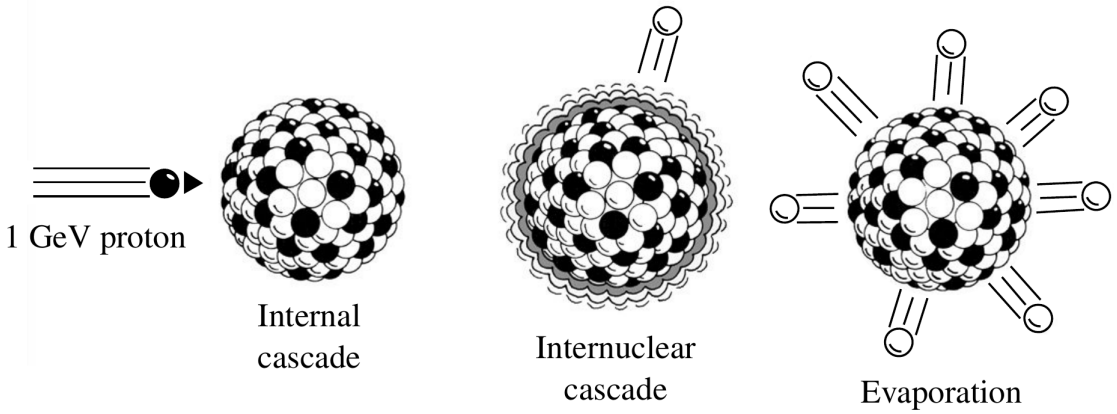

Figure 2.3: Schematic of a spallation process, where a high-energy proton interacts with a heavy nucleus. A large number of neutrons are evaporated with energies of several MeV in a single process involving multiple nuclei [49].

In particular, numerous energetic photons are emitted in spallation processes, mostly originating from the decay of the produced pion decays. These photons constitute the so-called γ-flash: they reach the detectors at the speed of light before any other particles originating from the spallation target, thus saturating the signal produced by the detection system and obscuring the acquisition of other particles until standard operating conditions are restored. In general, at n_TOF the de-excitation of nuclei in the lead target and neutron capture in the lead and moderation layer produce both fast and delayed γ-flashes, resulting in a γ-flash that can last up to several hundred ns. While γ-flash events cause a so-called "dead time" before particle detection, this characteristic also provides a method for time calibration of the detectors used.
In the spallation reaction, many neutrons are produced per incident particle: the actual yield depends on the target material, geometry and the energy of the incident particle.

2.2.2 The spallation target

At n_TOF, an average of 350 neutrons are produced per incident proton. Every 1.2 seconds, a high-intensity neutron pulse is produced from spallation reactions induced by pulses of 7×10^{12} protons, with momentum of 20 GeV/c, on a lead target. The time width of each pulse is 7 ns (rms), allowing for excellent energy resolution of the produced neutron beam even for the highest neutron energies.

Until 2021, the target weighed 1.3 t, was 40 cm long, and had a diameter of 60 cm. A 1 cm layer of water cooled the target and, together with an additional 4 cm layer of borated water (H_2O + 1.28% H_3BO_3, mass fraction), moderated the neutrons to the desired energy spectrum, down to thermal energy. These two separated layers represented the main innovation compared to the first configuration used from 2001 to 2004.
The previous configuration, in fact, used a single 5.7 cm layer that served both as a coolant and a neutron moderator. However, the spallation target had to be replaced due to corrosion caused by insufficient cooling. With the configuration in place from 2008 to 2021, on the other hand, the moderation role was mainly performed by borated water, which also helps minimize neutron capture by hydrogen, thus reducing the production of 2.2 MeV γ-rays. These γ-rays are responsible for significant background in cross-section measurements for neutron capture in the keV energy range [50]. A model of this spallation target can be seen Figure 2.4.

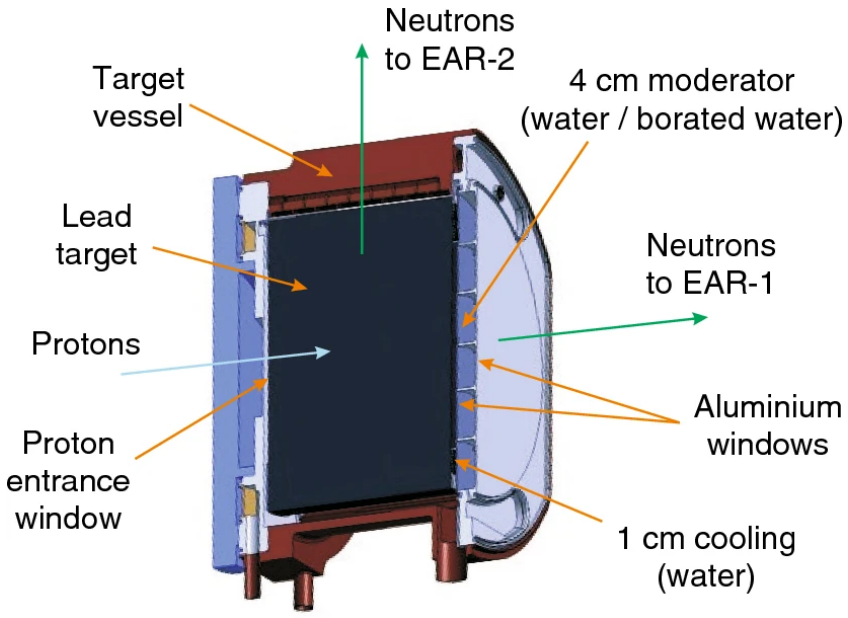

Figure 2.4: The cross-section of the n_TOF lead spallation target present until 2021 [45]. The separation of the cooling layer (water) from the moderator layer (borated water) is achieved by a thin aluminum window.

In April 2021, the spallation target was replaced again due to its prolonged use [51]. As a third-generation target, six separate U-shaped lead blocks were chosen, with a total weight of 1.5 tonnes. The new design provides several logistical advantages: first of all, it allows the cooling of the lead target, overheated by the proton beam, with gaseous nitrogen at room temperature instead of water, thus preventing circuit deterioration by completely eliminating the erosion and corrosion mechanisms caused by direct contact

between water and lead. Additionally, the new target allows the containment of an additional moderator tank filled with demineralized water at the top, along the EAR2 neutron detection direction. This arrangement improves the energy resolution of neutron TOF measurements along the vertical direction. Finally, the new configuration improves the physical performance of the facility [52]. In the latest intervention, a new shielding around the target was also installed to provide access to the target area for inspections and technical operations, as well as to allow the installation of a new experimental test station (NEAR) much closer to the spallation target than the two previously existing ones (EAR1 and EAR2): this proximity significantly increases the measurable number of neutrons per proton pulse. The new spallation target is shown in Figure 2.5.

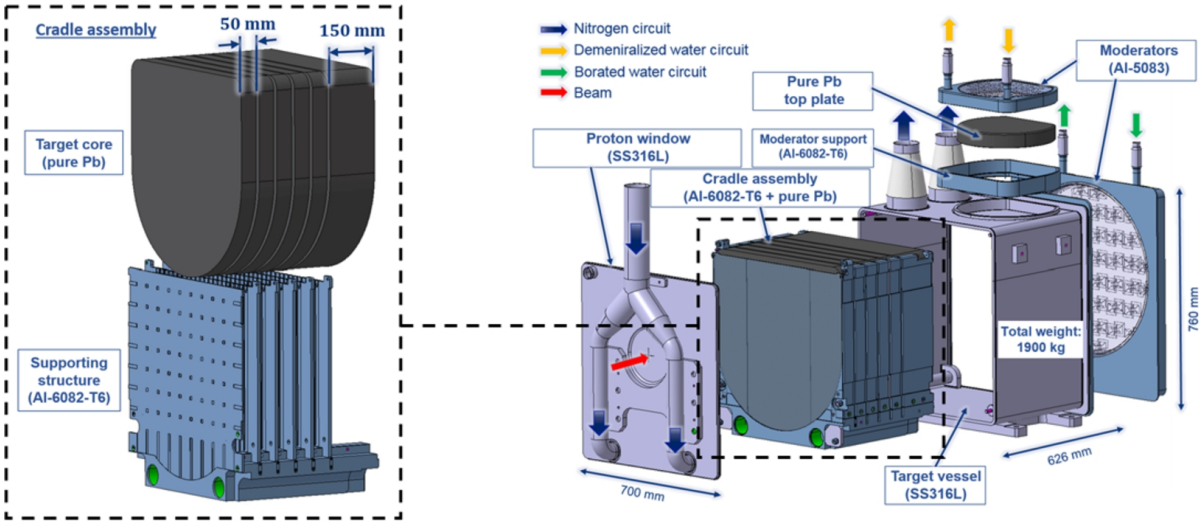

Figure 2.5: Exploded view (3D model) of the new third-generation spallation target installed in April 2021 at the n_TOF facility [53]. On the left, the support structure is shown, and on the right, the entire target is depicted.

2.3 Experimental halls

The n_TOF facility is currently equipped with three beamlines and experimental stations: EAR1, EAR2 (shown in Figure 2.6), and NEAR. Each of these halls is optimized for specific types of measurements and detection systems. EAR1 and EAR2 use the TOF technique, while NEAR is best suited for activation measurements and radiation-damage studies.

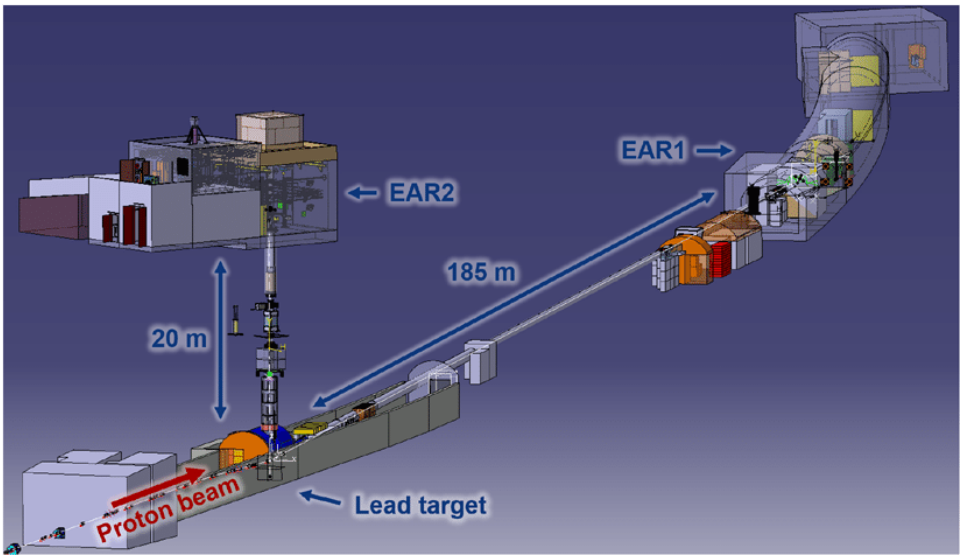

Figure 2.6: Scheme of the n_TOF facility as before 2021, with the two beamlines and experimental halls (EAR1 and EAR2) that use the TOF technique [54].

In the TOF beamlines (EAR1 and EAR2), charged particles are removed from the beam using "sweeping magnets", while collimators and additional shielding elements define the beam aperture. The final beam diameter in both areas is set by a shaping collimator located just before the experimental area. Two beam aperture options are available for each area, and the beam optical elements ensure a well-defined and sharp spatial profile of the neutron beams, optimizing for low background conditions. A schematic of the beamline, in the case of EAR1, is shown in Figure 2.7.
To study the experiments of interest at n_TOF, a variety of detection systems are available for analyzing different reaction types. Solid and liquid scintillators are mainly used for detecting γ rays following (n, γ) reactions, while gaseous and solid-state detectors are employed to measure $(n, \text{charged particles})$ reactions. Fission reactions are monitored using gaseous detectors.
The use of well-characterized detector configurations and well-known reference reactions also enables real-time monitoring of neutron beams, allowing for on-the-fly calibration and correction of data, and enhancing the overall quality of data analysis.
In general, characterizing the neutron flux in the experimental areas is a challenging task, as it requires covering a range of neutron energies spanning over eleven orders of magnitude. To achieve the highest possible accuracy, it is essential to adopt different experimental setups and reference reactions [55]. In Table 2.1 some of the detectors used at n_TOF for this purpose are listed.

Detector	Purpose	Reactions
Micromegas	flux, spectrum	^{235}U(n, f), ^{10}B(n, α)
PPAC	flux, beam profile	^{235}U(n, f)
Silicon monitor	flux, spectrum	^{6}Li(n, t)
PTB fission chamber	flux, spectrum	^{235}U(n, f)
C_6D_6	energy resolution	^{197}Au(n, γ), ^{nat}Ir(n, γ), ^{235}U(n, γ), ^{nat}Fe(n, γ), ^{nat}Si(n, γ), ^{77}Se(n, γ)
Timepix	beam profile	n-p elastic scattering

Table 2.1: Adopted experimental setups, purposes and exploited reactions for the commissioning of the latest phase of the n_TOF facility [55].

The integration of these detection systems, along with an acquisition system based on fADCs and the excellent properties of the neutron beams produced at n_TOF, enables the precise measurement of a large number of cross sections and contributes significantly to technical advancements in this field of research.
A brief description of each experimental hall, together with its main strengths, is provided in the next subsections.

2.3.1 EAR1

The EAR1 experimental area is located 182.3 m from the spallation target and is 7.9 m long. The neutron beamline is inclined by 10° relative to the proton beam, in order to reduce the typical γ-flash that affects the neutron production by spallation.
The EAR1 area is designed for high-resolution measurements, particularly in the resonance regions, and to extend the measurement of neutron-induced reaction cross sections at high neutron energies (up to GeV).

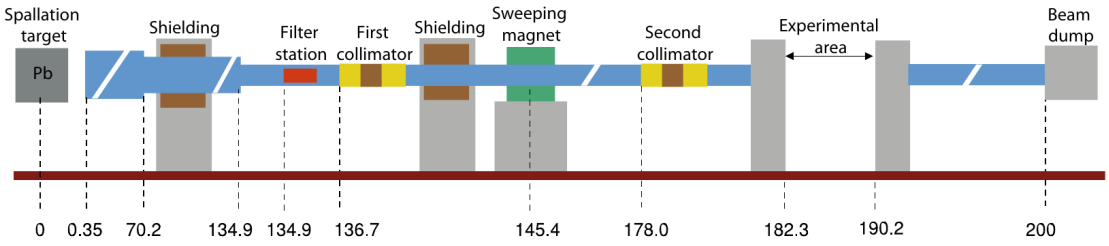

Figure 2.7: Schematic of the neutron beamline of n_TOF in the EAR1 area, from the spallation target to the beam dump (distances are in meters) [45].

2.3.2 EAR2

The EAR2 experimental area is located at the end of the beamline that extends vertically for 20 meters from the top of the target, as shown in Figure 2.8.

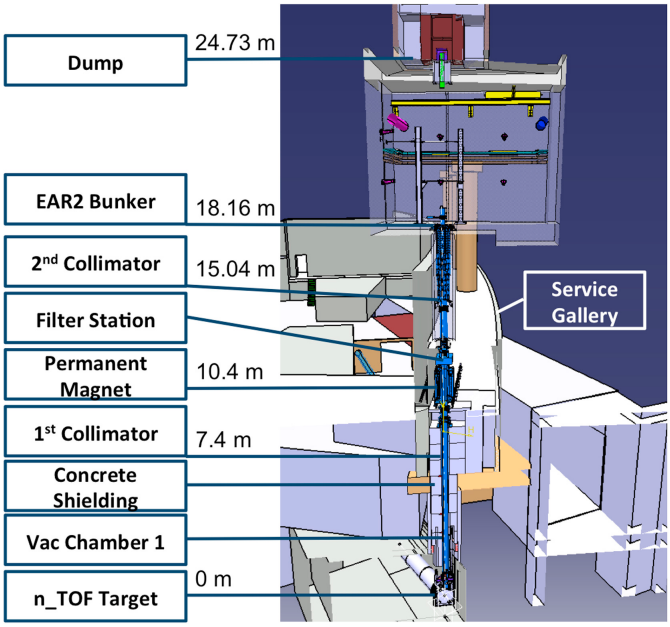

Figure 2.8: Schematic of the vertical neutron beamline of n_TOF in the EAR2 area, from the spallation target to the beam dump [56].

It was designed starting in 2012 and constructed because, compared to the first area, EAR1, it offers several advantages in specific research fields:

- The neutron flux is significantly higher ($\approx$ 30 times);
- Neutron-induced reaction measurements can be performed on small samples, leading to reduced activity in unstable samples and cost savings when purchasing rare samples;
- Measurements can be conducted on isotopes with very small cross-sections;
- The entire neutron energy range is measured in a shorter time interval ($\approx$ 10 times). Consequently, for measurements on radioactive nuclei, fewer background detector signals are due to radioactivity. Combined with the higher neutron flux, this leads to a signal-to-noise ratio 300 times higher than EAR1 [46];
- Measurements of neutron-induced reaction cross-sections at high energies ($\gtrsim$10 MeV), which are challenging to perform in EAR1, become feasible due to the attenuation of the γ-flash.

Regarding the last point in particular, some of the fast γ-flash signals are not visible because that they are not caused by the de-excitation of nuclei in the spallation target, but by the decay of fast particles in flight that follow the horizontal beamline, thus excluded from the EAR2 beamline. These fast γ-flashes primarily originate from the decay of neutral pions (π^0), generated by nucleon-nucleon collisions in intranuclear cascades [57]. Since the momentum of neutral pions is mostly directed along the proton beam in the laboratory frame of reference, the same applies to the γ rays: they can therefore follow the horizontal beamline towards EAR1, but very few can reach EAR2.
Recently, the EAR2 area has also been used to study neutron imaging, a technique similar to X-ray radiography but differing in its ability to highlight the structures of light materials due to the unique interactions between neutrons and matter [58].
The energy distributions of the total neutron flux are illustrated in Figure 2.9 for both EAR1 and EAR2. The neutron flux exhibits a Gaussian beam profile with a nominal full width at half maximum (FWHM) of 18 mm in EAR1 and 21 mm in EAR2 when using the small collimator typically employed for capture measurements [46].

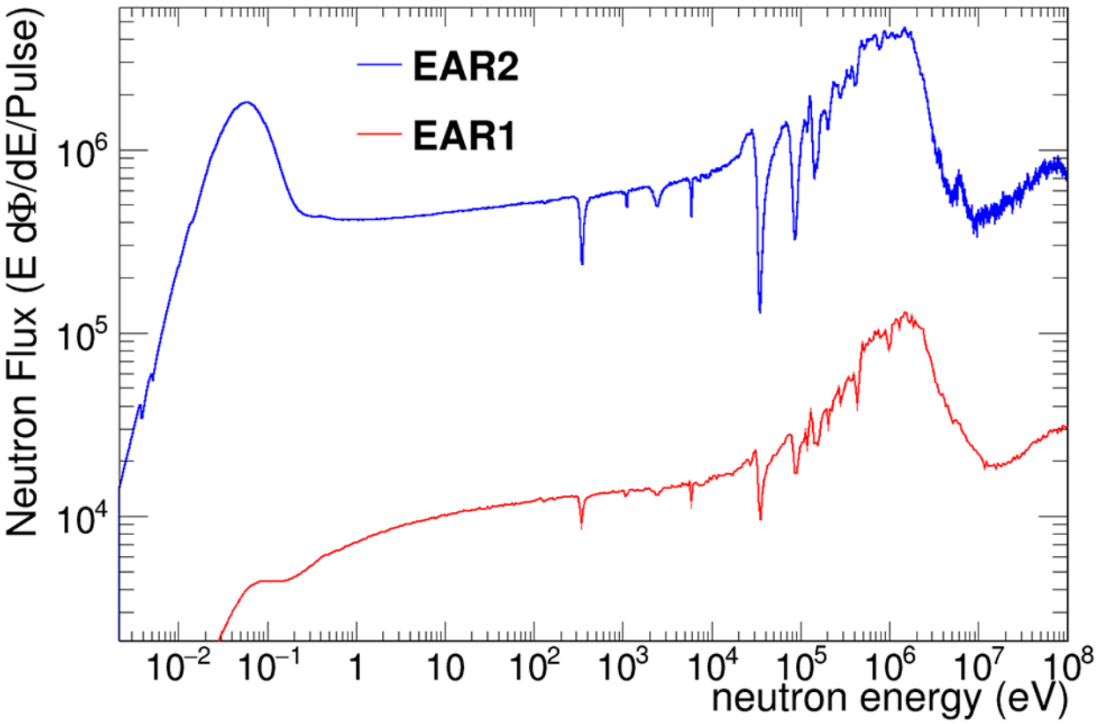

Figure 2.9: Neutron "flux", i.e. counts per proton bunch (7×10^{12} protons) on spallation target, as a function of the neutron energy, measured in EAR1 and EAR2 before 2021. The significant reduction of the thermal peak in EAR1 is due to the ^{10}B-loaded moderator [50, 59].

Some differences in the characteristics of the neutron beam measured in the two experimental areas are summarized in Table 2.2.

	EAR1	**EAR2**
Neutron flux [n/(cm^2 bunch)]	$\approx 2 \times 10^5$	$\approx 5 \times 10^6$
Energy spectrum	meV–1 GeV	meV–0.1 GeV
Energy resolution $\Delta E/E$ at 1 eV	10^{-4}	10^{-3}

Table 2.2: Characteristics of the n_TOF neutron beam in the two experimental areas EAR1 and EAR2. The beam repetition rate is the same as that of the incident proton beam, with a minimum of 1.2 s, to avoid overlap in TOF measurements [58].

The 2021 upgrade of the spallation source has significantly imrpoved the neutron beam quality at EAR2 in terms of flux, energy resolution, and beam profile. In particular, the instantaneous neutron flux increased by 45% in the epithermal region and evaporation peak, and by 25% at the thermal peak [60].

2.3.3 NEAR

The most recent experimental area, NEAR, became operational in July 2021 and is depicted in Figure 2.10. This area consists of two sub-areas: the irradiation station (i-NEAR), located adjacent to the spallation target, and the activation station (a-NEAR), positioned just outside the shielding, approximately 3 m from the target [61]. By placing the experimental setup so close to the spallation target, an extremely high neutron flux is achieved, allowing measurements on very small samples and extremely short-lived radioactive isotopes. The neutron beam from the spallation target reaches NEAR through a simple hole in the shielding wall, with the aid of a suitable mobile collimation/moderation system [62]. Due to the proximity to the target, a significant flux of γ rays and charged particles is also present.
This new station allows for the collection of previously scarce or novel data on radiation damage in a neutron-dominated environment, thus enabling an increase in the lifespan of instruments used in high-radiation areas, reducing the risk of failure during operations with accelerators and other similar facilities [63].

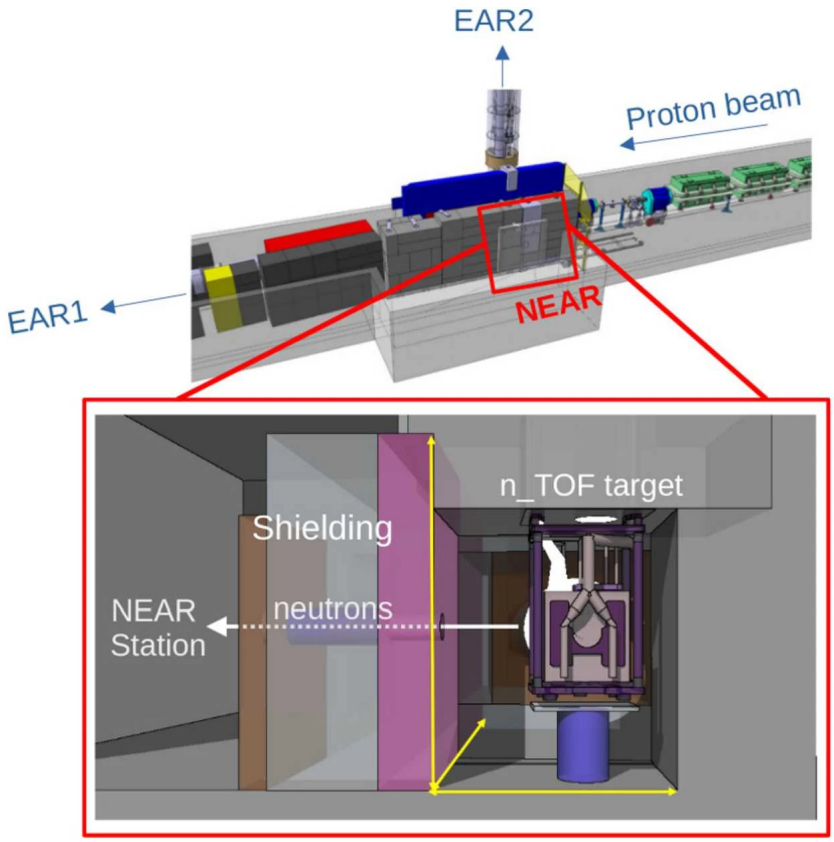

Figure 2.10: Scheme of the newly built NEAR experimental station [55].

Characterizing the neutron beam and experimental conditions at NEAR presents significant challenges. The TOF technique is less effective due to the short distance from the collimator and the wide energy spectrum. Moreover, the harsh radiation environment complicates the use of standard online detectors and electronics for spectrum measurements. To address these issues, a set of offline strategies were implemented to measure the neutron flux at the exit of the NEAR collimator. These strategies include activation techniques, such as Multi-foil Activation Measurements, which probe the full spectrum of interest by using different materials, or a single material combined with a moderating device.
First results indicate that the number of neutrons at the target position in NEAR has increased on average by a factor of ≈ 100 compared to the EAR2 beamline, and by a factor of ≈ 4000 compared to that of EAR1 [64]. Since NEAR can operate in parallel with EAR1 and EAR2, it can contribute to a substantial improvement in experimental opportunities and enable the study of neutron-induced reactions that were previously not accessible.

Chapter 3

The X17 search at n_TOF

To validate or provide an alternative explanation for the ATOMKI claim, it is important to conduct independent measurements by different research groups using different methodologies. New experiments should aim to provide more precise data on the properties of the X17 particle, including its coupling to ordinary matter and quantum numbers J^π. This can be achieved by measuring the charge and four-momenta of electron-positron pairs, performing measurements across a wide energy range, and designing a detection apparatus with large acceptance [29].
For this reason, a new investigation of the $^3\mathrm{H}(\mathrm{p}, \mathrm{e}^+\mathrm{e}^-)^4\mathrm{He}$ process has been proposed, by studying the conjugate reaction $^3\mathrm{He}(\mathrm{n}, \mathrm{e}^+\mathrm{e}^-)^4\mathrm{He}$ using the vertical neutron beam of EAR2 at the n_TOF facility. This chapter outlines the theoretical motivations for studying this reaction, the detector requirements, and a demonstrator prototype of the designed detection system, tested at n_TOF in 2023. The analysis of the data from this test is presented in Chapter 4.

3.1 Theoretical motivations

The study of the $^3\mathrm{He}(\mathrm{n}, \mathrm{e}^+\mathrm{e}^-)^4\mathrm{He}$ reaction at n_TOF is based on theoretical considerations on the nature of the X17 anomaly, guiding the definition and design of the experiment. A diagram showing the energy levels of ^{4}He relevant to this study is presented in Figure 3.1. The spin-parity states of interest, in order of increasing excitation energy, are 0^+, 0^-, 2^-, and 1^-.

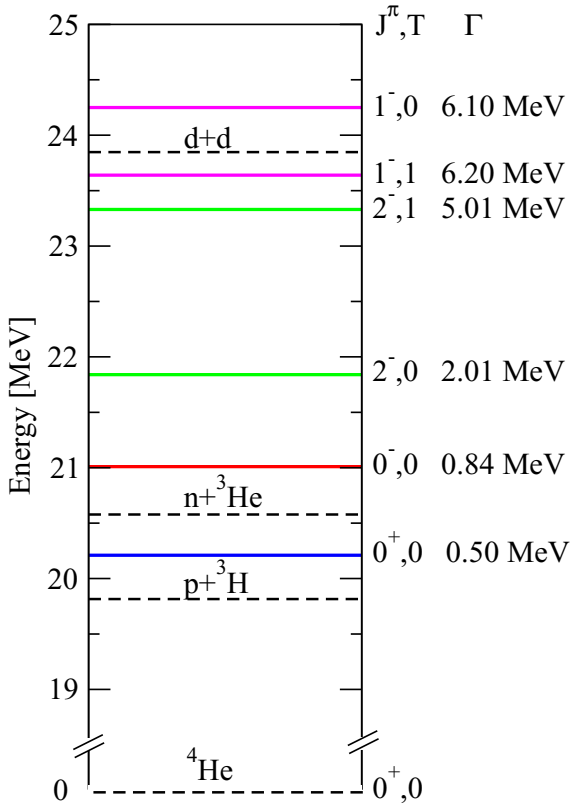

Figure 3.1: The low-energy spectrum of ^{4}He. The dashed lines represent the thresholds for the opening of the 1+3 nucleon and 2+2 nucleon channels, while the solid lines indicate the energies of various resonances, with their corresponding J^{π}, isospin assignments and widths shown on the right [65, 66].

In particular, low-energy $e^{\pm}$ pair production in A = 4 nucleon systems was studied, both as a purely electromagnetic process and by including the contribution of a hypothetical low-mass boson [66]. The calculations were calibrated on the ATOMKI findings, that detected only pairs lying in the plane orthogonal to the beamline ($\theta_k = 90°$). Differential cross sections were calculated for different energies of the incident particle for pairs emitted at $\theta_k = 90°$. Figure 3.2 shows the results of theoretical calculations for different incident nucleon energies as a function of the correlation angle Θ.
With standard model assumptions (i.e. no excess counts) and the existence of a Scalar (S), Pseudoscalar (P), Vector (V) and Axial (A) boson, a structure in the differential cross section can be observed. These excess counts depend on incident proton energy differently in the 4 cases considered (S, P, V, A), thus providing precise indications of the boson's quantum numbers.

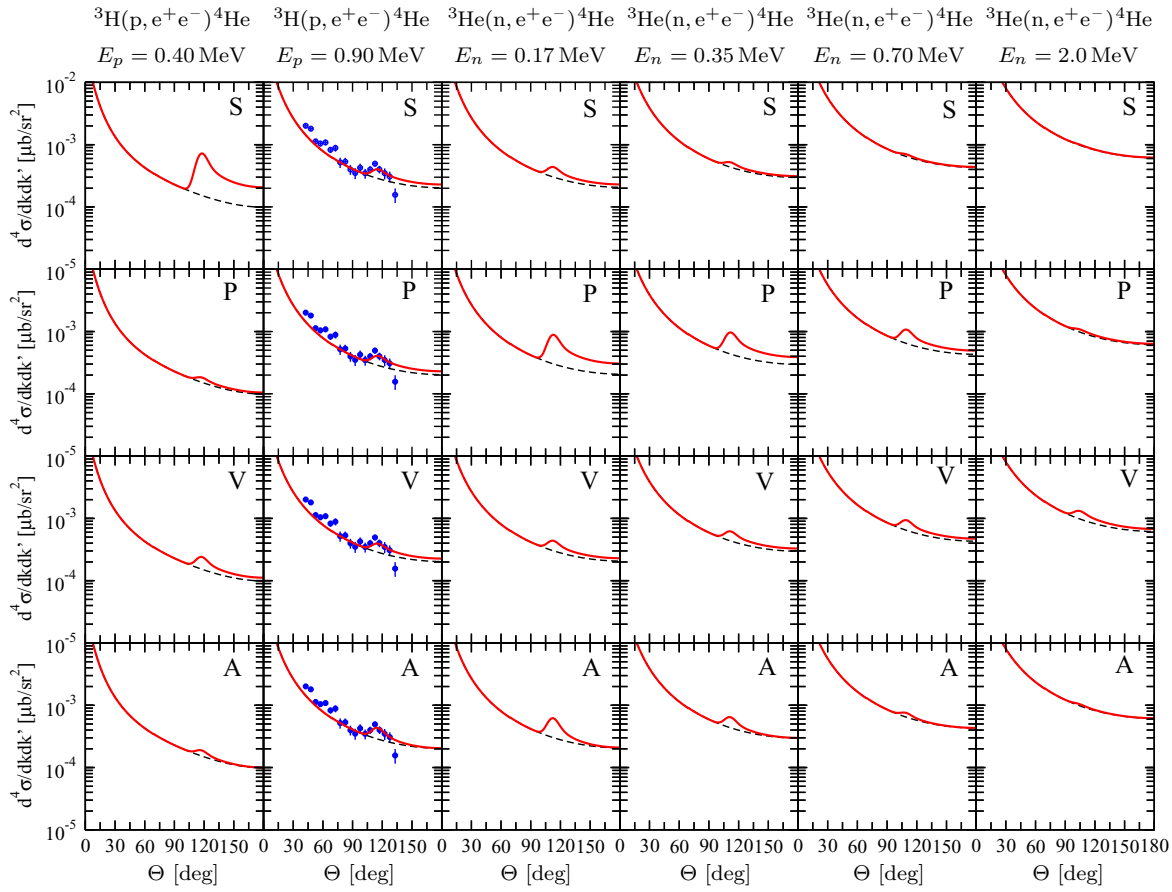

Figure 3.2: Differential cross sections for the ^{3}He(n, e$^+$ e$^-$)^{4}He and ^{3}H(p, e$^+$ e$^-$)^{4}He processes at $\theta_k = 90°$ and six different incident nucleon energies as a function of the correlation angle Θ. The panels labeled S, P, V, and A show the results obtained by assuming a scalar, pseudoscalar, vector, and axial X17, respectively. The dashed (black) and solid (red) curves represent the theoretical results obtained by including the electromagnetic interaction only or both the electromagnetic and X17 amplitudes. The coupling constants have been adjusted to reproduce the ATOMKI ^{3}H(p, e$^+$ e$^-$)^{4}He cross section data at $E_p = 0.90$ MeV (blue dots) [66].

Although the excess of $e^{\pm}$ pairs as a function of energy depends on the quantum numbers of the X17 particle, an experimental setup that detects only particles orthogonal to the beam axis may limit the ability to distinguish between different quantum numbers, and therefore hinder the unique identification of X17 properties. This limitation is evident in Figure 3.2, where the predicted trends of the excess are similar for both the pseudoscalar and axial cases.
To overcome this limitation, it is essential to detect pairs emitted at a wider range of angles θ_k. In fact, employing a detector with a large angular acceptance could make the discrimination between different quantum number configurations possible.

As shown in Figure 3.3, where the cross section at fixed energy ($E_p = 0.9\,\mathrm{MeV}$) was calculated assuming the detection of pairs at different angles ($\theta_k = 60°, 70°, 80°$), the angular distribution of $e^{\pm}$ pairs exhibits an evident dependence on the X17 quantum numbers. In this figure, the first quadrant reproduces the ATOMKI conditions, where $\theta_k = 90°$, and the theoretical curves for scalar, pseudoscalar, vector, and axial X17 bosons are normalized to the data in this configuration.

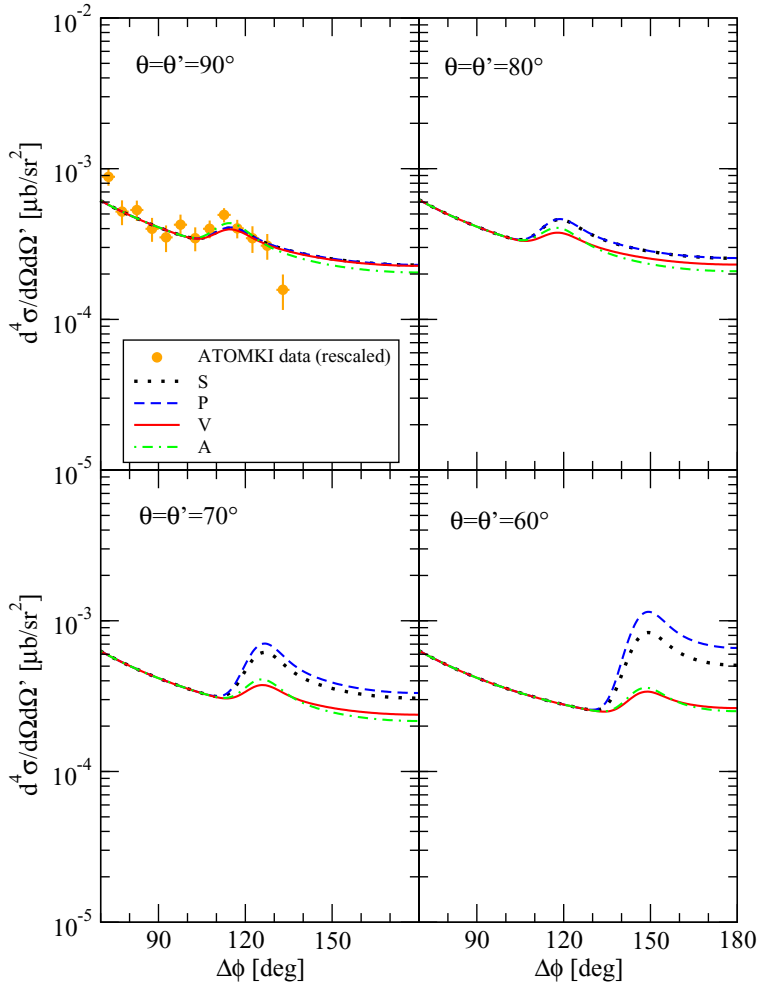

Figure 3.3: Differential cross sections for the $^3\mathrm{H}(\mathrm{p}, \mathrm{e}^+\,\mathrm{e}^-)^4\mathrm{He}$ processes at $E_p = 0.90\,\mathrm{MeV}$ and different emission angle $\theta = \theta' = \theta_k$ with respect to the beamline, as a function of the difference in azimuthal coordinate $\Delta\phi = \phi' - \phi$ of the positron and electron. The curves labeled S, P, V, and A show the results obtained by including the exchange of a scalar, pseudoscalar, vector, and axial X17, respectively. The coupling constants have been adjusted to reproduce the ATOMKI data at $\theta_k = 90°$ (orange dots) [66].

The results indicate that by detecting pairs emitted at different angles, the momentum and parity of X17 can be more precisely identified, as the angular distribution of the pair strongly varies depending on the nature of the X17 boson. This broader angular detection can thus resolve the ambiguity observed in Figure 3.2, and provide clearer evidence of the X17's properties.
In conclusion, a systematic experimental study as function of both the opening angle and electron energy is needed to scan the 0^+, 0^-, 2^-, and 1^- excited levels of ^{4}He (shown in Figure 3.1).
For this reason, the use of a wide range of incident nucleon energies and large detection acceptance is essential. Additionally, a dedicated detector to measure the $e^{\pm}$ pair's four-momenta and provide particle identification would enhance the quality of the experimental data.
In addition to the detector requirements mentioned so far, considerations on the expected signal, assessment of the background sources and their relevance must be done. Table 3.1 shows the relevant neutron beam parameters and count rates for photons, $e^{\pm}$ pairs generated from IPC and from the decay of an X17, assuming protophobic coupling [24, 25] and using the ab-initio calculation described in [66], for a 17 MeV vector boson.
The calculations were performed considering a target of ^{3}He 2 cm long and 2.4 cm in diameter (for a total volume of 5 cm^3) at pressure $P = 380$ bar and temperature $T = 300$ K. Daily counts are estimated by considering an average proton pulse every 5 s.
Assuming removal of the water moderator on the top of the spallation target (depicted in Figure 2.5), an increase in the number of neutrons in the MeV region can be obtained, which is of greater interest in the study of the $^3\mathrm{He}(\mathrm{n}, \mathrm{e}^+\mathrm{e}^-)^4\mathrm{He}$ reaction.

Neutron Energy	**TOF (μs)**	**n/pulse**	**γ/pulse**	**IPC/day**	**X17/day**
1 – 10 eV	411 – 1300	3.0×10^5	2(1)	5569(17)	1(0)
10 – 100 eV	130 – 411	3.3×10^5	2(1)	61(18)	2(0)
0.1 – 1 keV	41 – 130	3.7×10^5	2(1)	69(21)	2(1)
1 – 10 keV	13 – 41	5.8×10^5	3(1)	83(33)	2(1)
10 – 100 keV	4 – 13	2.8×10^6	5(7)	148(208)	4(5)
0.1 – 1 MeV	1.3 – 4	1.5×10^7	36(93)	1154(3003)	29(75)
1 – 10 MeV	0.41 – 1.3	7.8×10^6	26(44)	831(1412)	21(35)
Total		$\mathbf{2.7 \times 10^7}$	**76(148)**	**7915(4712)**	**71(117)**

Table 3.1: Relevant parameters for the measurement of the X17 anomaly at EAR2 of n_TOF. Columns show incident neutron energy, corresponding time of flight, neutrons per proton pulse, and expected events for (n,γ), (n,IPC), and (n,X17) processes. Values in parentheses refer to the case without the water moderator.

The low production cross section for the X17 boson requires a long measurement period: one month of measurement at n_TOF under standard conditions corresponds to about two thousand X17 products. The irreducible background consisting of IPC pairs is about 40 times higher than the signal. However, at large relative angle, this background reduces considerably.
In contrast, the background due to the reaction $^{3}\mathrm{He}(\mathrm{n},\gamma)^{4}\mathrm{He}$ is quite relevant, with a branching ratio of $\mathrm{B}(\gamma/X17) \sim 2 \times 10^{4}$. While this background is easily distinguishable from the X17 events (single electromagnetic shower of about 20 MeV, instead of a $e^{\pm}$ pair at large angles), a detection system with low radiation length is preferable.

3.2 Detectors of interest

The investigation of ^{4}He de-excitation via the $^{3}\mathrm{He}(\mathrm{n},\mathrm{e}^{+}\mathrm{e}^{-})^{4}\mathrm{He}$ process at the vertical EAR2 beamline of n_TOF could either confirm or rule out the existence of the X17 particle, and, if confirmed, provide the opportunity for a detailed study of its properties. Achieving these goals requires an experimental setup that meets the stringent energy range and detector performance requirements described earlier. This section outlines the design and implementation of the detection systems optimized for this study.

3.2.1 Scintillation Detectors

Scintillation detectors are among the most widely used detection instruments today. The physical process they exploit is related to the fact that certain materials, when struck by a nuclear particle or radiation, emit a small flash of light, known as scintillation. When coupled with amplifying devices such as photomultiplier tubes, these scintillations can be converted into electrical pulses that can then be electronically analyzed and counted to provide information about the incident radiation [67].
The general structure of a scintillation detector consists of a scintillating material connected to a photomultiplier (PM) either directly or via a light guide. When radiation passes through the scintillator, its atoms and molecules are excited and emit light as they return to their ground state. This light is directed to the photomultiplier, where, via the photoelectric effect, it is converted into a weak photoelectron current, which is then amplified by an electron multiplier. The resulting current is then analyzed by an electronic system.
Some characteristics that make the scintillator signal ideal for particle and radiation detection are:

- Energy sensitivity: Above a certain energy threshold, most scintillators provide a light emission signal directly proportional to the excitation energy. Since the photomultiplier is also a linear device, the amplitude of the final electrical signal will also be proportional to this energy;

- Fast response time: The signal response and recovery of standard detection conditions occur in very short times in a scintillator. This fast response enables precise timing measurements, such as the time difference between two events, and enables high counting rates since the dead time, i.e. the time lost waiting for the scintillator to return to its initial state, is reduced;

- Pulse Shape Discrimination (PSD) capability: a technique by which it is possible to distinguish different types of particles by analyzing the shape of the emitted light pulses. This is due to the different fluorescence mechanisms triggered by particles with varying ionizing powers. PSD is achievable only with certain scintillators.

The property by which scintillating materials, when exposed to certain types of radiation, absorb it and re-emit it as visible light is known as luminescence. If the re-emission occurs within 10^{-8} s, the order of magnitude of atomic transitions, the process is called fluorescence. However, if the re-emission is delayed, as the excited state is metastable, the process is called phosphorescence, and depending on the material, the re-emission can occur from a few microseconds to hours.
The evolution of the re-emission process can be described by a two-component exponential,

$$N = A \exp\left(-\frac{t}{\tau_f}\right) + B \exp\left(-\frac{t}{\tau_s}\right) \tag{3.1}$$

where τ_f and τ_s are the decay constants.
For most scintillators, one component is generally much faster than the other, and they are thus referred to as the fast component and the slow component. Their relative amplitudes A and B vary depending on the material, but usually, the fast component is dominant. These two components are the basis of Pulse Shape Discrimination previously mentioned.
Among the various scintillating materials, those that can serve as excellent detectors typically exhibit the following properties:

- High efficiency in converting excitation energy into fluorescent radiation;

- Transparency to their own fluorescent radiation to allow light transmission through the medium;

- Emission within an energy range consistent with the spectral response of the photomultipliers with which it would be coupled;

- A short decay constant, corresponding to a faster response.

Plastic Scintillators

Scintillators are categorized based on the materials used: examples include organic scintillators (crystals and liquids), plastics, inorganic crystals, etc.
Organic scintillators are aromatic hydrocarbon compounds containing linked or condensed benzene ring structures. Their strength lies in their very rapid decay time, on the order of a few nanoseconds or less. In these compounds, scintillation light originates from transitions undergone by the free valence electrons of the molecules. These delocalized electrons are not associated with any specific atom in the molecule and occupy the so-called π molecular orbitals. A typical energy diagram of these orbitals is depicted in Figure 3.4.

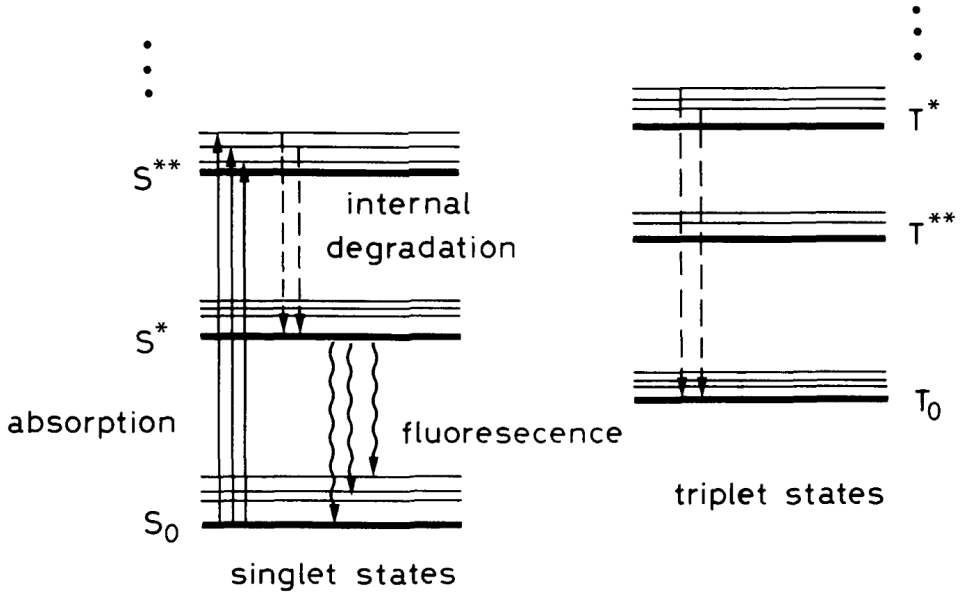

Figure 3.4: Typical energy level diagram of a molecule in an organic scintillator. The singlet states S on the left are separated from the triplet states T on the right [67].

The ground state is a singlet state, S_0. Above this are the excited singlet states ($S^*, S^{**}, ...$), the lowest energy triplet state (T_0), and its excited levels ($T^*, T^{**}, ...$). Each level is also associated with a fine structure due to the molecule's vibrational modes. The energy gap between electronic levels is on the order of a few eV, while that between vibrational levels does not exceed a few tenths of an eV.
The ionization energy from penetrating radiation excites both the electron and the vibrational levels (in Figure 3.4, the process is represented by the solid arrows). Excitations of the singlet states typically decay immediately ($\leq 10\,\text{ps}$) to the S^* state without radiation emission (dashed lines in Figure 3.4) through a process known as internal degradation. From S^*, there is a high probability of undergoing radiative decay to one of the vibrational

states of S_0 (wavy lines in Figure 3.4) within a few nanoseconds: this is the previously mentioned fluorescence process, described by the rapid exponential component in Eq. 3.1. The fact that S^* decays into excited vibrational states of S_0 also explains the transparency of scintillators to their own radiation, as the associated radiation emission has lower energy than that required for the $S_0 \rightarrow S^*$ transition.
For excited triplet states, an internal degradation process, similar to that of singlet states, occurs to bring the system to the lowest energy triplet state. Although transitions from T_0 to S_0 are possible, they are highly forbidden by several selection rules. It is more likely that the T_0 state decays by interacting with other molecules in the same state, according to the process

$$T_0 + T_0 \rightarrow S_0^* + S_0 + phonons$$

Radiation is finally emitted from the S^* level as described above, with a characteristic delay time (on the order of µs) and a lower intensity than that of the singlet state fluorescence.
Organic scintillators are often dissolved in an organic solvent and molded into different shapes, forming plastic scintillators. These detectors have similar scintillation mechanisms to organic scintillators, but the interaction of the incident particle typically excites the polymer rather than the individual scintillating molecules. In plastic scintillators, the energy deposited by ionizing radiation is transferred from the polymer molecules to a solute, which subsequently emits fluorescence in the visible spectrum. Therefore, the polymer matrix must be transparent to the solute's fluorescence emission and capable of efficient energy transfer. This transfer efficiency is a critical parameter in the performance of plastic scintillators, and the choice of solute is essential to optimize this property.
Plastic scintillators are widely used in applications requiring large-volume detectors due to their ease of fabrication into complex shapes and sizes. They are also chosen for their fast response time, low cost, and flexibility in tailoring their chemical composition to optimize for specific applications. Their main disadvantage, compared to inorganic scintillators, is their lower density and atomic number, which result in reduced detection efficiency for high-energy photons and charged particles. Despite this, plastic scintillators are often the preferred choice in many applications, especially where cost, speed, and flexibility are critical considerations.

3.2.2 SiPM

The Silicon Photomultiplier (SiPM) is a sensor designed to detect, quantify, and measure the timing of low-light signals down to the single-photon level. Traditionally, this role has been performed by photomultiplier tubes (PMTs), but SiPMs offer a solid-state alternative that combines the low-light detection capabilities of PMTs with the advantages of a solid-state sensor.
SiPMs exhibit characteristics such as low-voltage operation, insensitivity to magnetic

fields, mechanical robustness, and excellent uniformity of response [68]. These advantages have led to an increasingly widespread use of these sensors in fields such as medical imaging, risk and hazard detection, biophotonics and high-energy physics.
Silicon is an excellent candidate as a photosensor material because it absorbs a wide range of light wavelengths within a thickness of just a few tens of µm.
A photodiode is formed by a p-n junction of silicon, which creates a depletion region free of free-charge carriers. When a photon is absorbed in the silicon, it creates an electron-hole pair. By applying a reverse bias voltage, an electric field is created across the depletion region, which accelerates the charge carriers toward the anode (holes) or the cathode (electrons). This movement of charges results in a net current flow in the reverse-biased photodiode. With sufficiently high electric fields ($> 5 \times 10^5$ V/cm) in the depletion region (which can be achieved depending on the sensor type and the application of a recommended voltage), the accelerated charges gain enough kinetic energy to create secondary electron-hole pairs through a process known as impact ionization. In this way, a single absorbed photon can trigger a self-sustained ionization cascade that spreads through the silicon volume subject to the electric field. The silicon thus becomes conductive (breakdown phase) and amplifies the original electron-hole pair into a measurable macroscopic current flow. This process is known as Geiger discharge, and a photodiode operating under these conditions is called a Single Photon Avalanche Diode (SPAD) in Geiger mode.
The resulting current must be stopped by passive quenching (using series resistors): this causes a drop in the reverse bias voltage seen by the diode (quench) below the breakdown value, thereby halting the avalanche. The diode then recharges to the initial reverse bias voltage and is once again ready to detect other photons. This cycle is illustrated in Figure 3.5.

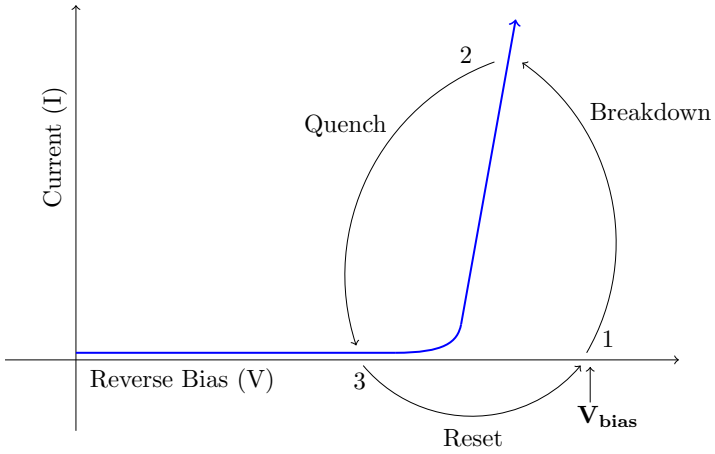

Figure 3.5: Breakdown, quench, and reset cycle of a SPAD sensor in Geiger mode [68].

In this way, a single SPAD sensor in Geiger mode acts as a switch, triggered by a photon, and thus operates in "on" or "off" states. This results in a binary output, which means the signal does not provide information on how many photons were absorbed in a single detection event; therefore, no information proportional to the instantaneous photon flux amplitude is available. To compensate for this lack of proportionality, the SiPM consists of a dense array of small, independent SPAD sensors, each with its own quenching resistor. A SPAD together with its resistor is called a microcell; a typical SiPM features between hundreds and several thousand microcells per mm^2, depending on their size. Each microcell detects photons independently and identically to the others, so the sum of the photocurrents from each combines to form a quasi-analog output that provides information on the instantaneous photon flux.

3.2.3 The μ-RWELL

The μ-RWELL is an advanced gas detector technology, specifically classified as a Micro-Pattern Gas Detector (MPGD). Gas detectors detect and measure ionizing radiation by using a gas-filled chamber. When ionizing particles pass through the gas, they create electron-ion pairs. These charges are collected by two electrodes with different potentials, generating a measurable electrical signal.
To achieve higher spatial resolution and faster response times, modern gas detectors have evolved to reduce the distance between the electrodes that collect the charge. MPGDs use advanced photolithographic technologies to achieve micro-metric distances between electrodes. The reduced electrode spacing, however, increases the risk of electrical discharges or sparks, which can potentially damage the detector and affect its performance. To solve this problem different approaches where adopted. In the case of GEM detectors [69], for example, the gain is divided into several amplification stages, while for the MicroMegas there is a resistive layer above the readout printed circuit board (PCB) to quench the discharge.
The micro-Resistive WELL (μ-RWELL) shares certain similarities with these other MPDGs, introducing some innovations in order to improve compactness, simplicity of construction and assembly while maintaining an optimal time and spatial performance. In Figure 3.6 a schematic representation of the μ-RWELL layout is depicted.

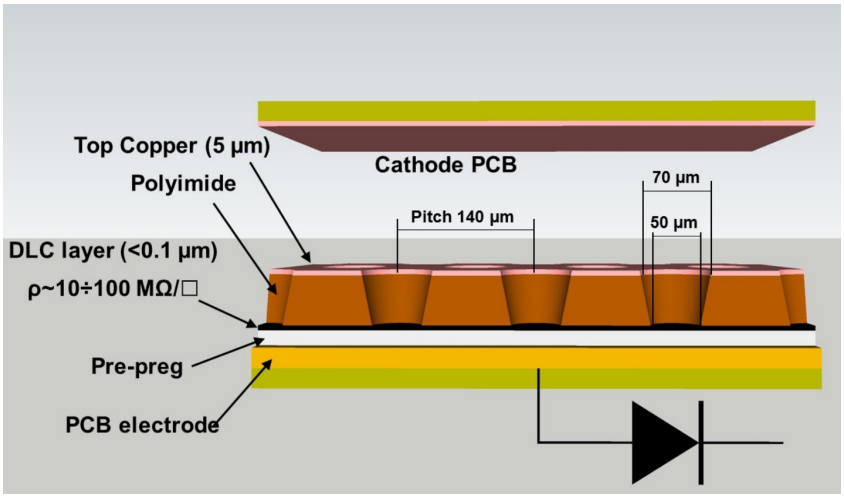

Figure 3.6: Schematic representation of the µ-RWELL layout [70] .

The µ-RWELL gas volume in which the ion-electron pairs are created and drift is delimited by a cathode on one side, made of a PCB with a thin copper layer, and the µ-RWELL PCB on the other. The latter is a multi-layer board composed of a thin layer of polyimide (Kapton®), connected to a readout board via a resistive layer [71]. The polymide layer is generally 50 µm thick and above it a 5 mm copper film is coated.
The amplification of the charges happens inside holes with a diameter of 70 µm and a spacing of 140 µm etched through photolithograpy in the polymide layer. The resistive layer below is a sub-micrometer layer of Diamond Like Carbon (DLC) which has a surface resistivity of the order of tenths of $M\Omega/sq$. When a proper voltage is applied between the copper layer and the DLC, usually grounded, the holes serve as channels that enhance the multiplication of charges produced within the drift zone. The ions produced are then collected by the copper layer above the polymide. The DLC resistive layer between the Kapton® and the readout plane quenches spark amplitudes and also allows the detector to operate safely at higher voltages and achieve higher gains. Thanks to this, the µ-RWELL can reach a maximum gain up to approximately 6000 with a voltage gap in the amplification region of 525 V, which is substantially higher than the gain achieved by a single GEM under similar conditions. Moreover, all electrons produced in the µ-RWELL's holes contribute to signal formation, unlike in GEM detectors where only about 50% of the charge contributes due to extraction inefficiencies [72].

3.3 Experimental setup

As previously mentioned, the study of the $^3\mathrm{He}(\mathrm{n}, \mathrm{e}^+\mathrm{e}^-)^4\mathrm{He}$ reaction requires a detector with large acceptance, capable of reconstructing the kinematics of the $e^\pm$ pairs, while

also having low sensitivity to photons and neutrons. The designed experimental setup is schematically illustrated in Figure 3.7.
It consists of a ^{3}He target of about 10 cm^3, contained in a 1-mm-thick carbon-fiber capsule. The ^{3}He is at a pressure of 358 bar and room temperature, giving a density of about 1.04×10^{22} atoms/cm^3.
The ^{3}He target is surrounded by a tracker consisting of 4 µ-RWELL detectors, each with an active surface area of 380 mm × 460 mm, and 4 planes consisting of scintillating bars. Each plane is made up of 20 scintillating bars of dimensions 3 mm × 20 mm × 500 mm. The µ-RWELL detectors are designed to operate effectively in Time Projection Chamber mode (as explained in Section 3.3.3), allowing for the reconstruction of electron and positron tracks in 3D. The trigger for the µ-RWELL chambers is provided by the 4 planes of scintillators. Additionally, the scintillators measure the neutron time of flight from the spallation source, from which the neutron energy can be deduced.
Finally, the target and detectors are placed inside a square-section coil that generates a 500 Gauss magnetic field parallel to the beamline. This field induces curvature in the electron and positron tracks in the plane orthogonal to the beamline, enabling the determination of their charge and the measurement of their momentum.

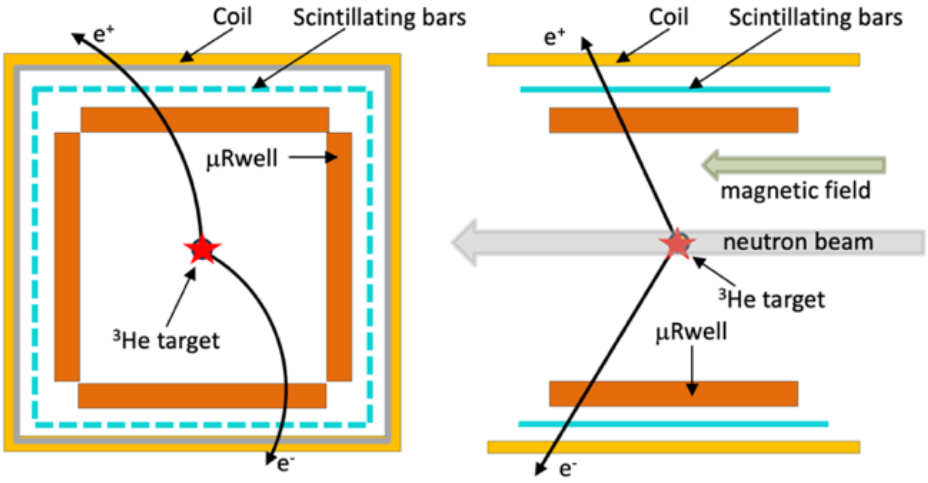

Figure 3.7: Schematic diagram of the designed experimental apparatus for the study of the ^{3}He$(n, e^+e^-)^4$He reaction [29].

3.3.1 The 2023 test at n_TOF

In 2023, a test was conducted using the EAR2 neutron beam at n_TOF to refine the design of the previously mentioned experimental setup. For this purpose, only a single plane of the 2D µ-RWELL and a scintillator bar array was employed, as illustrated in Figure 3.8.

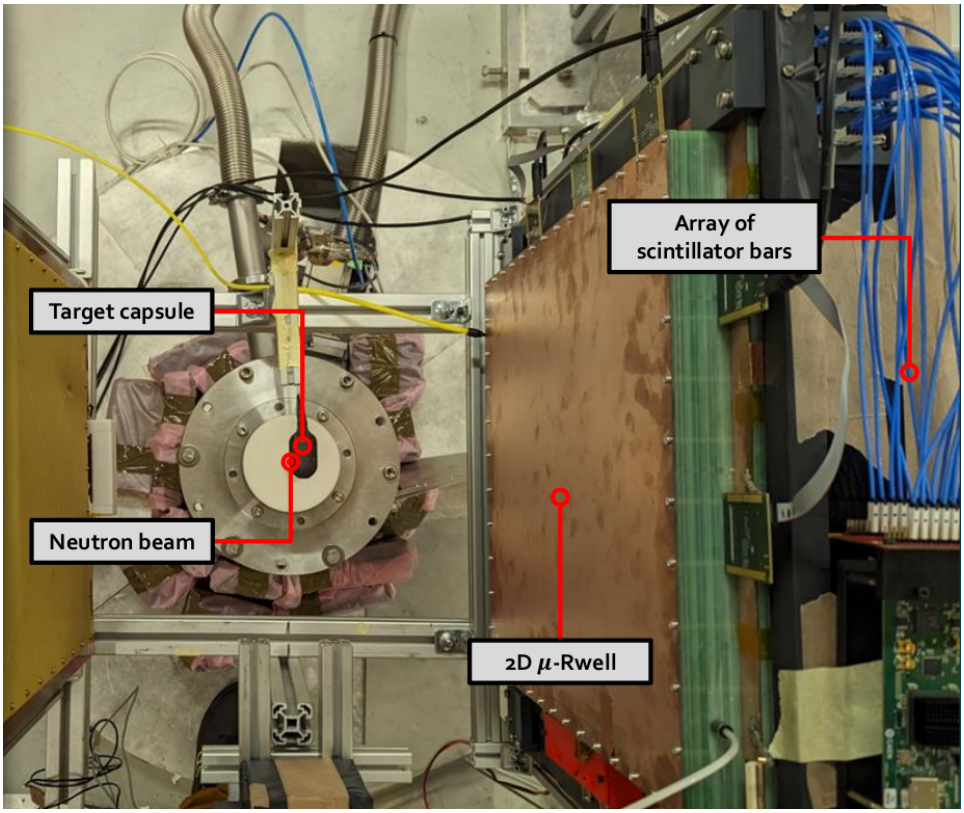

Figure 3.8: Photo of the experimental setup during the 2023 test at EAR2.

The test was performed using an empty target capsule, originally designed to contain ^{3}He. The purpose was to evaluate noise and saturation effects based on the following factors:

- Varying thicknesses of the empty target capsule.
- Distance between the detectors and the beam.
- Time after the γ-flash when the detectors become operational.

The data from this test have been analysed, specifically for the scintillator bar array. The results are described in Chapter 4.

3.3.2 He target

The target for the studied reaction is ^{3}He, a noble gas, and it can only be realized in gaseous or liquid form. The liquid form would allow for maximum density, but given its liquefaction temperature of 3.2 K, the cryogenic system required to keep the gas liquid would be expensive and introduce significant material into and around the beam, creating a high source of background that would make the measurement unfeasible.

The ^{3}He target must also meet the following requirements:

- It must have a high ^{3}He content to achieve a sufficiently high number of X17 counts within a reasonable beam time.
- The dimensions of the target must be compatible with the beam size (3 cm in diameter), which limits its width. Estimates show that using a volume of 15 cm^3 (with container dimensions approximately 25 mm $\times$ 40 mm), and a density of 59 g/L, the expected number of X17 counts can reach 100 counts/day.
- As the target is gaseous, the container must strike the best compromise between high mechanical strength and reduced mass to minimize scattering of the produced pairs and reduce the background from direct interactions with the neutron beam.

The effect of multiple scattering of the pairs associated with the container and the ^{3}He target has been evaluated via Monte Carlo GEANT4 simulations. As expected, thin materials with low atomic number are needed to minimize the deterioration of the signal-to-noise ratio caused by multiple scattering. The best choice is to use carbon fiber for the target casing due to its unique mechanical properties and minimal interaction with scattered neutrons, thanks to the low cross-section of neutrons on ^{12}C.
Several studies have been conducted to determine the best compromise between mechanical behavior and the container's impact on the experiment. The best results have been achieved with a spherical geometry, using an internal layer of 0.2-0.5 mm thickness of an aluminum alloy and carbon fiber as structural material. The internal layer aims to prevent helium diffusion and leakage, while the carbon fiber provides structural support to withstand the 358 bar ^{3}He pressure.
Most of the data at the n_TOF test were recorded using the thinnest target capsule, made of 0.3 mm aluminum and 2 mm carbon fiber. Other target capsule versions employed 0.5 mm aluminum or reinforced domes.

3.3.3 μ-RWELL tracker

The use of orthogonal strips in a μ-RWELL allows for 2D reconstruction of the particle's crossing point. By using a cathode positioned a few cm away from the multiplication plane, the detector can be operated in TPC (Time Projection Chamber) mode, which enables 3D track reconstruction. This can be achieved with strip timing measurement and highly segmented read-out electrodes: the first two coordinates are obtained from the position of the fired strips, while the third coordinate (perpendicular to the strip plane) can be computed using the electron drift velocity and the related time information [73]. The high density of the wells (and the low multiplication gain of these detectors) allows counting rates up to 10^5-10^6 Hz/cm^2 without significant saturation effects. Furthermore, the active part of the detector has a low density, composed of gas at atmospheric pressure

and a cathode made from lightweight materials. This characteristic gives the μ-RWELL reduced sensitivity to gamma rays and neutrons, making it ideal for use at n_TOF.
In the prototypes produced, the readout system integrated into the detector consists of orthogonal strips with a pitch of 1.2 mm. The gas mixture mainly used is $Ar + CO_2 = 70 + 30\%$ or $Ar + CO_2 + CF_4 = 45 + 15 + 40\%$. Operating these chambers with a cathode voltage of 3 kV/cm, given a maximum drift path of 30 mm (which is the distance gap between the cathode and the wells), the maximum drift time is 428 ns and 300 ns, respectively. This value is compatible with the 675 ns time window of the associated electronics. Finally, for both mixtures, the drift velocity remains substantially unchanged in the presence of a magnetic field.
The readout electronics of the μ-RWELL is based on the APV25 chip connected to the RD51/SRS ADC system. A single APV25 chip can read up to 128 channels; each APV25 channel consists of a preamplifier, a shaper, and an analog sampler that can operate up to 40 MHz (with a period of 25 ns, determined by an external clock) and can be stored in a circular analog FIFO with 192 samples, for a maximum sampling depth of $25 \times 192 = 4800$ ns. However, using the most common firmware at CERN, only $25 \times 27 = 675$ ns can be stored. Upon a trigger, the 128 channels are acquired simultaneously. The APV25 is mounted on a front-end board connected to the μ-RWELL readout system via a high-density connector. The front-end board receives and transmits signals to the SRS-ADC board. Two APV boards can be connected in a master-slave configuration to use the same HDMI cable. The ADC can convert up to 16 APV and is connected and controlled by an FPGA board (SRS-FEC).

3.3.4 Scintillator bar array

As shown in Figure 3.7, behind each μ-RWELL there is a plane with plastic scintillator bars, SCIONIX EJ-212 [74], measuring 3 mm × 20 mm × 500 mm.
As previously mentioned, the main function of these planes is to provide the trigger and time of flight of interacting neutrons, from which their energy is deduced. Additionally, during the analysis it is required that for a signal the hit bars match the position of the tracks from the μ-RWELL, improving the signal to noise ratio and the spatial resolution. In the test conducted at n_TOF, whose data are analysed in Chapter 4, bars of 3 mm × 17 mm × 500 mm were used, coupled with Silicon Photomultiplier (SiPM) arrays S13363-3050NE-16 [75].
Some properties of the chosen scintillator material and SiPM are reported in Table 3.2 and Table 3.3, respectively.

Properties	**EJ-212**
Light Output (% Anthracene)	65
Scintillation Efficiency (photons/1 MeV e^-)	1×10^4
Wavelength of Maximum Emission (nm)	423
Light Attenuation Length (cm)	250
Rise Time (ns)	0.9
Decay Time (ns)	2.4
Pulse Width, FWHM (ns)	2.7
Density (g/cm^3)	1.023
Polymer Base	Polyvinyltoluene
Refractive Index	1.58

Table 3.2: Properties of EJ-212 scintillator [74].

Properties	**S13363-3050NE-16**
Number of channels	16
Effective photosensitive area/channel (mm)	3×3
Pixel pitch (µm)	50
Number of pixels per channel	3584
Fill factor (%)	74
Refractive index of window material	1.55
Spectral response range (nm)	320 to 900
Maximum photon detection efficiency (%)	40
Breakdown voltage (V)	53 ± 5
Maximum dark count rate (Mcps)	1.5
Gain	1.7×10^6

Table 3.3: Properties of the Silicon Photomultiplier (SiPM) array S13363-3050NE-16 [75]. The reported photon detection efficiency does not include crosstalk and afterpulses.

The scintillator bar array was arranged in a crossed configuration, consisting of six bars in each orientation. Each SiPM array, composed of 16 SiPMs with dimensions of 3 mm × 3 mm, was coupled to three adjacent bars. To cover both ends of the 12 scintillating bars, a total of eight SiPM arrays were used.

A photograph of the scintillator bar array tested at n_TOF and analyzed is shown in Figure 3.9.

Figure 3.9: Picture of the scintillator bar array tested at n_TOF-EAR2 in 2023.

Light collection in the scintillators is enhanced by a reflective layer, less than 1 µm thick, deposited by evaporation and protected by a polymer coating. This layer ensures over 95% reflectivity across all wavelengths. Additionally, a layer of Teflon tape on the outside shields the scintillators from ambient light.
The light signals are collected in the SiPMs and transmitted to a front-end board, which combines the signals from 4 adjacent SiPMs into a single analog output. This results in 4 analog outputs per array and a total of 32 outputs for the entire system. For the n_TOF test, the electronics were handled by a CAEN FERS A5202 module [76]. It is composed of 64 channels, corresponding to 2 Citiroc-1A chips. The Citiroc-1A preamplifiers ensure a dynamic range from 160 fC to 400 pC (i.e. from 1 to 2500 photo-electrons with 10^6 SiPM gain). The module features a programmable 10-bit DAC for setting a common threshold (minimum 1/3 photo-electron), a separate trigger line for each channel, and a programmable 4-bit DAC for fine-tuning the threshold on a per-channel basis. As described in the next chapter, three acquisition modes are possible: "counting," "spectroscopy," or "timing".
The choice of readout and data acquisition systems was influenced by the limited availability of acquisition channels in the n_TOF DAQ (equipped with digitizers operating at a 1 GHz sampling rate) and by the need to assess the potential use of the FERS in the final setup.

Chapter 4

First experimental results

As described in the previous chapter, the design of the detection system for the search for the X17 anomaly at n_TOF was guided by both theoretical and experimental considerations. This chapter presents the results of the 2023 test data analysis on the scintillator bar array, which provided information that helped the research group make key decisions about the final design of the detection system (outlined in Section 4.7). As mentioned before, the test was performed using the empty target capsule, that will contain ^{3}He in the future measurement, with a 2D µ-RWELL and the scintillator bar array as detection system.

4.1 Data structure

The DAQ system used in the test can be operated in three distinct acquisition modes: "counting," "spectroscopy," or "timing" [76]. The chosen data acquisition configuration for the scintillator bar array, described in Section 3.3.4, does not provide amplitude information when operating in timing mode. In this mode, the system records Time-over-Threshold (ToT), that measures the duration for which a signal remains above a set amplitude threshold, and Time-of-Arrival (ToA), corresponding to the moment the signal is detected. The timing data are provided with a 0.5 ns resolution. While the ToT data could, in principle, offer an estimate of the signal amplitude, this requires proper calibration and knowledge of the signal shape, which could not be performed in this experimental setup. Nevertheless, valuable insights can still be extracted from the ToT data, as discussed later.
The acquisition trigger is provided by a reference detector, commonly used at n_TOF, which consists of a cubic plastic scintillator read by photomultipliers. As soon as the characteristic γ-flash signal is detected, the trigger signal is sent to both the µ-RWELL and scintillator array DAQ systems, with an adjustable delay. During data collection, this delay was set to different values ranging from 0 ns to 10 µs. For each trigger, up to

64 signals can be acquired by the scintillator DAQ system. A typical data file contains approximately 3×10^3 triggers, thus corresponding to around 3×10^3 neutron bunches. Despite the limitations mentioned above, the data collected during the 2023 test still provide valuable information regarding the use of SiPMs combined with scintillator bars. As noted previously, the scintillator bars were arranged in a crossed configuration, composed of 6 vertical and 6 horizontal bars. SiPM arrays were placed at the ends of the bars, with a total of 8 channels on each side. The channels and their labels are shown in Figure 4.1. Channel 29, located at the top right, was disconnected due to a faulty SiPM pixel detected during data collection. Consequently, the analysis considers a total of 31 channels.

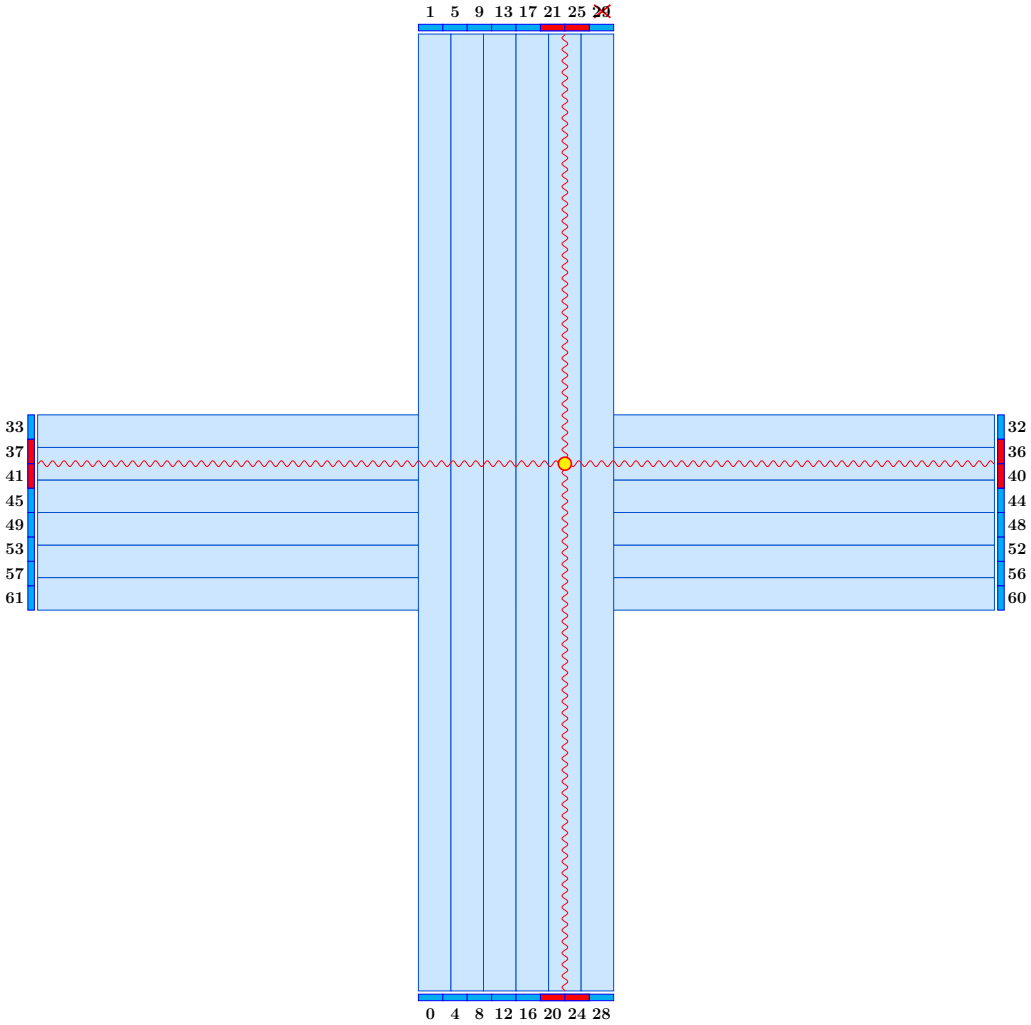

Figure 4.1: Schematic representation of the scintillator bar array, showing the FERS channel labels and an example of a signal-like event. Channel 29 is marked with a cross to indicate that it is disconnected.

4.2 Background and threshold estimation

In order to minimize background, some data were collected in "pedestal" mode, i.e. sending triggers to the detection system when the EAR2 neutron beam was off. In this way, the registered Time-over-Threshold (ToT) data helps in setting a threshold value to discriminate between real signals and background signals. Since ToT is related to the signal amplitude, data with very low ToT are likely to be noise and can be discarded at the initial stages of analysis.

The result of this analysis is illustrated in Figure 4.2. In many cases, the detection threshold was probably above the background level. As a result, 21 out of the 31 channels did not acquire sufficient data to perform a reliable background estimation. For the remaining channels, where enough data were available, the ToT threshold was determined statistically. In particular, it was set to the average value of the first main peak (shown by the continuous line in Figure 4.2), plus three times its standard deviation.

For channels with insufficient data to compute the ToT threshold statistically, this was set to a conservative default value of 24 ns, slightly above the highest threshold calculated from the available data, which was approximately 22 ns.

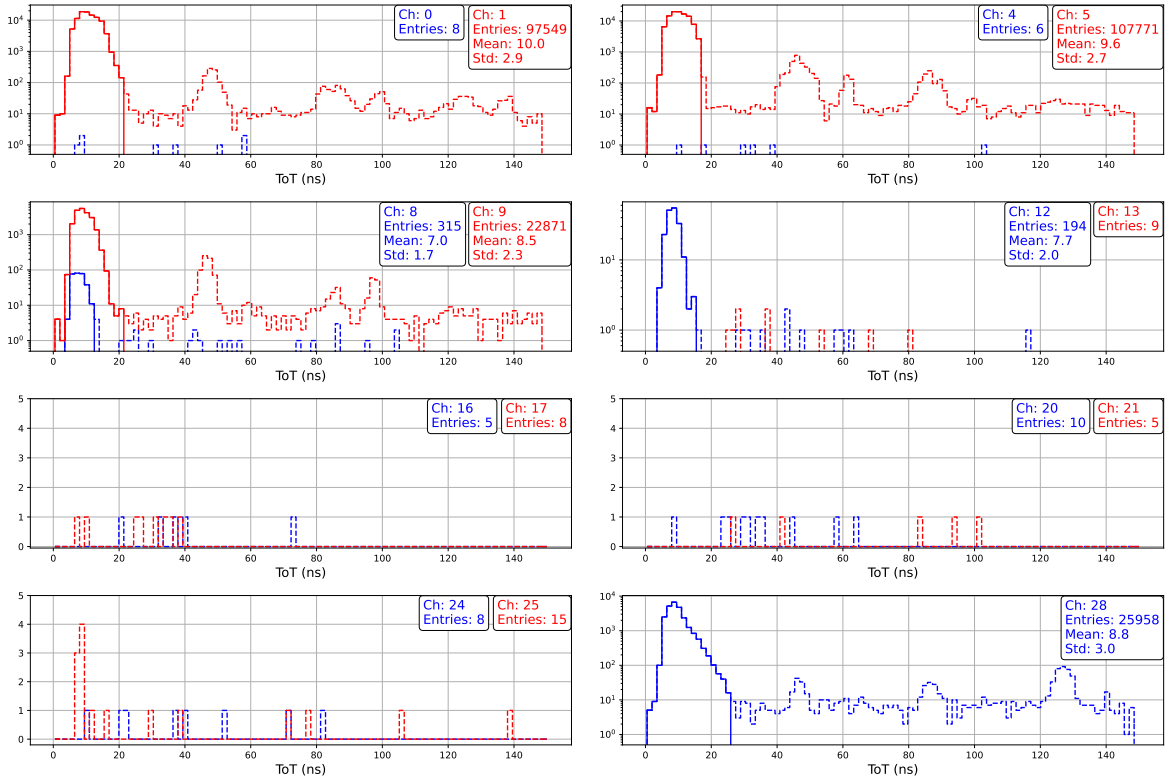

(a)

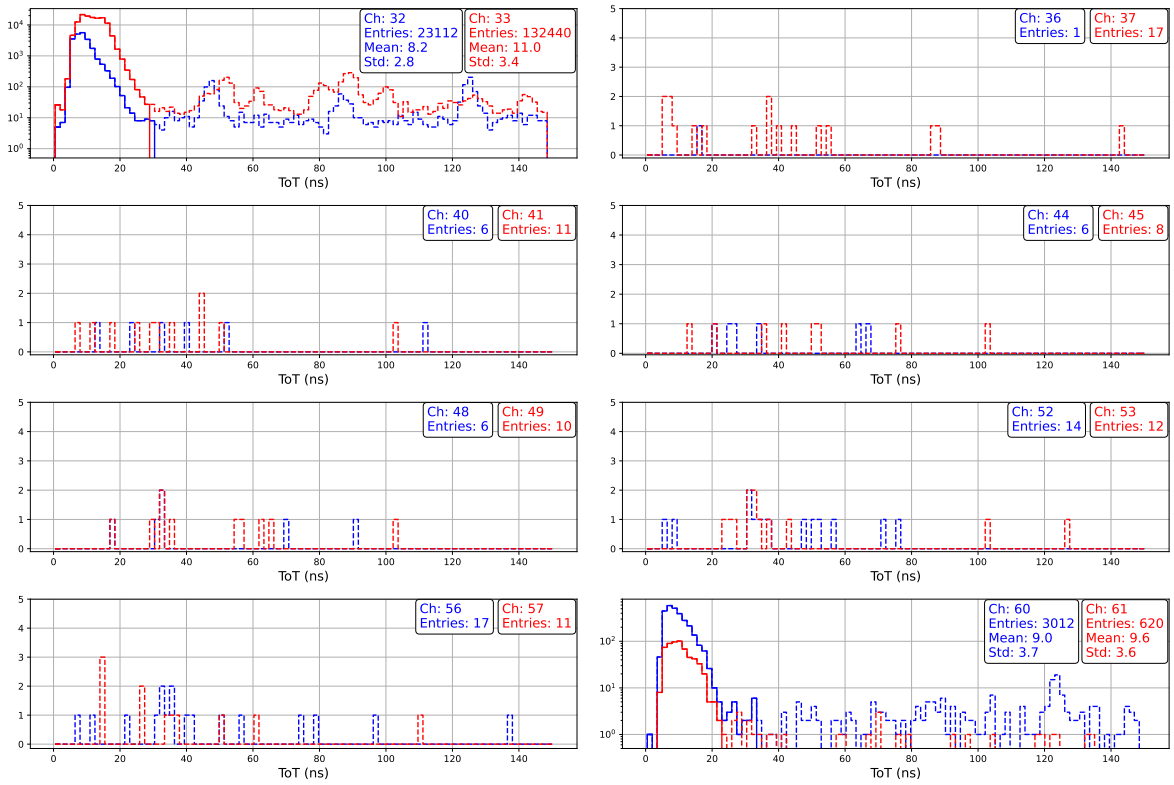

(b)

Figure 4.2: Time-over-Threshold data registered for vertical (a) and horizontal (b) channels from "pedestal" measurements. The distributions are grouped by channels at opposite ends of the scintillating bar array. The data plotted with continuous lines, corresponding to the first main ToT peak, are the ones used for the threshold estimation, while dashed lines indicate the ones not used. Channel labels and entries, together with mean and standard deviations computed when sufficient entries where available, are reported.

The background registered can be attributed to several factors, such as residual activated material in the experimental hall and the capsule target, and electronic noise. The data in Figure 4.2 are grouped by channels situated at opposite ends of the scintillating bar array. In this way, particularly noisy channels and/or scintillating bars can be already flagged for the further steps of the analysis, e.g. during the hit map reconstruction process.

The ToT threshold value chosen from the pedestals has been selected to avoid distorting the average ToT with too high values. This cut still contains the important contribution of the background: this can be clearly seen in Figure 4.3, where the ToT data from all signal runs has been compared to the cut on the pedestal used for threshold estimation. From this plot it can also be seen that a very relevant part of the data is constituted by low ToT background signal, which highlights the need for the threshold estimation. For all experimental conditions (such as delay from γ-flash and target capsule thickness) this selection cuts 20 % to 30 % of recorded events.

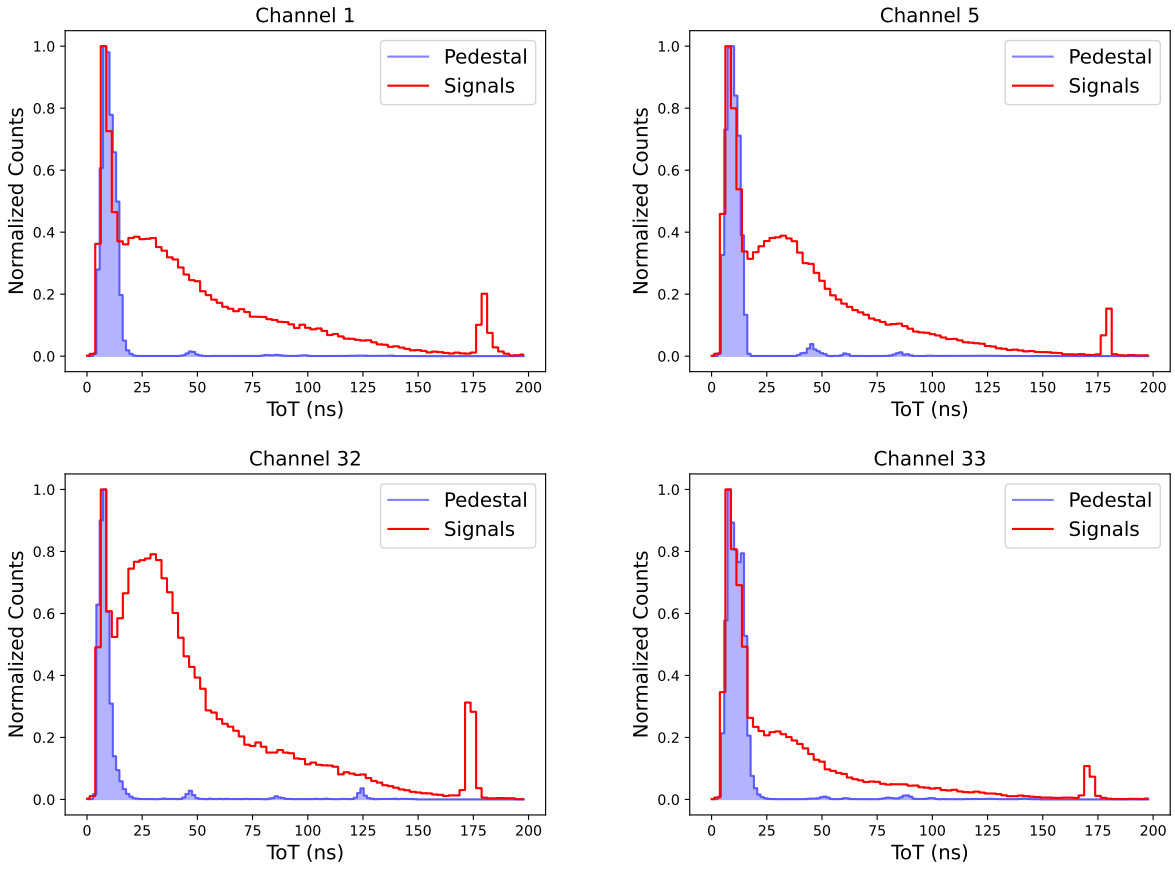

Figure 4.3: Comparison of Time-over-Threshold data between signal runs (red solid lines) and pedestal runs (blue filled lines), for some relevant channels (two per bar orientation). Data have been normalized to match the maxima of the distributions. The background peak at low ToT can be clearly distinguished from the signal component, and overlaps well with the peak of the pedestal signals, confirming the correctness of the cut. The small peaks visible at ToT ≈ 175 ns are signals attributed to the γ-flash.

The ToT signals of channels for which the pedestal data were not enough for a threshold estimation still display a peak at low ToT values, even if less prominent. The ToT distributions for some of the channels that exhibit this behaviour are reported in Figure 4.4. The conservative ToT threshold cut value excludes potential background noise, without compromising the quality of the analysis.

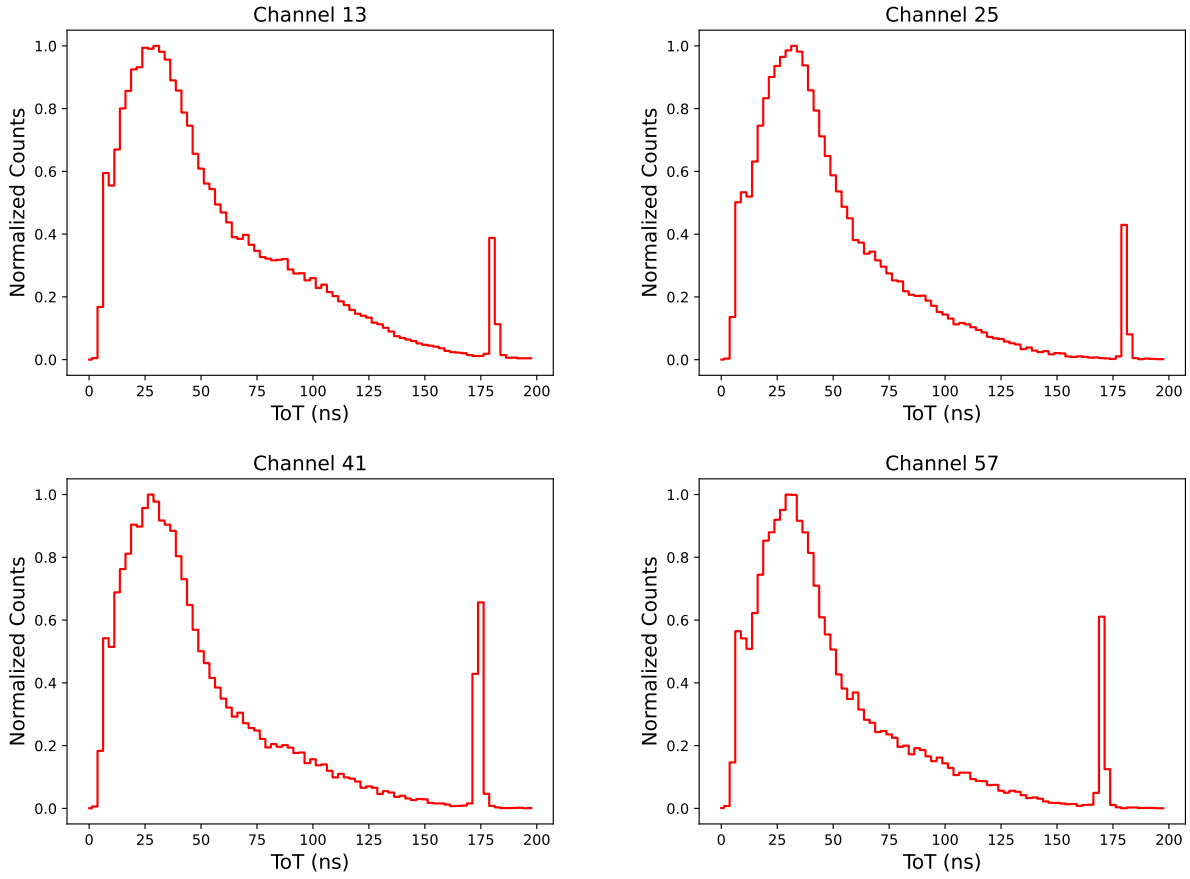

Figure 4.4: Time-over-Threshold data from signal runs for channels where the ToT threshold was set to the default value of 24 ns. The data have been normalized to the maxima of the distributions. While a background peak at low ToT is still present, its prominence is reduced compared to the signal component. The peaks visible at ToT ≈ 175 ns are signals attributed to the γ-flash.

4.3 Dead time estimation

An important aspect to be verified for the detection system is whether the time performances are suitable for the expected event rate. In fact, while light signals in scintillators are generally produced and propagated in a short time, the SiPM signal pulses are slower, lasting up to hundreds of nanoseconds, and could therefore hinder the detector timing performances. For this reason, it is useful to estimate the dead time of a channel. To do this, the time difference Δt between consecutive hits in a high event rate environment such as the γ-flash detection can be measured. In this situation, the dead time of a channel is expected to correspond to the minimum Δt obtained.
As shown in Figure 4.5, which displays the distribution of ToT signals as a function of the time interval between two consecutive events recorded in the same SiPM (the figure shows a representative SiPM for all SiPMs), this behaviour is confirmed: the time difference between consecutive events is always greater than the corresponding ToT of the first event. Since for some events ToT values coincide with the corresponding Δt, it can also be stated that the channels are ready to detect new events as soon as the previous signal goes below the amplitude threshold, without any particular additional delays.
In particular, the significant reduction in the number of signals in the region $\Delta t < 100$ ns indicates a dead time of the acquisition system of the same magnitude. This decrease in the number of signals for Δt <100 ns also indicates the existence of possible pileup events.
This systematic effect could be mitigated by using the n_TOF acquisition system (consisting of flash ADC with 1 GHz sampling rate), which allows for the reconstruction of signals separated by just a few tens of nanoseconds using appropriate offline filters and reconstruction algorithms, resulting in a dead time of less than 10 ns.
More information can be extracted from the plots as Figure 4.5. For example, the signals due to the gamma flash are easily recognizable, as they all have the same ToT of 175 ns. This becomes even more evident when comparing this figure with delayed acquisition data such as Figure 4.6, in which the acquisition was delayed of 500 ns, i.e. events recorded from 500 ns after the γ-flash. Figure 4.7 shows the registered signal in a much lower event rate environment, where the delay from the γ-flash was 10 µs. While the general increasing trend at low Δt is still present (confirming that the dead time estimation is independent on the γ-flash presence), the 175 ns ToT population is absent. Lastly, it can be noted that no events are present below a specific ToT value, giving a precise indication of the threshold chosen for the selection of ToT events (described in Section 4.2).

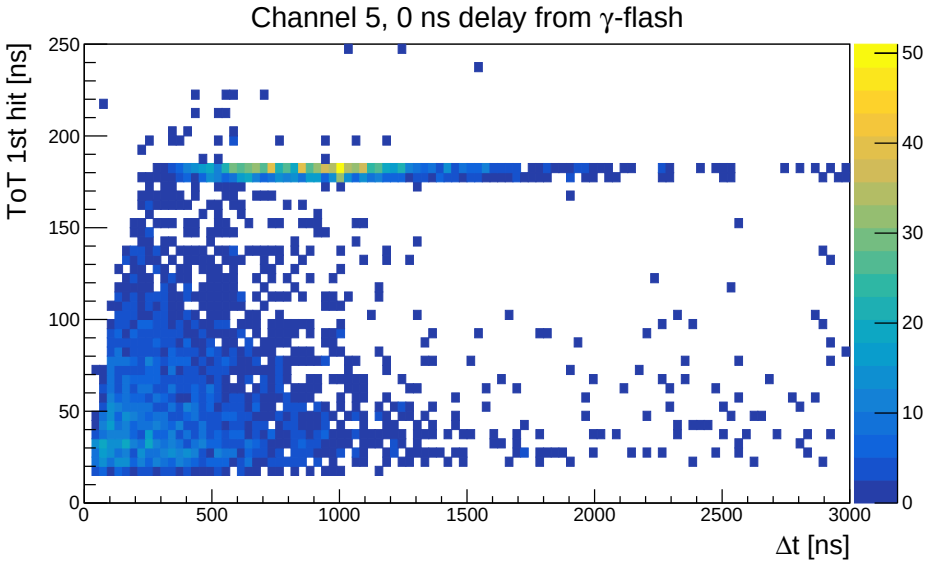

Figure 4.5: Time-over-Threshold as a function of the time difference of consecutive events in the same channel. The group of signals due to the γ-flash is evident, at a ToT value of approximately 175 ns.

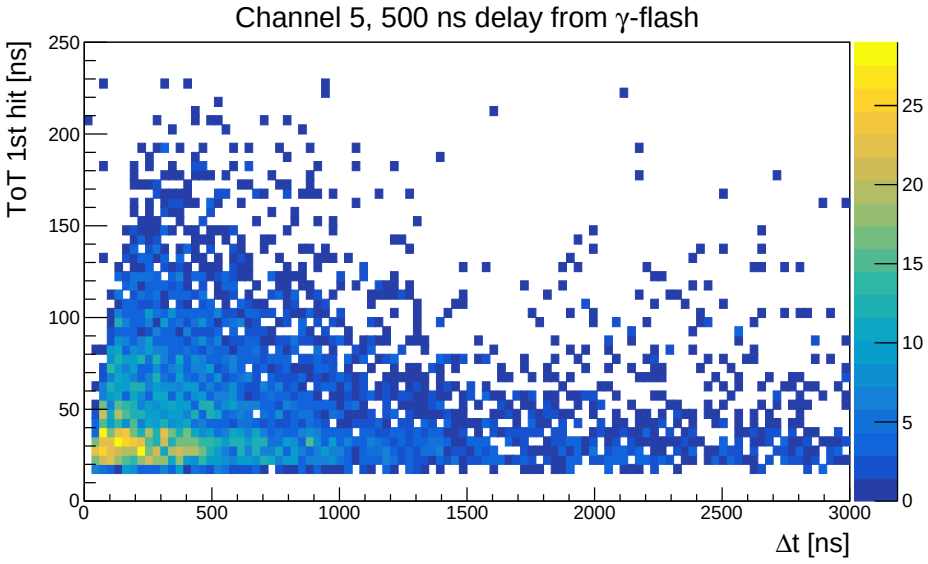

Figure 4.6: Time-over-Threshold as a function of the time difference with the consecutive event in the same channel. The typical γ-flash ToT signal is not visible, since data were acquired with a 500 ns delay.

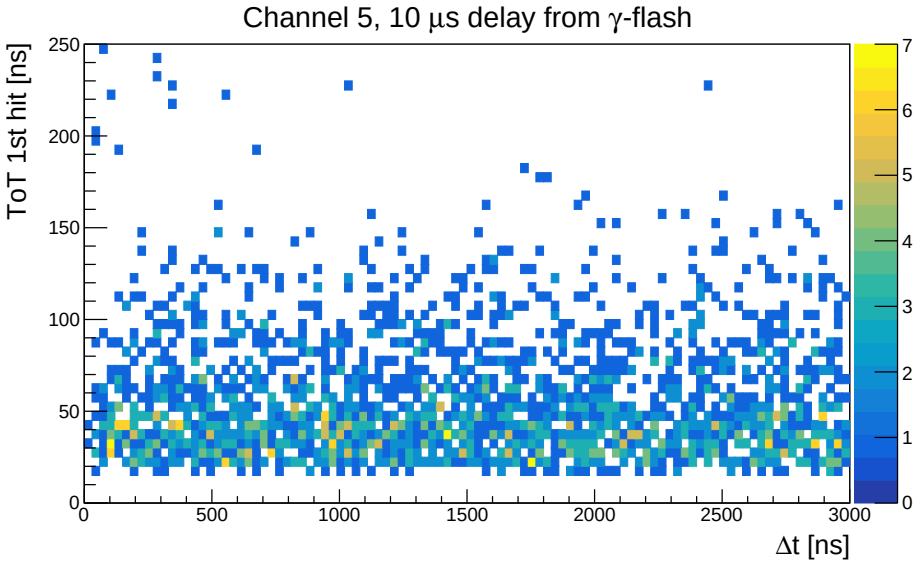

Figure 4.7: Time-over-Threshold as a function of the time difference with the consecutive event in the same channel. The event rate is low, since data were acquired with a 10 µs delay from the γ-flash.

4.4 Time window estimation

Data that can be attributed to "true" signals, called "coincidences" from now on, are light signals registered by at least 2 SiPMs at opposite ends of a scintillating bar. These coincidences must happen within a certain time window Δt_c in order to attribute the signal from two channels as coming from the same event.
At first, a simple naive estimation could be done considering the propagation of the scintillation light along the bar, for which $\Delta t_c \approx L/c_n$, where L is the scintillating bar length (500 mm) and $c_n = c/n$ the speed of light divided by the refraction index of the scintillator (see Table 3.2). However, to account for the collection of light by the SiPM (which could be internally reflected and reach the end of the bar later), the transmission to the electronics and other possible delays, a broader time window must be selected, at the cost of increasing false coincidences.
The final choice was guided by considerations on the distribution of the time difference between two signals at opposite ends of the scintillating bars. As it can be seen in Figure 4.8, when detectors are exposed to the γ-flash, the coincidences decrease exponentially towards a flat background. For all other cases, i.e. for any time delay from the γ-flash, the distribution is less regular, but the majority of the events are still comprised within the first 10 ns. This can be seen clearly in Figure 4.9, where data have been acquired with the highest delay with respect to γ-flash, 10 µs, corresponding to low energy neutrons

(tenths of keV, as visible in Figure 2.1).
Taking into account all the aforementioned reasons, the coincidence time window Δt_c has been set to 10 ns. In this way all relevant coincidences are accepted, confirmed from the fact that the mean values of the distributions are always below this time window. Further requirements, described later, will improve the selection of true hit signals.

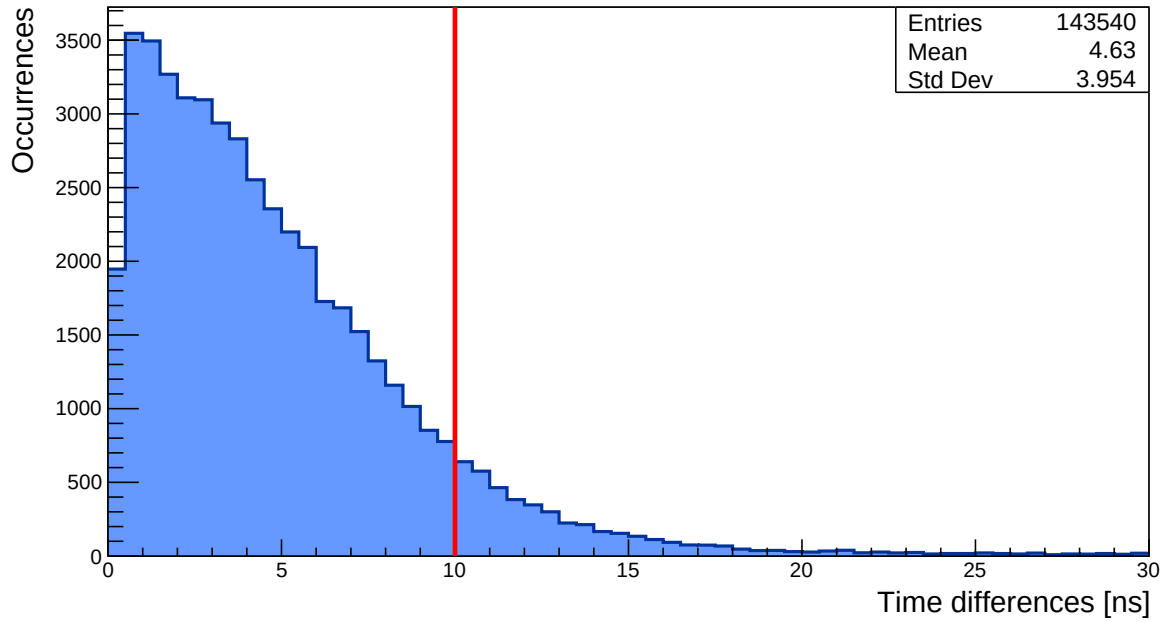

Figure 4.8: Distribution of time differences between signals that reached two opposite channels at the end of any scintillating bar within the same trigger event. Data have been acquired in presence of the γ-flash, which cause the majority of signals. The solid red line indicates the chosen time window $\Delta t_c = 10$ ns.

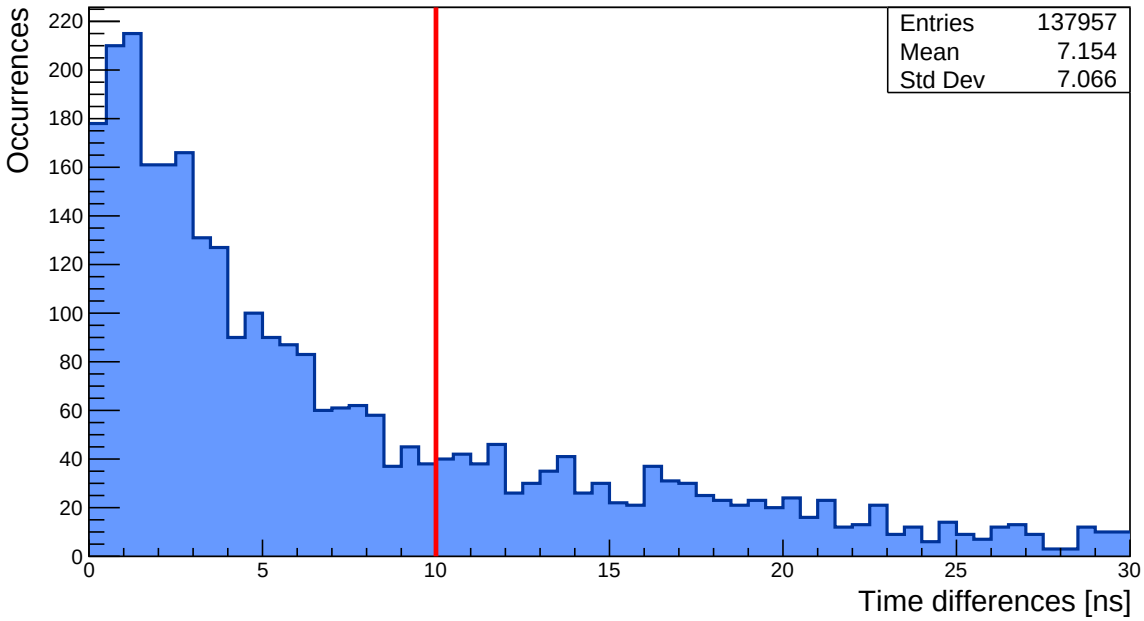

Figure 4.9: Distribution of time differences between signals that reached two opposite channels at the end of any scintillating bar within the same trigger event. Data have been acquired with a 10 µs delay from the γ-flash. The solid red line indicates the chosen time window $\Delta t_c = 10$ ns.

4.5 Hit map reconstruction

An important aspect of the analysis is to estimate with the best precision the hit position of signals in the scintillating bar array. This piece of information will be combined with the 2D µ-RWELL spatial information to achieve the tracking capabilities required for the detection system. To achieve this goal, several physical considerations must be done to select the events that can hinder the performances of the detector in the future data taking with the ^{3}He target.

4.5.1 Coincidence rate

As depicted in Figure 4.1, a light signal event could be potentially detected by eight different channels, four per scintillating bar, provided that the particle traverses the entire array and hence releases energy in both the vertical bars, which are closest to the target, and the horizontal ones.
It may also happen that two adjacent channels on the same side of a scintillating bar fire multiple times for the same signal. This could happen for several reasons, such as afterpulses and crosstalk effects, which are common in SiPM detectors. The incidence

of these processes, however, must be estimated with the available timing information, to assess if the contribution is negligible or not. In the latter case, the reconstruction software could introduce a systematic increase on hit counts for scintillating bars and channels particularly affected by these effects.
As stated before, the term "coincidence" refers to a signal registered from at least one channel per side of a scintillating bar within the chosen time windows Δt_c. In Figure 4.10 the number of coincidences per trigger is shown in presence of the γ-flash. On average around 22 coincidences are recorded within the same trigger event. Assuming that the 12 scintillating bar have uniform response, in most of the triggers each bar records 2 coincidences.
This behaviour is confirmed by looking at Figure 4.11, where the number of coincidences greater than 0 per bar per trigger is shown. However, a non-negligible number of times a single bar records 4 coincidences within the same trigger, while very rarely 5 are reached. This could be attributed to particularly photo-sensitive scintillating bars and/or SiPMs, that fire multiple times when exposed to the γ-flash.

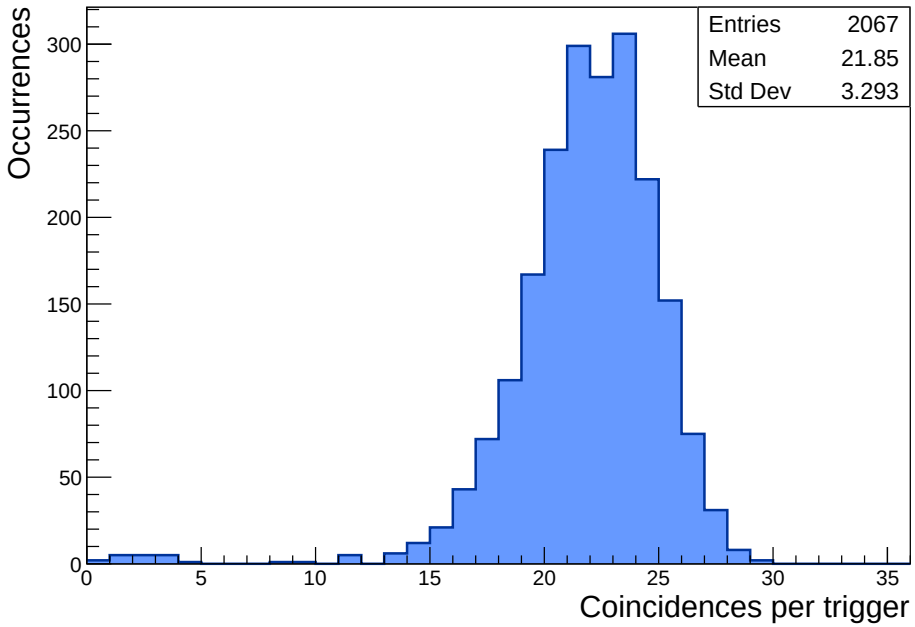

Figure 4.10: Distribution of coincidences recorded per trigger event in presence of the γ-flash.

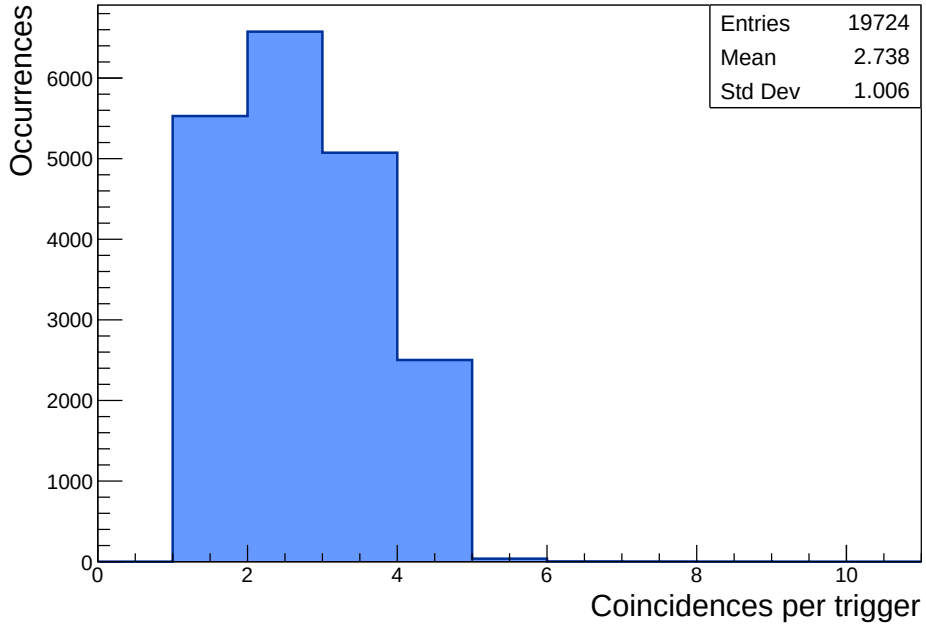

Figure 4.11: Distribution of coincidences recorded per bar per trigger event in presence of the γ-flash. The bin at 0 coincidences per trigger is not shown.

In low-rate environments, such as those following the end of the γ-flash, the scintillator array has demonstrated a suitable response to the observed event rate. In fact, as seen from Figure 4.12, the coincidences per trigger just 500 ns after the γ-flash are almost always zero, indicating a very low event rate with the chosen selection criteria. In this case we are interested in a low response of the scintillator array since the signals recorded in this test will be the physical background of the future measurement. Figure 4.13 shows the corresponding distribution of coincidences registered per trigger per scintillating bar. If there is more than one coincidence in a trigger event, each bar records usually not more than a single coincidence. However, also in the environment with no γ-flash, a non negligible amount of times some bars record two coincidences in the same trigger event, and sometimes up to 5. This hints that some scintillating bar may be more noisy than others, and must therefore be flagged during the analysis. In fact, it has been found that most of the times in which more than 3 coincidences are found, these are registered in the same scintillating bar, the one seen by channels 32, 33, 36, 37 (depicted in Figure 4.1).

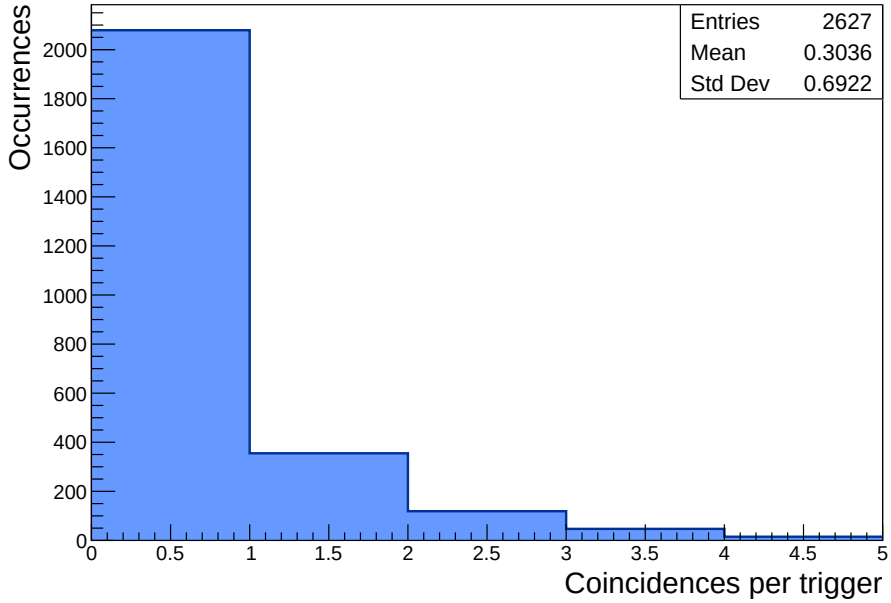

Figure 4.12: Distribution of coincidences recorded per trigger event. Data have been acquired with a 500 ns delay from the γ-flash.

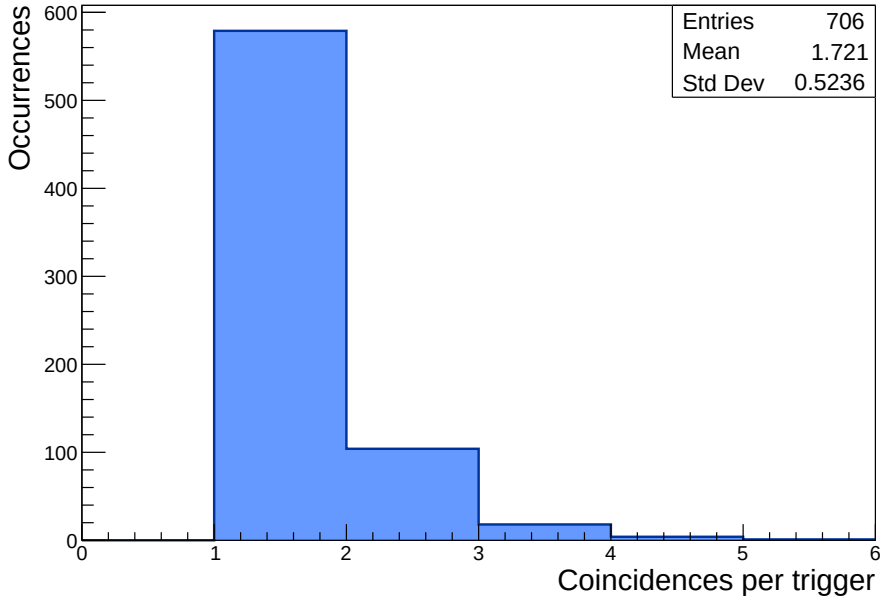

Figure 4.13: Distribution of coincidences recorded per trigger event per scintillating bar. Data have been acquired with a 500 ns delay from the γ-flash. The bin at 0 coincidences per trigger is not shown.

4.5.2 Channel reconstruction

After setting all necessary parameters previously described, a reconstruction algorithm was developed to assess the event rate registered by the channels, and identify particularly noisy channels and hotspots. A preliminary reconstruction can be done by considering only coincidences in which the light signals reach channels placed at exactly opposite ends. An example of this reconstruction algorithm can be seen in Figure 4.14. The coincidence gives a spatial information along only one direction, vertical or horizontal depending on the fired channels. Some observations can already be done with this reconstruction. It appears that the channels 32 and 33 (at $y \approx 40\,\text{mm}$) always register the highest number of coincidences and surprisingly, channels 36 and 37 (the ones just below 32 and 33, at $y \approx 40\,\text{mm}$) register no coincidences, up to a few in some runs. This effect is present also in the high signal rate environment of the γ-flash, as visible in Figure 4.15. This behaviour clearly suggests that crosstalk effects are particularly relevant for these channels, and poor coupling of channels 36 and 37 to the scintillating bars may have increased the disproportion between signals coming from the same scintillating bar and reaching these channels. It can also be observed that, due to the fact that channel 29 is disconnected, no coincidences are present for the couple 28-29 (at $x \approx 40\,\text{mm}$).

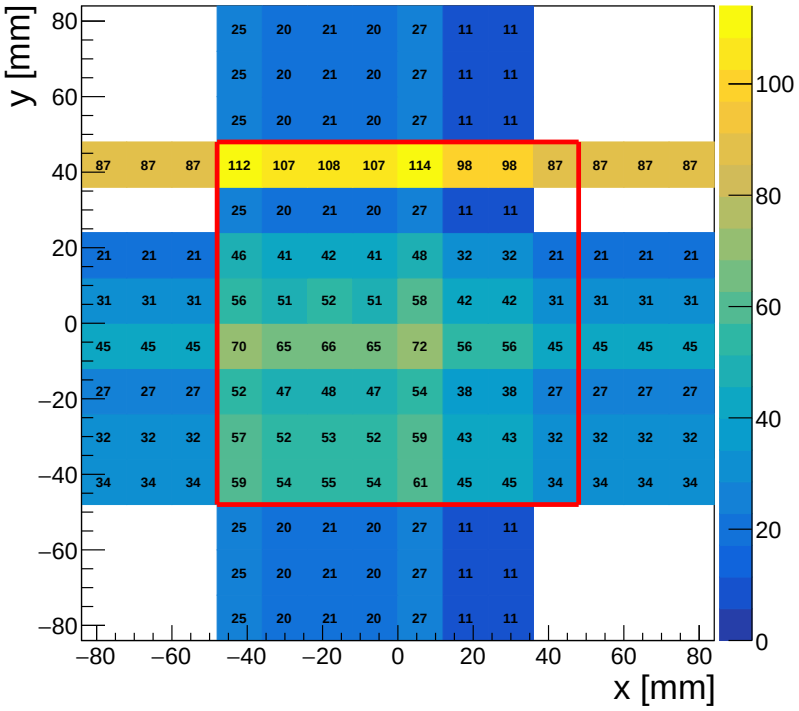

Figure 4.14: Hit map reconstruction on channels for signals with 500 ns delay from the γ-flash.

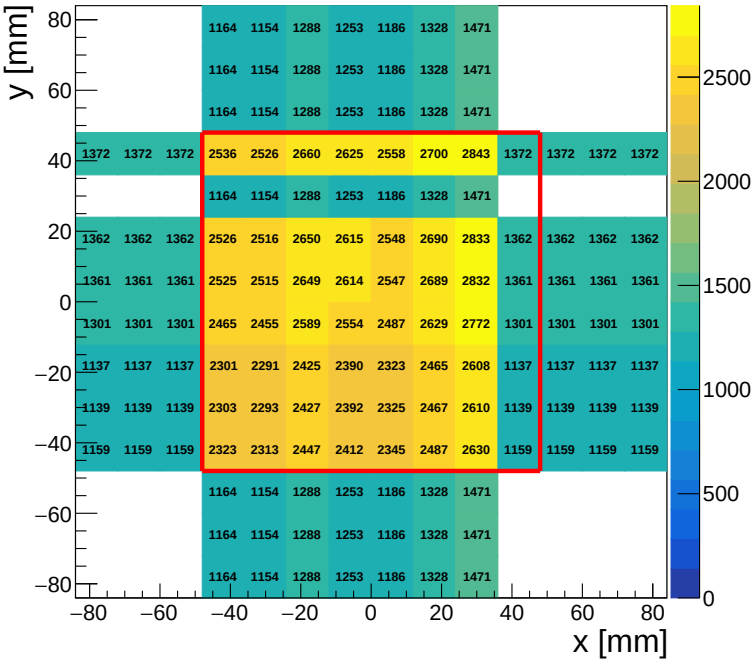

Figure 4.15: Hit map reconstruction on channels for signals with 0 ns delay from the γ-flash.

4.5.3 Bar reconstruction

The fact that a scintillating bar at each end is seen by more than one channel is due to the difference between the width of a scintillating bar and the width of four SiPM that constitute a channel. While this significantly complicates the reconstruction during the analysis, it helps in increasing the number of coincidences, since the light signal produced by a true event is probably detected by at least one channel per side. For this reason, a reconstruction algorithm was implemented to attribute signal events to the scintillating bars by requiring that at least one channel is in coincidence with another that sees the same bar on the opposite side. Examples of these results are reported in Figure 4.16 and Figure 4.17, after and during the γ-flash, respectively.
This reconstruction addresses the previous issues regarding coincidences between channels at exactly opposite ends. The results are substantially different: the response of the array is more uniform compared to Figure 4.14 and Figure 4.15, with a higher concentration of events observed not only at $y \approx 40$ mm, but also at $y \approx -30$ mm. It is interesting to note that the peak of coincidences is registered at $y \approx -30$ mm even in the presence of the γ-flash. This suggests that certain non-negligible physical background phenomena do not reach the detectors uniformly, like in the case of elastically scattered neutrons. Alternatively, it could indicate a different impact of the γ-flash to the readout channels.

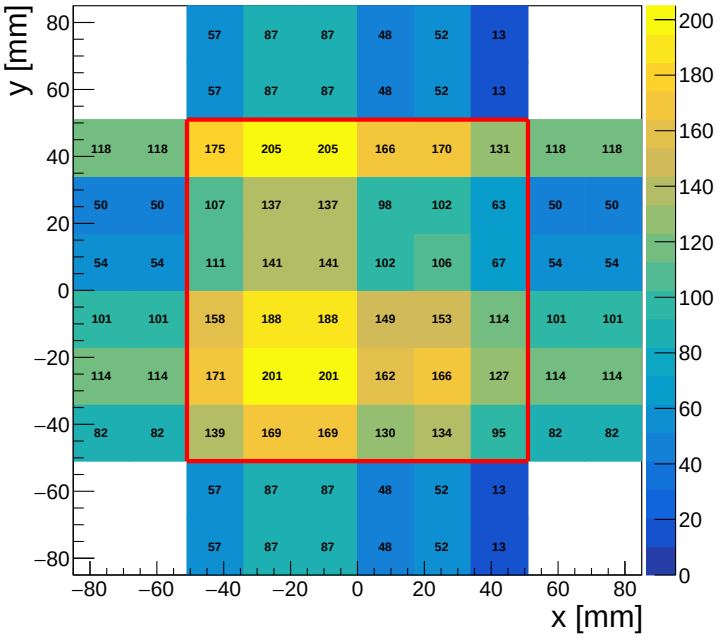

Figure 4.16: Hit map reconstruction on scintillating bars for signals with 500 ns delay from the γ-flash.

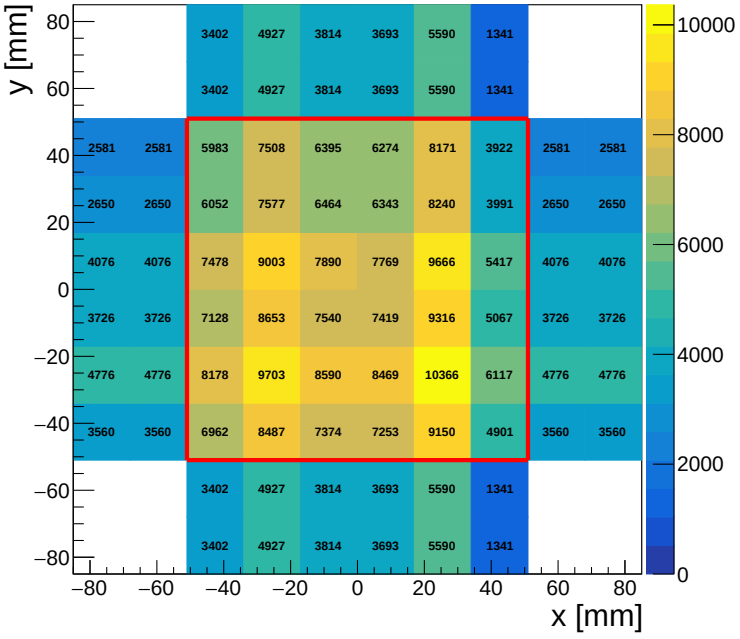

Figure 4.17: Hit map reconstruction on scintillating bars for signals with 0 ns delay from the γ-flash.

4.5.4 Crossed coincidences

The reconstruction analysis up to this point has considered coincidences between single pairs of channels or single bars. However, an additional event selection can be performed by considering coincidences within a chosen time window Δt_x between a vertical and a horizontal bar, called "crossed coincidences". The results of this additional selection criterion are shown in Figure 4.18 and Figure 4.19 for $\Delta t_x = 10\,\text{ns}$.
While in the γ-flash environment the number of crossed coincidences is high, as expected due to the high signal rate, this number drops just after 500 ns, and remains at the same low order of magnitude at much later times. This behaviour can be explained by the fact that usually only a single coincidence in a bar is recorded per trigger, as discussed in Section 4.5.1. When more than one coincidence in a bar is registered, it is often associated with noise from the top horizontal bar. The additional requirement of two bars with opposite orientations firing within a chosen time window Δt_x, further reduces the number of signal-like events. The time window can be set arbitrarily large without significant increase of this number.

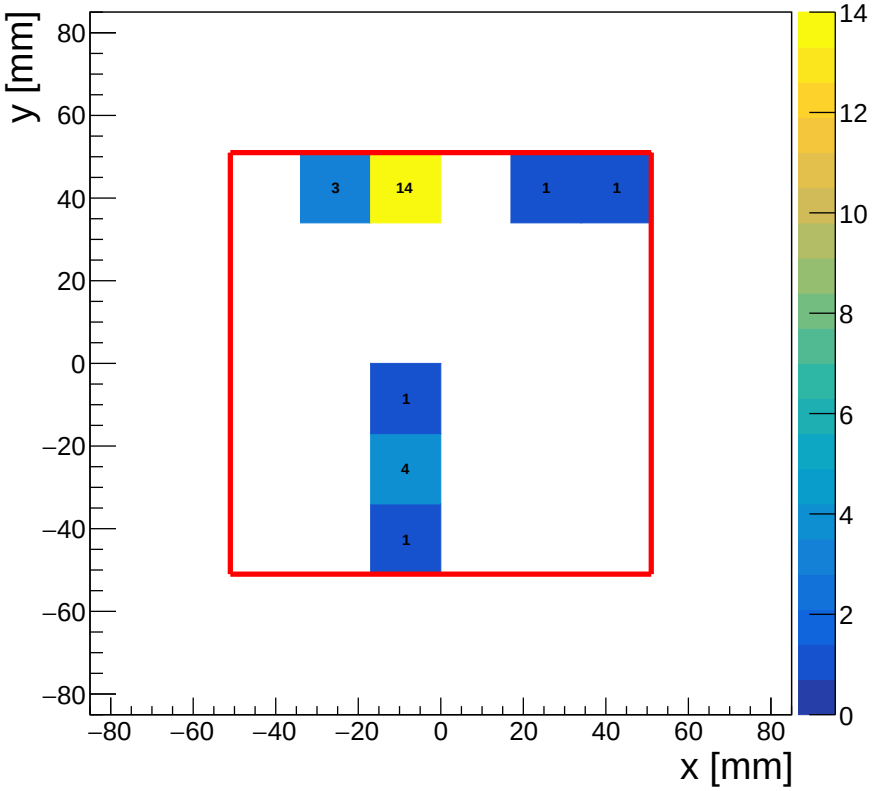

Figure 4.18: Hit map reconstruction of crossed coincidences for signals with 500 ns delay from the γ-flash.

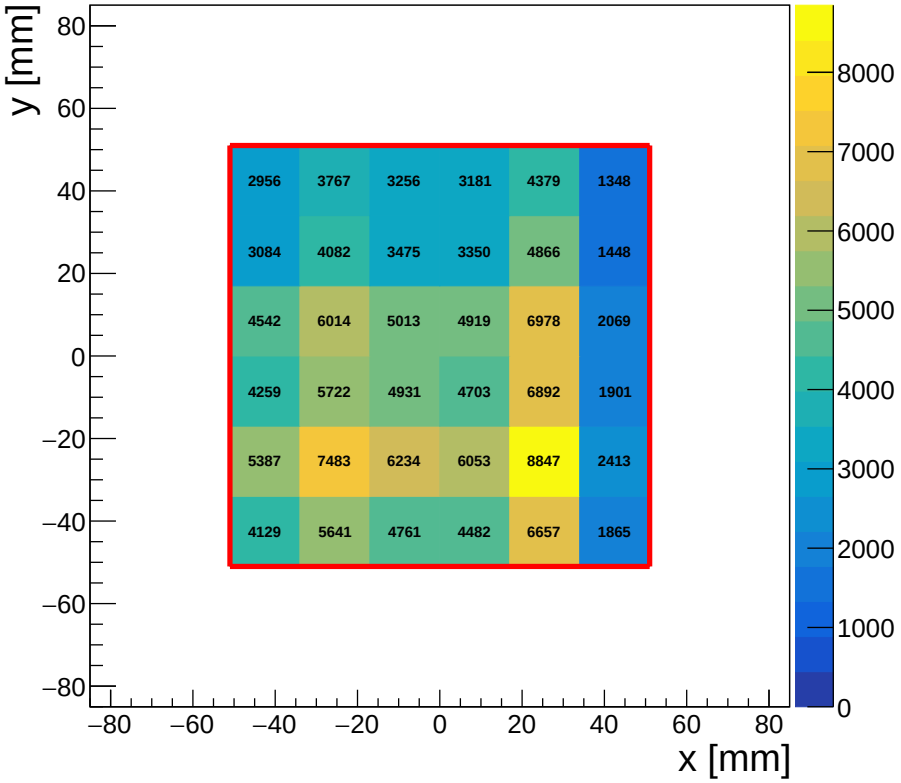

Figure 4.19: Hit map reconstruction of crossed coincidences for signals with 0 ns delay from the γ-flash.

4.5.5 ToA information

The hit map reconstruction so far did not provide spatial information of the hit position along a scintillating bar, 500 mm long. In the case of crossed coincidences, the signals are comprised within the spatial superposition of the two scintillating bars, which correspond to a squared area of 17 mm $\times$ 17 mm. This is not enough to provide useful tracking information alone, but in coincidence with the 2D µ-RWELL it will help in the event selection and track reconstruction, by matching tracks in the chambers with the hit points in the scintillator array.
The hit positions can be better reconstructed by using the available timing information for the signals, ToA and ToT. While the latter will require further analysis, after a thorough calibration and characterization of signal amplitudes, the Time-of-Arrival can help identify the hit position of a signal along a bar.

Given the 0.5 ns timing resolution and the time traversed by a light signal from the end of a bar to the other, $\Delta t_c \approx L/c_n \approx 2.5\,\text{ns}$, the bar can be roughly divided in 5 sections of 100 mm each, where the central one corresponds to the area in which the two scintillator array layers overlap. As previously mentioned, the chosen time window for a coincidence is 4 times larger, $\Delta t_c = 10\,\text{ns}$. This does not imply an increase of spatial resolution, since the greater value accounts for fluctuations of the time signal that do not necessarily happen regularly inside the bar. For this reason, the different values of ToA will still give a spatial resolution of 100 mm.

However, as stated before, the use of this piece of information cannot be trusted unless a proper calibration of the scintillating bars is performed. The contribution to the delay of multiple reflection of light along the bar, defects that make the light propagation asymmetric along the bar and electronics delays must be established to apply the right corrections to this algorithm. At the time of this analysis, this characterization was not available yet, so in the current implementation of the algorithm there is the assumption that the scintillation light is delayed uniformly along the length of the bar. This is not true if, for example, there are asymmetric delays due to defects or bad couplings of channels to the bars (which are probably present, as seen from the pedestal data in Section 4.2).

More than improving the spatial resolution, this reconstruction will allow to check whether the majority of signals was registered in the crossing of the scintillating bars, or a significant number of events is recorded outside of it. If this is the case, the final setup will require a larger acceptance, either by increasing the number of bars or by decreasing the distance from the target. An example of hit map reconstructed with this method is shown in Figure 4.20. With the current algorithm, generally around half of the signals are reconstructed outside the crossing of the bars. Although these results are preliminary, a high number of signals outside the crossing of the scintillator array is in agreement with the very low number of registered crossed coincidences, described in Section 4.5.4.

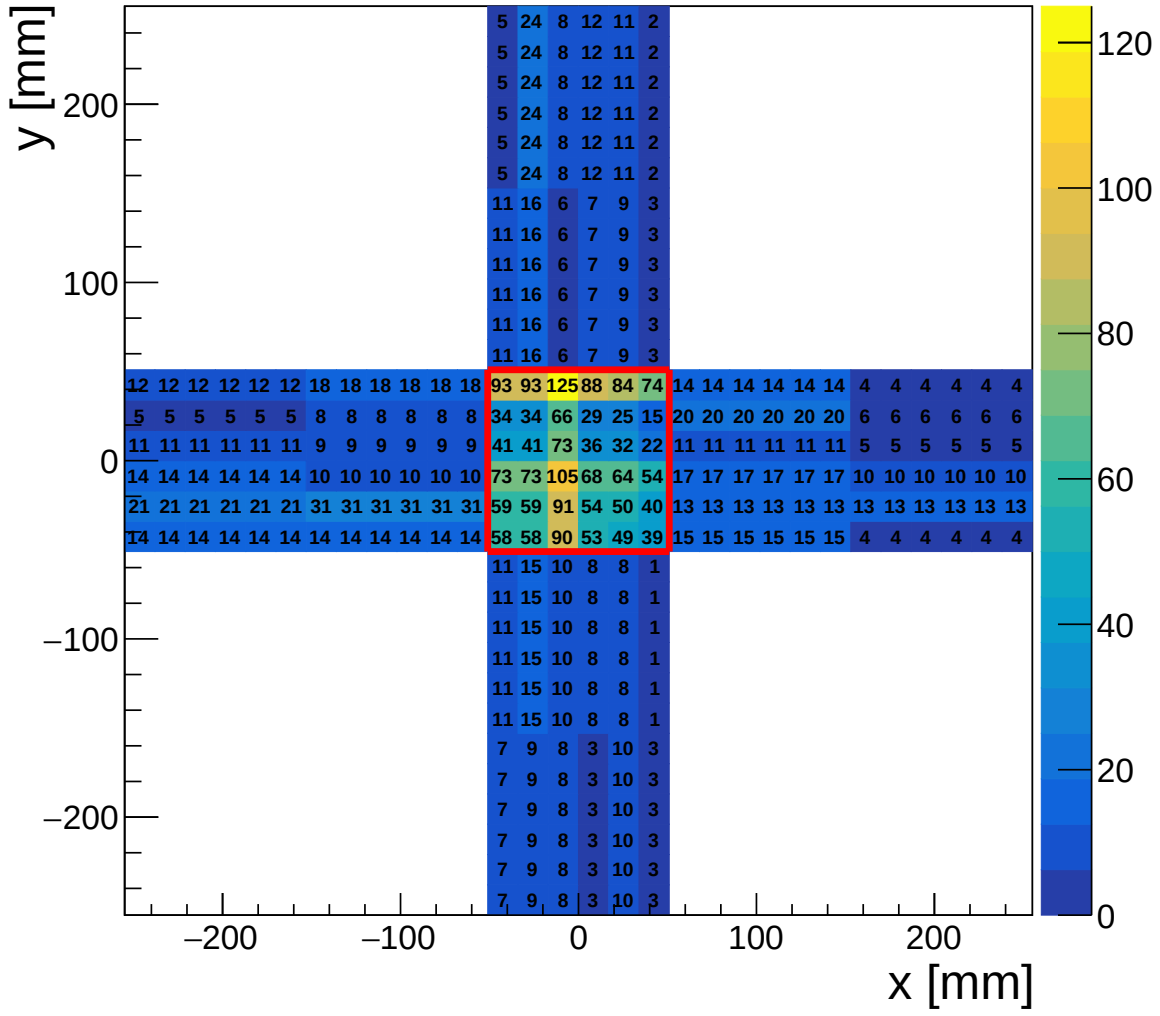

Figure 4.20: Hit map reconstruction of coincidences using Time-of-Arrival for signals with 500 ns delay from the γ-flash.

4.6 Neutron energy dependence

It is interesting to study the response of the detector in function of the delay of the acquisition from the γ-flash signal. This, in fact, corresponds to different neutron energies, and thus the array is exposed to particles originating from different reaction channels. Figure 4.21 shows the distribution of the coincidences in function of the delay from the γ-flash for the available data. Specifically, the rate per trigger of three types of coincidences is reported: coincidences between channels in a single bar, double bar coincidences in the same trigger, and crossed coincidences.

As expected, the rate of the crossed coincidences is the lowest one, since they are selected with the most stringent requirements. Single bar coincidences have instead the highest rate. These considerations, however, do not hold in a high rate environment such as the γ-flash, in which scintillating bars fire continuously. In this case, the rate for which a single bar fires is lower than the combinations of all bars that fire within the chosen time window. The effect is that the double coincidence and crossed coincidence rates are greater than the single bar coincidence rate, as seen in Figure 4.21 (first bin).

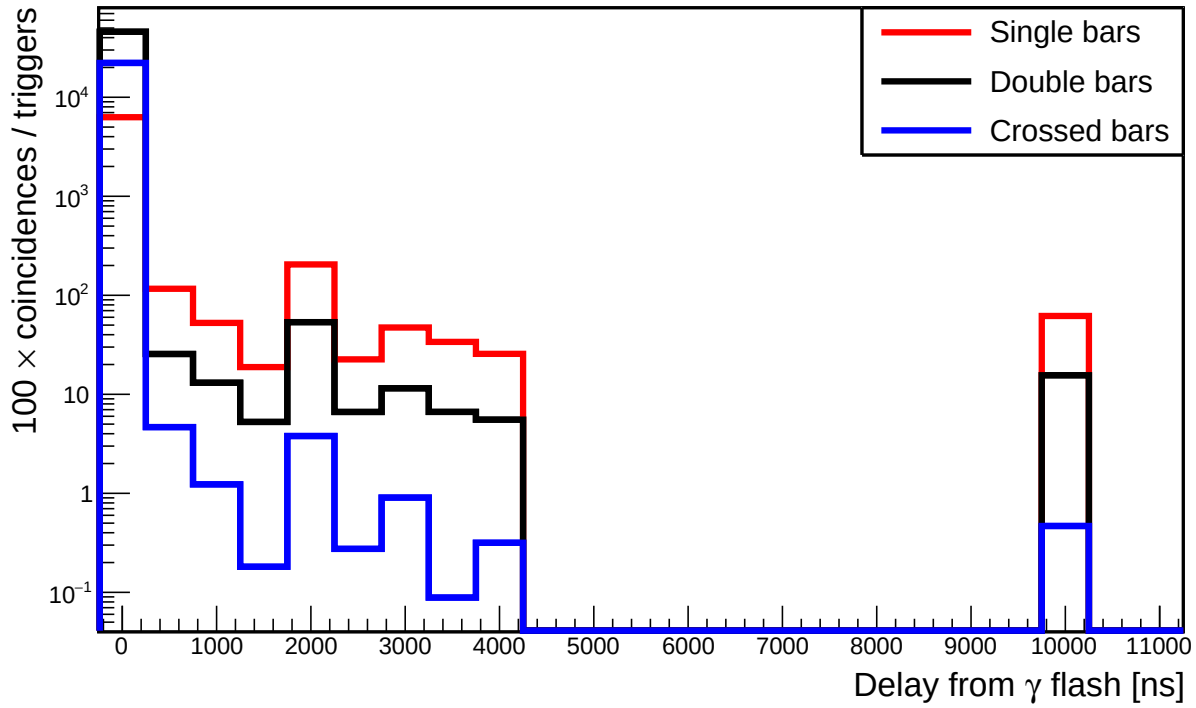

Figure 4.21: Distribution of the rate of coincidences over triggers in function of the delay from the γ-flash. The different colours refer to single bar coincidences (red), double bar coincidences of any orientation (black), crossed coincidences (blue). Occurrences have been rescaled for improved readability.

Considering neutron-induced reactions on the capsule target, the expected dominant source of background is the elastic scattering, which is more significant at lower neutron energies (longer TOFs). Other channels become relevant at neutron energies $E_n \gtrsim 1\,\mathrm{MeV}$, thus for data acquired until around 1500 ns from the γ-flash. In this early time window, however, also the tail of the γ-flash signal is present, and therefore a significant component of background should be attributed to it. This behaviour is confirmed in Figure 4.21, where all coincidences decrease with the delay from the γ-flash. However, there are other contributions to the signals, as seen from the non negligible amount of coincidences

registered even after a great delay from the γ-flash. A significant number of coincidences is observed at 2000 ns. The reason behind this may be, more than a physical background, a statistical effect. In fact, much more data have been taken with this delay, with respect to all other delays. If further analyses confirm this hypothesis, then more data taking must be acquired to correctly assess the background coincidences at different delays from γ-flash.

4.7 Final considerations

As mentioned in Section 4.1, the timing mode of the DAQ system does not provide direct amplitude information for the signals. Instead, it relies on the time-over-Threshold (ToT) measurement, which offers only a rough estimate of the pulse amplitude, and even then, only when calibrated with a known signal shape and amplitude.
An important consequence is that the identification of pile-up events from two successive signals is not possible in timing mode. This issue is particularly relevant for signals occurring near the large γ-flash signal, whose tail still has significant amplitude even at considerable time distances (of the order of µs) from the amplitude peak.
Another issue is related to the acquisition time gate, which is limited to 50 µs from the trigger (equivalent to neutron kinetic energies > 1 keV), thus not the whole available TOF window can be exploited. For these reasons, an alternative data acquisition system will be employed in the final setup.
In any case, the results of the experimental tests demonstrate that the trigger system based on scintillator bars with SiPM readout is suitable for use in EAR2. As mentioned earlier, the ideal solution involves using two planes per side, with bars of size 500 mm $\times$ 20 mm $\times$ 3 mm (20 bars per orientation), and fine-sampling acquisition using the n_TOF DAQ system, which is equipped with 1 GHz FADCs. However, the complete 2π setup, shown in Figure 3.7 would require 160 bars, 320 SiPMs, and an equal number of independent readout channels (fast FADCs). The need for an acceptable cost-performance compromise led to the development of the following options:

1. Omit the x-y configuration, halving the number of bars and channels;
2. Use a digital channel pattern (which acts as a trigger for both the scintillator bars and the µ-RWELL detectors) by appropriately grouping the analog signals from two adjacent SiPMs and sending them to the FADC.

The options above, combined together, offer several advantages:

- The digital channel pattern provides a fast trigger for the entire detector (including the µ-RWELL trigger and the SiPM data acquisition trigger);

- It enables the determination of the longitudinal coordinate, allowing the verification of the position obtained from the μ-RWELL track, with a spatial resolution of a few centimeters (based on the number of grouped SiPM analog signals);
- The number of FADC acquisition channels is reduced by a factor of 2, meaning only 80 FADC channels would be required (currently available at n_TOF), allowing the use of the n_TOF DAQ system without additional costs.

A possible design of the acquisition system, based on the digital channel pattern just described, is the LNGS FEE card, shown in Figure 4.22 together with the FERS. The LNGS FEE boards discriminate the signals, which are then sent to the CAEN V2495 module. The configuration of the activated SiPMs is recorded after selection by a validation mask. If the registered configuration meets the required conditions, a trigger signal is sent to the SRS system of the μ-RWELL. The same signal "freezes" the configuration and records it along with the event's absolute time. The module, extendable up to a maximum of 160 input channels and 32 output channels, can be programmed and read via the VME BUS through the CAEN V3718 VME-USB/optical bridge, providing trigger and validation configurations for the SiPMs. In addition to discriminating the SiPM signals, the FEE-LNGS boards provide the analog output to be sent to the centralized acquisition system of n_TOF, for each proton pulse on the spallation target.
This solution could be more suitable for the purposes of the proposed measurement than the one adopted in the test analyzed in this thesis, based on the CAEN FERS A5202 module. The latter has shown several critical issues, such as absence of digitizers, inability to resolve events close to the γ-flash, difficulty in integrating the acquisition with the SRS system used for the μ-RWELL.

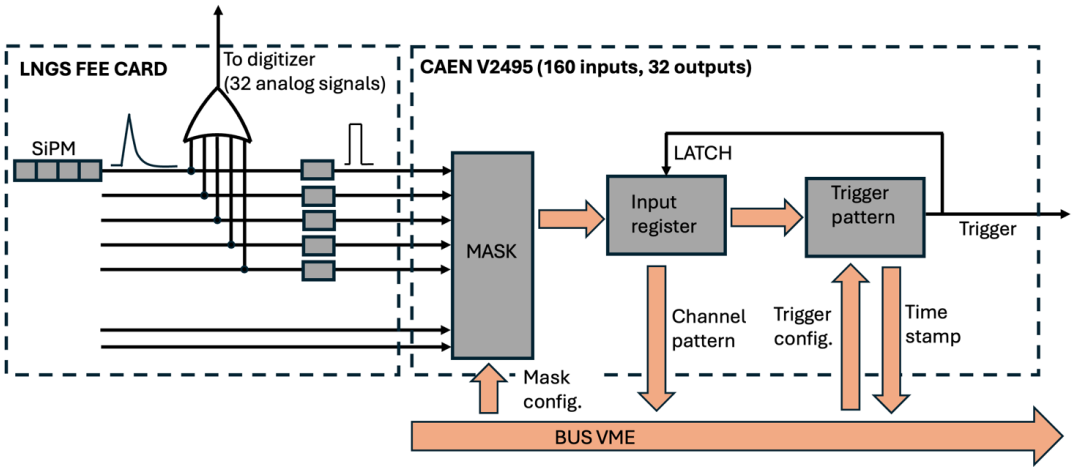

Figure 4.22: Scheme of the acquisition system based on the CAEN V2495 module.

Conclusions

Internal Pair Creation (IPC) is a well-studied quantum electrodynamics phenomenon. During the transition of an excited nucleus to its ground state, the dominant process is the emission of one or more high-energy photons. However, if the transition energy is high enough, an electron-positron pair can be created and emitted. The probability of IPC increases with the transition energy and decreases monotonically with increasing correlation angle between the emitted electron and positron.
In recent years, an anomaly in the emission of electron-positron pairs has been observed with high statistical significance in the final excited states of the nuclear reactions $^{7}\mathrm{Li}(\mathrm{p}, \mathrm{e}^{+}\mathrm{e}^{-})^{8}\mathrm{Be}$, $^{3}\mathrm{H}(\mathrm{p}, \mathrm{e}^{+}\mathrm{e}^{-})^{4}\mathrm{He}$ and $^{11}\mathrm{B}(\mathrm{p}, \mathrm{e}^{+}\mathrm{e}^{-})^{12}\mathrm{C}$. In particular, an excess of events has been detected at large correlation angles between the electron and positron for all three reactions.
Several hypotheses have been proposed to explain this anomaly. Among these, the interpretation of the excesses as the signature of the existence of a new particle beyond the standard model is one of the most intriguing. This hypothetical boson, referred to as X17, has an estimated rest mass of approximately $17\,\mathrm{MeV/c^2}$. However, many properties of this particle cannot yet be determined with the current experimental findings. Furthermore, this anomaly has not been confirmed or refuted by other independent experiments. The detection setups used in the original discoveries, based on detector telescopes, do not provide tracking or particle identification, and suffer from limited angular acceptance.
In order to address these issues, the n_TOF Collaboration has evaluated different detection setups to investigate the conjugate neutron-induced reaction $^{3}\mathrm{He}(\mathrm{n}, \mathrm{e}^{+}\mathrm{e}^{-})^{4}\mathrm{He}$.
The n_TOF facility at CERN provides a high-flux, pulsed neutron beam in a wide energy range, allowing for a comprehensive and precise measurement of the relevant spin-parity states of the excited ^{4}He nucleus. This experimental search is supported by reliable theoretical predictions on the interpretations of the X17 anomaly. With a precise measurement of the angular distribution of the emitted pairs following the reaction, the existence of the X17 boson can be verified and its quantum numbers determined.
In this thesis, the performance evaluation of the detection apparatus undergoing testing and calibration has been presented. The setup consists of four µ-RWELL gas detectors and a configuration of crossed scintillator bars surrounding the ^{3}He target. When combined with a magnetic field, this configuration ensures tracking and particle identification of

the electron-positron pairs within a large acceptance angle. In 2023, a data taking test of the detectors suited for this experiment was performed at n_TOF, in order to assess noise levels, saturation effects, optimize the detectors configuration and their suitability for the X17 detection.
The results of the analysis described in this thesis proved the scintillator bar array to be suitable for the study of this neutron-induced reaction. Its performance is adequate for its intended role in the final setup, which includes providing the trigger signal for the entire detection system, precisely measuring the neutron time of flight, and improving spatial resolution.
Timing information, consisting of Time-over-Threshold (ToT) and Time-of-Arrival (ToA), has been used to extract relevant properties of the detector and develop a preliminary reconstruction algorithm to be integrated with the tracking provided by the µ-RWELL.
The scintillator bars have confirmed their low sensitivity to the high neutron and gamma ray background. Although the detectors are momentarily blinded by the characteristic γ-flash of the n_TOF neutron beam, they recover in a time short enough to be sensitive to the neutron energies of interest. The exposure to the γ-flash also allowed for an estimation of the system's dead time.
Moreover, the analysis suggests that the performance of the scintillator bar array can be significantly improved by adopting a different data acquisition system than the one employed in the 2023 test, ideally including signal amplitude information and an extended acquisition time window. These improvements will allow for the identification of pileup effects, especially in presence of the γ-flash.

Bibliography

[1] A. J. Krasznahorkay et al. "Observation of Anomalous Internal Pair Creation in ^{8}Be: A Possible Indication of a Light, Neutral Boson". In: *Phys. Rev. Lett.* 116 (4 Jan. 2016), p. 042501. DOI: 10.1103/PhysRevLett.116.042501. URL: https://link.aps.org/doi/10.1103/PhysRevLett.116.042501.

[2] A. J. Krasznahorkay et al. "New anomaly observed in ^{4}He supports the existence of the hypothetical X17 particle". In: *Phys. Rev. C* 104 (4 Oct. 2021), p. 044003. DOI: 10.1103/PhysRevC.104.044003. URL: https://link.aps.org/doi/10.1103/PhysRevC.104.044003.

[3] A. J. Krasznahorkay et al. "New anomaly observed in ^{12}C supports the existence and the vector character of the hypothetical X17 boson". In: *Phys. Rev. C* 106 (6 Dec. 2022), p. L061601. DOI: 10.1103/PhysRevC.106.L061601. URL: https://link.aps.org/doi/10.1103/PhysRevC.106.L061601.

[4] K.S. Krane. *Introductory Nuclear Physics*. Wiley, 1991. ISBN: 9780471805533.

[5] C. Hofmann et al. "Angular correlation of electrons and positrons in internal pair conversion". In: *Phys. Rev. C* 42 (6 Dec. 1990), pp. 2632–2645. DOI: 10.1103/PhysRevC.42.2632. URL: https://link.aps.org/doi/10.1103/PhysRevC.42.2632.

[6] M. E. Rose. "Internal Pair Formation". In: *Phys. Rev.* 76 (5 Sept. 1949), pp. 678–681. DOI: 10.1103/PhysRev.76.678. URL: https://link.aps.org/doi/10.1103/PhysRev.76.678.

[7] P. Schlüter et al. "Conversion coefficient for internal pair creation". In: *Zeitschrift für Physik A Atoms and Nuclei* 286.2 (June 1978), pp. 149–158. ISSN: 0939-7922. DOI: 10.1007/BF01408969. URL: https://doi.org/10.1007/BF01408969.

[8] P. Schlüter and G. Soff. "Total and differential conversion coefficients for internal electron-positron pair creation". In: *Atomic Data and Nuclear Data Tables* 24.6 (1979), pp. 509–571. ISSN: 0092-640X. DOI: https://doi.org/10.1016/0092-640X(79)90008-1. URL: https://www.sciencedirect.com/science/article/pii/0092640X79900081.

[9] C. Hofmann and G. Soff. "Total and Differential Conversion Coefficients for Internal Pair Creation in Extended Nuclei". In: *Atomic Data and Nuclear Data Tables* 63.2 (1996), pp. 189–273. ISSN: 0092-640X. DOI: https://doi.org/10.1006/adnd.1996.0013. URL: https://www.sciencedirect.com/science/article/pii/S0092640X96900133.

[10] Dowie J. T. H. et al. "Table of electronic factors for E0 electron and electron–positron pair conversion transitions". In: *Atomic Data and Nuclear Data Tables* 131 (2020), p. 101283. ISSN: 0092-640X. DOI: https://doi.org/10.1016/j.adt.2019.06.002. URL: https://www.sciencedirect.com/science/article/pii/S0092640X19300336.

[11] G. K. Horton. "Angular Distribution in Internal Pair Creation". In: *Proceedings of the Physical Society* 60.5 (May 1948), p. 457. DOI: 10.1088/0959-5309/60/5/308. URL: https://dx.doi.org/10.1088/0959-5309/60/5/308.

[12] G. Goldring. "Internal Pairs in Anisotropic Emission". In: *Proceedings of the Physical Society. Section A* 66.4 (Apr. 1953), p. 341. DOI: 10.1088/0370-1298/66/4/304. URL: https://dx.doi.org/10.1088/0370-1298/66/4/304.

[13] M. E. Rose. "Internal Pairs from Aligned Nuclei". In: *Phys. Rev.* 131 (3 Aug. 1963), pp. 1260–1264. DOI: 10.1103/PhysRev.131.1260. URL: https://link.aps.org/doi/10.1103/PhysRev.131.1260.

[14] C. R. Hofmann et al. "Angular correlations in internal pair conversion of aligned heavy nuclei". In: *Phys. Rev. C* 53 (5 May 1996), pp. 2313–2323. DOI: 10.1103/PhysRevC.53.2313. URL: https://link.aps.org/doi/10.1103/PhysRevC.53.2313.

[15] E. K. Warburton. "Internal Pair Emission from Aligned Nuclei". In: *Phys. Rev.* 133 (6B Mar. 1964), B1368–B1372. DOI: 10.1103/PhysRev.133.B1368. URL: https://link.aps.org/doi/10.1103/PhysRev.133.B1368.

[16] J. Gulyás et al. "A pair spectrometer for measuring multipolarities of energetic nuclear transitions". In: *Nuclear Instruments and Methods in Physics Research Section A: Accelerators, Spectrometers, Detectors and Associated Equipment* 808 (2016), pp. 21–28. ISSN: 0168-9002. DOI: https://doi.org/10.1016/j.nima.2015.11.009. URL: https://www.sciencedirect.com/science/article/pii/S0168900215013716.

[17] G. Devons et al. "Emission of Electron-Positron Pairs from Light Nuclei I: Monopole Transition in ^{16}O". In: *Proceedings of the Physical Society. Section A* 67.2 (Feb. 1954), p. 134. DOI: 10.1088/0370-1298/67/2/305. URL: https://dx.doi.org/10.1088/0370-1298/67/2/305.

[18] S. Devons and G. Goldring. "Emission of Electron-Positron Pairs from Light Nuclei II: γ-Transitions in ^{8}Be, ^{10}B and ^{16}O". In: *Proceedings of the Physical Society. Section A* 67.5 (May 1954), p. 413. DOI: 10.1088/0370-1298/67/5/302. URL: https://dx.doi.org/10.1088/0370-1298/67/5/302.

[19] G. Goldring. "Emission of Electron-Positron Pairs from Light Nuclei III: γ-Transitions in the Reaction ^{15}N(p, γ)^{16}O". In: *Proceedings of the Physical Society. Section A* 67.10 (Oct. 1954), p. 930. DOI: 10.1088/0370-1298/67/10/312. URL: https://dx.doi.org/10.1088/0370-1298/67/10/312.

[20] A. Buda et al. "Positron-electron decay of ^{28}Si at an excitation energy of 50 MeV". In: *Nuclear Physics A* 553 (1993), pp. 509–513. ISSN: 0375-9474. DOI: https://doi.org/10.1016/0375-9474(93)90649-I. URL: https://www.sciencedirect.com/science/article/pii/037594749390649I.

[21] A. Passoja et al. "Adaptation of a superconducting-solenoid-transporter Si(Li) - Si(Li) spectrometer for in-beam studies of internal-pair transitions". In: *Nuclear Instruments and Methods in Physics Research* 223.1 (1984), pp. 96–102. ISSN: 0167-5087. DOI: https://doi.org/10.1016/0167-5087(84)90249-7. URL: https://www.sciencedirect.com/science/article/pii/0167508784902497.

[22] C. S. Galovich et al. "Design and performance of an electron-positron pair detector". In: *Nuclear Instruments and Methods in Physics Research Section A: Accelerators, Spectrometers, Detectors and Associated Equipment* 271.3 (1988), pp. 483–490. ISSN: 0168-9002. DOI: https://doi.org/10.1016/0168-9002(88)90309-9. URL: https://www.sciencedirect.com/science/article/pii/0168900288903099.

[23] D.R. Tilley et al. "Energy levels of light nuclei A=8,9,10". In: *Nuclear Physics A* 745.3 (2004), pp. 155–362. ISSN: 0375-9474. DOI: https://doi.org/10.1016/j.nuclphysa.2004.09.059. URL: https://www.sciencedirect.com/science/article/pii/S0375947404010267.

[24] J. L. Feng et al. "Particle physics models for the 17 MeV anomaly in beryllium nuclear decays". In: *Phys. Rev. D* 95 (3 Feb. 2017), p. 035017. DOI: 10.1103/PhysRevD.95.035017. URL: https://link.aps.org/doi/10.1103/PhysRevD.95.035017.

[25] J. L. Feng et al. "Protophobic Fifth-Force Interpretation of the Observed Anomaly in ^{8}Be Nuclear Transitions". In: *Phys. Rev. Lett.* 117 (7 Aug. 2016), p. 071803. DOI: 10.1103/PhysRevLett.117.071803. URL: https://link.aps.org/doi/10.1103/PhysRevLett.117.071803.

[26] G. Charpak and F. Sauli. "Multiwire proportional chambers and drift chambers". In: *Nuclear Instruments and Methods* 162.1 (1979), pp. 405–428. ISSN: 0029-554X. DOI: https://doi.org/10.1016/0029-554X(79)90726-2. URL: https://www.sciencedirect.com/science/article/pii/0029554X79907262.

[27] D. S. Firak et al. "Confirmation of the existence of the X17 particle". In: *EPJ Web Conf.* 232 (2020), p. 04005. DOI: 10.1051/epjconf/202023204005. URL: https://doi.org/10.1051/epjconf/202023204005.

[28] T. T. Anh et al. "Checking the ^{8}Be Anomaly with a Two-Arm Electron Positron Pair Spectrometer". In: *Universe* 10.4 (2024). ISSN: 2218-1997. DOI: 10.3390/universe10040168. URL: https://www.mdpi.com/2218-1997/10/4/168.

[29] G. Carlo. "X17: Status and Perspectives". In: *Universe* 10.7 (2024). ISSN: 2218-1997. DOI: 10.3390/universe10070285. URL: https://www.mdpi.com/2218-1997/10/7/285.

[30] A. Aleksejevs et al. *A Standard Model Explanation for the "*ATOMKI *Anomaly"*. 2021. arXiv: 2102.01127 [hep-ph]. URL: https://arxiv.org/abs/2102.01127.

[31] H. X. Chen. *Is the* X17 *composed of four bare quarks?* 2020. arXiv: 2006.01018 [hep-ph]. URL: https://arxiv.org/abs/2006.01018.

[32] V. Kubarovsky et al. *Quantum Chromodynamics Resolution of the ATOMKI Anomaly in* ^{4}He *Nuclear Transitions*. 2024. arXiv: 2206.14441 [hep-ph]. URL: https://arxiv.org/abs/2206.14441.

[33] C. Y. Wong. "QED Meson Description of the Anomalous Particles at ~ 17 and ~ 38 MeV". In: *Universe* 10.4 (2024). ISSN: 2218-1997. DOI: 10.3390/universe10040173. URL: https://www.mdpi.com/2218-1997/10/4/173.

[34] X. Zhang and G. A. Miller. "Can a protophobic vector boson explain the ATOMKI anomaly?" In: *Physics Letters B* 813 (2021), p. 136061. ISSN: 0370-2693. DOI: https://doi.org/10.1016/j.physletb.2021.136061. URL: https://www.sciencedirect.com/science/article/pii/S0370269321000010.

[35] Koch B. "X17: A new force, or evidence for a hard $\gamma - \gamma$ process?" In: *Nuclear Physics A* 1008 (2021), p. 122143. ISSN: 0375-9474. DOI: https://doi.org/10.1016/j.nuclphysa.2021.122143. URL: https://www.sciencedirect.com/science/article/pii/S0375947421000087.

[36] P. Kálmán and T. Keszthelyi. "Anomalous internal pair creation". In: *The European Physical Journal A* 56.8 (Aug. 2020), p. 205. ISSN: 1434-601X. DOI: 10.1140/epja/s10050-020-00202-z. URL: https://doi.org/10.1140/epja/s10050-020-00202-z.

[37] D. S. M. Alves et al. "Shedding light on X17: community report". In: *The European Physical Journal C* 83.3 (Mar. 2023), p. 230. ISSN: 1434-6052. DOI: 10.1140/epjc/s10052-023-11271-x. URL: https://doi.org/10.1140/epjc/s10052-023-11271-x.

[38] J. R. Batley et al. "Search for the dark photon in π^0 decays". In: *Physics Letters B* 746 (2015), pp. 178–185. ISSN: 0370-2693. DOI: https://doi.org/10.1016/j.physletb.2015.04.068. URL: https://www.sciencedirect.com/science/article/pii/S0370269315003342.

[39] L. Morel et al. "Determination of the fine-structure constant with an accuracy of 81 parts per trillion". In: *Nature* 588.7836 (Dec. 2020), pp. 61–65. ISSN: 1476-4687. DOI: 10.1038/s41586-020-2964-7. URL: https://doi.org/10.1038/s41586-020-2964-7.

[40] U. Ellwanger and S. Moretti. "Possible explanation of the electron positron anomaly at 17 MeV in ^{8}Be transitions through a light pseudoscalar". In: *Journal of High Energy Physics* 2016.11 (Nov. 2016), p. 39. ISSN: 1029-8479. DOI: 10.1007/JHEP11(2016)039. URL: https://doi.org/10.1007/JHEP11(2016)039.

[41] L. Delle Rose et al. "Explanation of the 17 MeV Atomki anomaly in a $U(1)^{'}$-extended two Higgs doublet model". In: *Phys. Rev. D* 96 (11 Dec. 2017), p. 115024. DOI: 10.1103/PhysRevD.96.115024. URL: https://link.aps.org/doi/10.1103/PhysRevD.96.115024.

[42] L. Delle Rose et al. "Atomki Anomaly in Family-Dependent $U(1)^{'}$ Extension of the Standard Model". In: *Phys. Rev. D* 99 (5 Mar. 2019), p. 055022. DOI: 10.1103/PhysRevD.99.055022. URL: https://link.aps.org/doi/10.1103/PhysRevD.99.055022.

[43] L. Delle Rose et al. "New Physics Suggested by ATOMKI Anomaly". In: *Frontiers in Physics* 7 (2019). ISSN: 2296-424X. DOI: 10.3389/fphy.2019.00073. URL: https://www.frontiersin.org/journals/physics/articles/10.3389/fphy.2019.00073.

[44] C. Rubbia et al. *A High Resolution Spallation Driven Facility at the CERN-PS to Measure Neutron Cross Sections in the Interval from 1 eV to 250 MeV: a Relative Performance Assessment*. Tech. rep. Addendum to CERN-LHC-98-002-EET. Geneva: CERN, 1998. URL: https://cds.cern.ch/record/363828.

[45] C. Guerrero et al. "Performance of the neutron time-of-flight facility n_TOF at CERN". In: *The European Physical Journal A* 49.2 (Feb. 2013), p. 27. ISSN: 1434-601X. DOI: 10.1140/epja/i2013-13027-6. URL: https://doi.org/10.1140/epja/i2013-13027-6.

[46] F. Gunsing et al. "Nuclear data activities at the n_TOF facility at CERN". In: *The European Physical Journal Plus* 131.10 (Oct. 2016), p. 371. ISSN: 2190-5444. DOI: 10.1140/epjp/i2016-16371-4. URL: https://doi.org/10.1140/epjp/i2016-16371-4.

[47] E. Dupont et al. "Overview of the dissemination of n_TOF experimental data and resonance parameters". In: *EPJ Web of Conf.* 284 (2023), p. 18001. DOI: 10.1051/epjconf/202328418001. URL: https://doi.org/10.1051/epjconf/202328418001.

[48] G. F. Knoll. *Radiation detection and measurement*. New York, NY: Wiley, 2010.

[49] B. T. M. Willis and C. J. Carlile. *Experimental Neutron Scattering*. Oxford University Press, 2013. ISBN: 9780199673773.

[50] M. Barbagallo et al. "High-accuracy determination of the neutron flux at n_TOF". In: *The European Physical Journal A* 49.12 (Dec. 2013), p. 156. ISSN: 1434-601X. DOI: 10.1140/epja/i2013-13156-x. URL: https://doi.org/10.1140/epja/i2013-13156-x.

[51] T. Hortala. *n_TOF poised for 10 more years of research with third-generation neutron spallation target*. 2021. URL: https://home.web.cern.ch/news/news/experiments/ntof-poised-10-more-years-research-third-generation-neutron-spallation-target.

[52] R. Esposito et al. "Design of the third-generation lead-based neutron spallation target for the neutron time-of-flight facility at CERN". In: *Phys. Rev. Accel. Beams* 24 (9 Sept. 2021), p. 093001. DOI: 10.1103/PhysRevAccelBeams.24.093001. URL: https://link.aps.org/doi/10.1103/PhysRevAccelBeams.24.093001.

[53] M. Calviani et al. *n_TOF neutron spallation Target #3 N2 cooled bare Pb core – Engineering Design Report*. Tech. rep. Eng. spec. TOF-TAR-ES-0003 (EDMS 2154581). Geneva, Switzerland: CERN, 2019.

[54] M. Calviani. *Diagram of the n_TOF facility*. General Photo. 2021. URL: https://cds.cern.ch/record/2765232.

[55] N. Patronis et al. "Status report of the n_TOF facility after the 2nd CERN long shutdown period". In: *EPJ Techniques and Instrumentation* 10.1 (May 2023), p. 13. ISSN: 2195-7045. DOI: 10.1140/epjti/s40485-023-00100-w. URL: https://doi.org/10.1140/epjti/s40485-023-00100-w.

[56] C. Weiß et al. "The new vertical neutron beam line at the CERN n_TOF facility design and outlook on the performance". In: *Nuclear Instruments and Methods in Physics Research Section A: Accelerators, Spectrometers, Detectors and Associated Equipment* 799 (2015), pp. 90–98. ISSN: 0168-9002. DOI: https://doi.org/10.1016/j.nima.2015.07.027. URL: https://www.sciencedirect.com/science/article/pii/S0168900215008566.

[57] Y. H. Chen et al. "Characterization of the n_TOF EAR-2 neutron beam". In: *EPJ Web Conf.* 146 (2017), p. 03020. DOI: 10.1051/epjconf/201714603020. URL: https://doi.org/10.1051/epjconf/201714603020.

[58] F. Mingrone et al. "Development of a Neutron Imaging Station at the n_TOF Facility of CERN and Applications to Beam Intercepting Devices". In: *Instruments* 3.2 (2019). ISSN: 2410-390X. DOI: 10.3390/instruments3020032. URL: https://www.mdpi.com/2410-390X/3/2/32.

[59] M. Sabaté-Gilarte et al. "High-accuracy determination of the neutron flux in the new experimental area n_TOF-EAR2 at CERN". In: *The European Physical Journal A* 53.10 (Oct. 2017), p. 210. ISSN: 1434-601X. DOI: 10.1140/epja/i2017-12392-4. URL: https://doi.org/10.1140/epja/i2017-12392-4.

[60] J. A. Pavón-Rodríguez et al. "Characterisation of the n_TOF 20 m beam line at CERN with the new spallation target". In: *EPJ Web of Conf.* 284 (2023), p. 06006. DOI: 10.1051/epjconf/202328406006. URL: https://doi.org/10.1051/epjconf/202328406006.

[61] M. E. Stamati et al. "The n_TOF NEAR Station Commissioning and first physics case". In: *EPJ Web of Conf.* 284 (2023), p. 06009. DOI: 10.1051/epjconf/202328406009. URL: https://doi.org/10.1051/epjconf/202328406009.

[62] The n_TOF Collaboration. *The new n_TOF NEAR Station*. Tech. rep. Ginevra: CERN, 2020. URL: https://cds.cern.ch/record/2737308.

[63] M. Ferrari et al. "Design development and implementation of an irradiation station at the neutron time-of-flight facility at CERN". In: *Phys. Rev. Accel. Beams* 25 (10 Oct. 2022), p. 103001. DOI: 10.1103/PhysRevAccelBeams.25.103001. URL: https://link.aps.org/doi/10.1103/PhysRevAccelBeams.25.103001.

[64] G. Gervino et al. "NEAR: A New Station to Study Neutron-Induced Reactions of Astrophysical Interest at CERN-n_TOF". In: *Universe* 8.5 (2022). ISSN: 2218-1997. DOI: 10.3390/universe8050255. URL: https://www.mdpi.com/2218-1997/8/5/255.

[65] D.R. Tilley, H.R. Weller, and G.M. Hale. "Energy levels of light nuclei A = 4". In: *Nuclear Physics A* 541.1 (1992), pp. 1–104. ISSN: 0375-9474. DOI: https://doi.org/10.1016/0375-9474(92)90635-W. URL: https://www.sciencedirect.com/science/article/pii/037594749290635W.

[66] M. Viviani et al. "X17 boson and the ^{3}H$(p, e^+e^-)^4$He and ^{3}He$(n, e^+e^-)^4$He processes: A theoretical analysis". In: *Phys. Rev. C* 105 (1 Jan. 2022), p. 014001. DOI: 10.1103/PhysRevC.105.014001. URL: https://link.aps.org/doi/10.1103/PhysRevC.105.014001.

[67] W.R. Leo. *Techniques for Nuclear and Particle Physics Experimentes: a how-to approach*. Springer, 1981.

[68] onsemi®. *Introduction to the Silicon Photomultiplier (SiPM)*. https://www.onsemi.com/pub/Collateral/AND9770-D.PDF. 2023.

[69] F. Sauli. "GEM: A new concept for electron amplification in gas detectors". In: *Nuclear Instruments and Methods in Physics Research Section A: Accelerators, Spectrometers, Detectors and Associated Equipment* 386.2 (1997), pp. 531–534. ISSN: 0168-9002. DOI: https://doi.org/10.1016/S0168-9002(96)01172-2. URL: https://www.sciencedirect.com/science/article/pii/S0168900296011722.

[70] G. Bencivenni et al. "The micro-RWELL layouts for high particle rate". In: *JINST* 14.05 (2019), P05014. DOI: 10.1088/1748-0221/14/05/P05014. arXiv: 1903.11017. URL: https://cds.cern.ch/record/2672599.

[71] G. Bencivenni et al. "The micro-Resistive WELL detector: a compact spark-protected single amplification-stage MPGD". In: *Journal of Instrumentation* 10.02 (Feb. 2015), P02008. DOI: 10.1088/1748-0221/10/02/P02008. URL: https://dx.doi.org/10.1088/1748-0221/10/02/P02008.

[72] S. Bachmann et al. "Discharge studies and prevention in the gas electron multiplier (GEM)". In: *Nuclear Instruments and Methods in Physics Research Section A: Accelerators, Spectrometers, Detectors and Associated Equipment* 479.2 (2002), pp. 294–308. ISSN: 0168-9002. DOI: https://doi.org/10.1016/S0168-9002(01)00931-7. URL: https://www.sciencedirect.com/science/article/pii/S0168900201009317.

[73] T. Alexopoulos et al. "Development of large size Micromegas detector for the upgrade of the ATLAS Muon system". In: *Nuclear Instruments and Methods in Physics Research Section A: Accelerators, Spectrometers, Detectors and Associated Equipment* 617.1 (2010). 11th Pisa Meeting on Advanced Detectors, pp. 161–165. ISSN: 0168-9002. DOI: https://doi.org/10.1016/j.nima.2009.06.113. URL: https://www.sciencedirect.com/science/article/pii/S0168900209013485.

[74] Scionix Holland B.V. *General Purpose EJ-200, EJ-204, EJ-208, EJ-212*. https://scionix.nl/frame/.

[75] Hamamatsu Photonics K. K. *MPPC array S13363-3050NE-16*. https://www.hamamatsu.com/us/en/product/optical-sensors/mppc/mppc_mppc-array/S13363-3050NE-16.html.

[76] CAEN S.p.A. *A5202 64 Channel Citiroc unit for FERS-5200*. https://www.caen.it/products/a5202/.